Università degli Studi di Milano Bicocca
DIPARTIMENTO DI FISICA G. OCCHIALINI

CORSO DI DOTTORATO IN FISICA E ASTRONOMIA
CICLO XXVII

Search for a Higgs boson decaying into a di-τ pair in the double hadronic final state

Settore scientifico disciplinare FIS/01

Tesi di Dottorato di:
RICCARDO A. MANZONI

Tutore: Dr. Sandra Malvezzi

Anno Accademico 2013-2014

ABSTRACT

Elucidating the mechanism of electroweak symmetry breaking, through which the W and Z bosons become massive, is an important goal of the Large Hadron Collider (LHC) physics programme.

In the standard model (SM), electroweak symmetry breaking is achieved via the Brout-Englert-Higgs mechanism, which also predicts the existence of a scalar Higgs boson.

On July 4, 2012, the discovery of a new boson with mass around 125 GeV was announced at CERN by the ATLAS and CMS Collaborations. The excess was most significant in the ZZ, $\gamma\gamma$, and WW decay modes. The spin and CP properties of the new boson are compatible with those of the SM Higgs boson.

In the SM, the masses of the fermions are generated via the Yukawa couplings between the Higgs field and the fermionic fields. The measurement of these couplings is essential for identifying this boson as the SM Higgs boson.

The $\tau\tau$ decay mode is the most promising to test the fermionic decays of the Higgs boson, thanks to its large event rate expected in the SM compared to the other leptonic decay modes and the smaller contribution from background events with respect to the $b\bar{b}$ decay mode.

This thesis reports on the results of a search for a SM Higgs boson using final states with a pair of τ leptons in proton-proton collisions at $\sqrt{s} = 7$ and 8 TeV at the LHC. The entire dataset collected in 2011 and 2012 by the CMS experiment is used, corresponding to an integrated luminosity of $4.9\,fb^{-1}$ at a centre-of-mass energy of 7 TeV and $19.7\,fb^{-1}$ at 8 TeV.

All six τ-pair final states are studied: $\mu\tau_h$, $e\tau_h$, $\tau_h\tau_h$, $e\mu$, $\mu\mu$ and ee. The present work is focussed on the fully hadronic $\tau_h\tau_h$ final state which comprises the 42% of di-τ events. Moreover, the presence of only two neutrinos in the decay chain, as opposed to three or four neutrinos in the semi or fully leptonic final state respectively, allows for a better mass resolution.

These peculiar features have been vastly exploited and the fully hadronic final state provided a critical performance breakthrough to the $H \to \tau\tau$ search, finally reaching the sensitivity to the SM Higgs boson.

In addition to treating separately the six different di-τ channels, the events are furthermore classified in categories according to the number of reconstructed jets and additional light leptons in the final state in order to maximize the sensitivity of the analysis and assess the three dominant SM Higgs boson production modes at the LHC:

gluon-gluon fusion, vector boson fusion (VBF) and W/Z associated production.

The signal extraction is performed through a maximum likelihood fit based, for most of the channels, on the distribution of the invariant mass of the τ-lepton pair, $m_{\tau\tau}$, calculated from the four-momenta of the Higgs leptons and the missing transverse energy vector.

An excess of events is observed over the expected background contributions, with a local significance larger than 3 standard deviations for m_H values between 115 and 130 GeV. The best fit of the observed $H \to \tau\tau$ signal cross section times branching fraction for $m_H = 125$ GeV is 0.78 ± 0.27 times the standard model expectation.

These observations constitute evidence for the 125 GeV Higgs boson decaying to a pair of τ leptons.

Despite the extraordinary success of the SM in describing the particles physics phenomena known so far, few theoretical problems remain unsolved. Most notably, the Higgs boson mass in the SM is not protected against quadratically divergent quantum-loop corrections at high energy. This is known as the *hierarchy problem*. In the model of supersymmetry (SUSY), which postulates a symmetry between the fundamental bosons and fermions, a cancellation of these divergences occurs naturally.

The Higgs sector of the minimal supersymmetric extension of the standard model (MSSM) contains two scalar doublets that result in five physical Higgs bosons: a light and a heavy CP-even Higgs boson h and H, a CP-odd Higgs boson A, and two charged Higgs bosons $H^{\pm}$. At tree level the Higgs sector can be expressed in terms of two parameters which are usually chosen as the mass of the CP-odd Higgs boson m_A and $\tan\beta$, the ratio of the two vacuum expectation values of the two Higgs doublets.

In large part of the $\tan\beta$ vs m_A parameters space the branching fraction to tau leptons is also enhanced, making the search for neutral MSSM Higgs bosons in the $\tau\tau$ final state particularly interesting.

In these thesis, a search for neutral Higgs bosons in the MSSM decaying to tau-lepton pairs is presented. This analysis stemmed out from its SM counterpart, is based on the same CMS datasets, employs the same physics objects definitions and uses similar techniques for the backgrounds estimates and signal extraction.

No excess is observed in the tau-lepton-pair invariant mass spectrum. Exclusion limits are presented in the MSSM parameter space for different benchmark scenarios, m_h^{max}, m_h^{mod+}, m_h^{mod-}, light-stop, light-stau, τ-phobic, and low-m_H. Upper limits on the cross section times branching fraction for gluon fusion and b-quark associated Higgs boson production are also given.

SOMMARIO

La verifica del meccanismo di rottura della simmetria elettrodebole, attraverso il quale i bosoni W e Z acquisiscono massa, è uno degli obiettivi più importanti del programma di fisica del Large Hadron Collider (LHC).

Nel modello standard (SM), la rottura della simmetria elettrodebole è generata dal meccanismo di Brout-Englert-Higgs, il quale prevede inoltre l'esistenza di un bosone scalare neutro, il bosone di Higgs.

Il 4 Luglio 2012 le Collaborazioni ATLAS e CMS hanno annunciato la scoperta di un nuovo bosone con massa intorno a 125 GeV. L'eccesso osservato era particolarmente significativo nei canali ZZ, $\gamma\gamma$ and WW. Le misure di spin e CP del nuovo bosone sono in accordo con le predisioni dello SM.

Nello SM, le masse dei fermioni sono generate attraverso gli accoppiamenti di Yukawa tra il campo di Higgs e i campi fermionici. La misura di questi accoppiamenti è fondamentale per corroborare la natura SM del nuovo bosone.

Il canale $\tau\tau$ è particolarmente promettente, grazie al branching ratio pari al 6.3% per $m_H = 125$ GeV , più alto rispetto agli altri decadimenti leptonici, e alla più contenuta contaminazione da parte dei processi di fondo rispetto al modo di decadimento dominante $b\bar{b}$.

In questa tesi vengono riportati i risultati della ricerca di un bosone di Higgs SM nello stato finale comprendente due leptoni τ, compiuta all'LHC in collisioni protone-protone all'energia nel centro di massa di $\sqrt{s} = 7$ e 8 TeV. Sono stati analizzati gli interi dataset raccolti da CMS nel 2011 e nel 2012, corrispondenti alla luminosità di 4.9 fb^{-1} a $\sqrt{s} = 7$ TeV e 19.7 fb^{-1} a $\sqrt{s} = 8$ TeV

Sono stati studiati tutti i possibili sei stati finali di-τ: $\mu\tau_h$, $e\tau_h$, $\tau_h\tau_h$, $e\mu$, $\mu\mu$ e ee. Questa tesi, in particolare, descrive l'analisi condotta nello stato finale completamente adronico $\tau_h\tau_h$.

Lo stato finale completamente adronico comprende il 42% degli eventi con due leptoni τ, e, grazie alla presenza di due soli neutrini provenienti dai decadimenti dei τ, offre una migliore risoluzione in massa rispetto agli stati finali semi e completamente leptonici.

Queste caratteristiche sono state ampiamente sfruttate nell'analisi e hanno permesso di raggiungere la sensibilità necessaria per osservare il bosone di Higgs previsto nello SM.

Per massimizzare la sensibilità dell'analisi e provare i tre principali modi di produzione dell bosone di Higgs SM, gluon-gluon fusion, vector boson fusion (VBF) e produzione in associazione con un bosone vettore W o Z, gli eventi sono stati ulteriormente classificati in

diverse categorie mutuamente esclusive, definite secondo il numero di jet, elettroni o muoni nell'evento.

L'estrazione del segnale è stata ottenuta attraverso un maximum likelihood fit basato, per la maggior parte dei canali, sulla distribuzione della massa invariante dei due leptoni τ, $m_{\tau\tau}$, calcolata a partire dai quadrivettori degli stessi e dalla energia trasversa mancate.

Nei dati è stato osservato un eccesso di eventi rispetto alla predizione per i soli fondi. La significanza locale eccede le 3 deviazioni standard per valori di m_H compresi tra 115 e 130 GeV. Il prodotto della sezione d'urto per branching ratio, misurato per il segnale a $m_H = 125$ GeV, corrisponde a 0.78 ± 0.27 volte il valore predetto dallo SM.

Questo costituisce l'evidenza dei decadimenti in coppie di leptoni τ del bosone di Higgs a 125 GeV.

Nonostante l'immenso successo dello SM nel descrivere la maggior parte dei fenomeni osservati in fisica delle particelle, si ritiene che esso non sia la teoria ultima. Uno dei problemi che non trova soluzione all'interno dello SM è noto come *problema della gerarchia*. Nello SM la massa del bosone di Higgs non è protetta da correzioni a loop che divergono quadraticamente e per ottenere un valore finito per m_H è necessario un *fine tuning* innaturalmente *fine*.

I modelli supersimmetrici (SUSY) risolvono questo problema postulando una simmetria tra bosoni e fermioni fondamentali. Le correzioni radiative alla massa del bosone di Higgs sono finite poichè, ad ogni diagramma a loop nel quale circola una fermione (bosone) SM, corrisponde un diagramma equivalente, ma con fase opposta, nel quale circola il corrispettivo bosone (fermione) supersimmetrico. In questo modo avviene una cancellazione naturale delle divergenze quadratiche.

Il settore di Higgs dell'estensione minimale supersimmetrica dello standard model (MSSM) contiene due doppietti scalari che danno luogo a cinque bosoni di Higgs: due neutri CP-pari, uno leggeto h e uno pesante H, uno neutro, massivo, e CP-dispari, A e due carichi $H^{\pm}$. A livello albero, il settore di Higgs può essere completamente espresso in funzione di due parametri, la massa di A e il rapporto tra i valori di aspettazione del vuoto dei due doppietti di Higgs $\tan\beta$.

In questa tesi viene anche descritta la ricerca di un bosone di Higgs neutro MSSM nel canale $\tau\tau$. Questo canale è particolarmente interessante poiché i decadimenti in leptoni τ sono favoriti in buona parte dello spazio dei parametri.

Questa analisi deriva da quella SM, impiega gli stessi dataset di CMS e con essa condivide la definizione degli *physics objects*, le tecniche di stima dei fondi e i metodi di estrazione del segnale.

Non viene osservato nessun eccesso nello spettro di massa invariante $m_{\tau\tau}$ e si procede quindi a fissare limiti di esclusione nello spazio dei parametri. Sono stati considerati diversi *benchmark scenarios*, m_h^{max},

m_h^{mod+}, m_h^{mod-}, light-stop, light-stau, τ-phobic, e low-m_H. Vengono inoltre forniti limiti sul prodotto di sezione d'urto per branching ratio per i due più rilevanti modi di produzione, gluon-gluon fusion e produzione associata con b-quark.

CONTENTS

LIST OF FIGURES

LIST OF TABLES

1 THEORY

1.1 THE STANDARD MODEL

The Standard Model of particle physics (SM) [127, 135, 92] is the theoretical framework that encompasses the fundamental constituents of matter and describes the particle interactions by means of forces.

The SM is a renormalizable Quantum Field Theory based on global Poincaré space-time symmetry and local gauge invariance under transformations of the direct product of the groups $SU(3)_C \times SU(2)_L \times U(1)_Y$. All but one elementary particles fit into the SM as either spin-1/2 fermions or spin-1 bosons. The only spin-0 particle foreseen in the SM is the Higgs boson, which is detailed in Sec. 1.1.1. A synoptic view of the SM particles and their quantum numbers is given in Tab. 1. Matter particles, consisting of lepton and quark fermions, appear as right- and left-handed spinors identified as irreducible representations of the Poincaré group, whereas gauge bosons are structured in adjoint representations of the corresponding gauge groups.

	field			spin	$SU(3)_C$	$SU(2)_L$	Y	Q
leptons	$\begin{pmatrix} e \\ \nu_e \end{pmatrix}_L$	$\begin{pmatrix} \mu \\ \nu_\mu \end{pmatrix}_L$	$\begin{pmatrix} \tau \\ \nu_\tau \end{pmatrix}_L$	1/2	1	2	1/3	$\begin{pmatrix} -1 \\ 0 \end{pmatrix}$
	e_R	μ_R	τ_R	1/2	1	1	4/3	1
	$\begin{pmatrix} u \\ d \end{pmatrix}_L$	$\begin{pmatrix} c \\ s \end{pmatrix}_L$	$\begin{pmatrix} t \\ b \end{pmatrix}_L$	1/2	3	2	1/3	$\begin{pmatrix} -2/3 \\ 1/3 \end{pmatrix}$
quarks	u_R	c_R	t_R	1/2	3	1	4/3	2/3
	d_R	s_R	b_R	1/2	3	1	-2/3	-1/3
Higgs		$\begin{pmatrix} \phi^+ \\ \phi^0 \end{pmatrix}_L$		0	1	2	1	0
		W^i_μ		1	1	3	0	1
gauge bosons		B_μ		1	1	1	0	0
		G^a_μ		1	8	1	0	0

Table 1: The field content of the Standard Model of particle physics. The Higgs boson, quarks and leptons are shown in their $SU(2)_L$ representations. Also shown, is the corresponding spin, hypercharge Y, electromagnetic charge Q and representation under $SU(3)_C$, $SU(2)_L$ of each field.

The particle interactions occur through Quantum Chromodynamics (QCD, strong force) and Electroweak (EW) force. In the EW sector, the gauge bosons are represented by the $SU(2)_L$ isotriplet W^i_μ together with the isosinglet B_μ of $U(1)_Y$. Left(right)-handed quarks

and leptons are doublets(singlets) under $SU(2)_L$ transformations and are charged under $U(1)_Y$. The electromagnetic charge Q satisfy the condition $Q = Y/2 + T_3$, where T_3 is the third isospin component of the $SU(2)_L$ generator. The octet of gluons G^a_μ for the $SU(3)_C$ (C is the color charge) gauge group establishes the interactions of QCD by acting on $SU(3)_C$ triplets of quarks.

Both leptons and quarks are sorted into three generations. The lepton $SU(2)_L$ doublets are represented by the left-handed electron (e_L), muon (μ_L), and tau (τ_L) paired up with their corresponding left-handed neutrinos, ν^e_L, ν^μ_L and ν^τ_L respectively. The lepton $SU(2)_L$ singlets are represented by (e_R), muon (μ_R), and tau (τ_R), since right-handed neutrinos are not observed experimentally[1]. In the same fashion, the quark $SU(2)_L$ doublets are made up by left-handed u (up) and d (down), s (strange) and c (charm), t (top) and b (bottom) pairs while the $SU(2)_L$ singlets are made up by their right-handed equivalents.

Over the last four decades, the SM has proven to be an extremely successful description of Nature. It framed the elementary particles already known before its advent into a common picture and it predicted the existence of new particles that was later experimentally confirmed, e.g. the W boson in 1983 by the UA1 [20] and UA2 [22] Collaborations and the top quark in 1995 by the D0 [7] and CDF [10] Collaborations. The SM has been experimentally tested up to the TeV scale with high accuracy and only very few deviations have been observed.

1.1.1 Electroweak symmetry breaking and Higgs mechanism

In the SM, a perfectly conserved electroweak gauge symmetry would forbid mass terms for all field. However, this is not observed in Nature. In fact, the weak force carriers, the Z and W bosons, are massive and both leptons and quarks have non-zero masses as well.

This fact indicates that the electroweak gauge symmetry is preserved only at a hidden level and it is spontaneously broken. The mechanism to generate masses of gauge bosons by spontaneaously breaking the corresponding gauge symmetries was found 1964 independently by Higgs and Brout, Englert. The accordingly named *Higgs mechanism* or *BEH mechanism* (Ref. [85, 106, 107, 94, 108, 112]) The vacuum, left by the spontaneous breaking of the electroweak symmetric potential, which is non symmetric under a local gauge transformation, gives rise to a scalar field (Goldstone boson) whose unphysical degrees of freedom get absorbed into the longitudinal components

1 An indirect indication that right-handed neutrinos exist come from the observation of neutrino flavour oscillations, which are possible only in case the neutrinos have non zero mass. In the SM, fermion masses arise from the Yukawa coupling that connects the particle's left- and the right-handed fields.

of the gauge bosons Z and W, which, in turn, acquire mass. The remaining potential is still invariant under local $U(1)$ transformations, and this residual symmetry guarantees the photon to be massless. Fermions masses are generated indirectly, by Yukawa couplings to the introduced scalar field with degenerate vacuum state.

1.1.1.1 *The Higgs mechanism*

The Weinberg-Salam model of electroweak interaction is built upon a local $SU(2)_L \times U(1)_Y$ gauge invariance corresponding to the existence of three gauge bosons W^i_μ from $SU(2)$ and one B_μ from $U(1)$. Physical bosons γ, $W^\pm$, Z arise from a rotation of the gauge bosons eigenstates.

If the electroweak $SU(2)_L \times U(1)_Y$ symmetry is (partially) broken, the masses of the vector bosons arise. Massive W and Z bosons explain the short-ranged behaviour of the weak force. However, the symmetry is not completely broken, in fact a residual electromagnetic $U(1)_{EM}$ symmetry allows the photon to remain massless. In its simplest form, the Higgs mechanism postulates the existence of complex scalar doublet in order to break the symmetry.

$$\phi = \frac{1}{\sqrt{2}} \begin{pmatrix} \phi_1 + i\phi_2 \\ H + i\phi_0 \end{pmatrix} \tag{1}$$

In the SM, only one Higgs doublet is foreseen. The most general $SU(2)$-invariant scalar potential that can be expressed in terms of the ϕ field is

$$V(\phi) = \mu^2 |\phi^\dagger \phi| + \lambda (|\phi^\dagger \phi|)^2 \tag{2}$$

If the μ parameter is positive, then the gauge symmetry is preserved. The interesting case occurs for a negative μ. A negative-signed μ^2 shapes the V potential as in Fig. 1 and forces the field ϕ to acquire a non-null vacuum expectation value (VEV) $v = \sqrt{\mu^2/\lambda}$ (where λ is the coupling strength of the four point). Along the vacuum circle, the field ϕ is displaced from o. Since $V(\phi) = V(|\phi^\dagger \phi|)$, the direction of the minimum is not determined and we can operate an arbitrary $SU(2) \times U(1)$ transformation over ϕ leaving V unchanged[2]

$$\phi \to e^{iT^a \tau^a} e^{iY/2} \phi \tag{3}$$

and therefore we can chose $T^1 = T^2 = 0,\ T^3 = Y/2$

$$\langle \phi \rangle = \frac{1}{\sqrt{2}} \begin{pmatrix} 0 \\ v \end{pmatrix} \tag{4}$$

This choice leaves the electromagnetism unbroken, since $Y = 2(Q - T^3)$ we have

$$Q\langle \phi \rangle = 0 \tag{5}$$

2 The generators of this symmetry are Pauli matrices T^i and the hypercharge Y

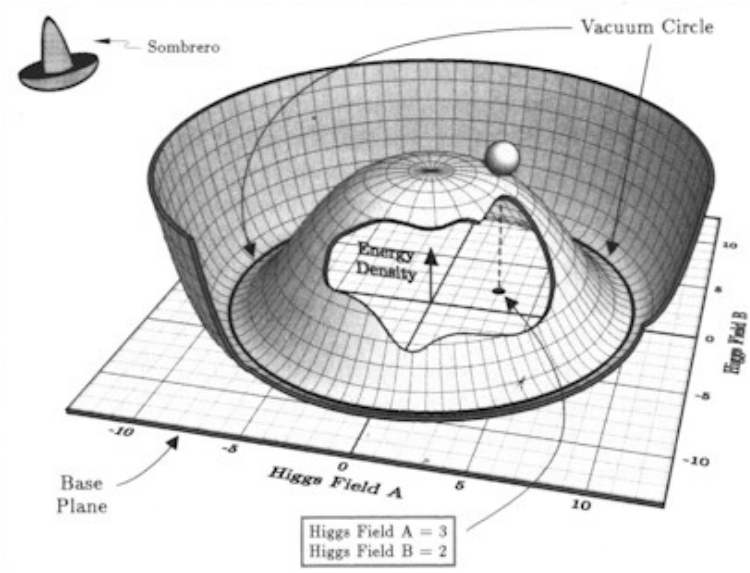

Figure 1: Higgs potential with $\mu < 0$. The Excitation of the field ϕ along the minimum of the potential is absorbed by the longitudinal polarisation of the W and Z bosons, thereby acquiring mass. The radial excitation corresponds in turn to the free particle associated to the Higgs field, i. e. the Higgs boson.

and the desired symmetry breaking scheme $SU(2)_L \times U(1)_Y \to U(1)_{EM}$ is obtained. Indeed this particular linear combination of the four generators, preserving the electromagnetic $U(1)_{EM}$ symmetry, underlies the existence of the massless photon, the three remaining degree of freedom are fulfilled by combination of the gauge bosons that lead to $W^{\pm}$ and Z physical bosons.

1.1.1.2 *Boson masses*

The electroweak gauge covariant derivative is

$$D_\mu \phi = \left(\partial_\mu - i g W^j_\mu \tau^j - i \frac{1}{2} g' B_\mu \right) \phi \tag{6}$$

where g and g' are the coupling strength of the $SU(2)_L$ and $U(1)_Y$ interactions. The kinetic energy term of the ϕ field in the EWK lagrangian is given by

$$\begin{aligned} \mathcal{L}_{KE} &= (D^\mu \phi)^\dagger (D_\mu \phi) \\ &= \frac{1}{2} (0 \; v) \left(g W^j_\mu \tau^j + \frac{1}{2} g' B_\mu \right) \left(g W^{k\mu} \tau^k + \frac{1}{2} g' B^\mu \right) \begin{pmatrix} 0 \\ v \end{pmatrix} \\ &= \frac{1}{2} \frac{v^2}{4} [g^2 (W^1_\mu)^2 + g^2 (W^2_\mu)^2 + (-g W^3_\mu + g' B_\mu)^2] \end{aligned} \tag{7}$$

the fields associated to the physical bosons are obtained from linear combination of the interaction eigenstates

$$W_\mu^\pm = \frac{1}{\sqrt{2}}(W_\mu^1 \mp iW_\mu^2) \qquad \text{charged currents} \tag{8a}$$

$$Z_\mu = \frac{-g'B_\mu + gW_\mu^3}{\sqrt{g^2+g'^2}} \qquad \text{neutral currents} \tag{8b}$$

$$A_\mu = \frac{gB_\mu + g'W_\mu^3}{\sqrt{g^2+g'^2}} \qquad \text{electromagnetic currents} \tag{8c}$$

The mixing of the third weak component W_μ^3 and the $U(1)_Y$ generator B_μ is typically expressed in terms of the Weinberg mixing angle θ_W defined by $\sin(\theta_W) = g'/\sqrt{g^2+g'^2}$ and $\cos(\theta_W) = g/\sqrt{g^2+g'^2}$. Eq. 8c connects θ_W with the electrical charge $e = g\sin\theta_W = g'\cos\theta_W$. The lagrangian for the Higgs field in the unitary gauge, can then be expressed as

$$\mathcal{L}_{Higgs} = \frac{1}{2}\partial_\mu H \partial^\mu H - \lambda v^2 H^2 \tag{9a}$$

$$+ \frac{1}{4}v^2 g'^2 W_\mu^+ W^{-\mu} \tag{9b}$$

$$+ \frac{1}{8}(g^2+g'^2)v^2 Z_\mu Z^\mu \tag{9c}$$

$$+ \frac{1}{2}g'^2 v H W_\mu^+ W^{-\mu} + \frac{1}{4}(g^2+g'^2)vHZ_\mu Z^\mu \tag{9d}$$

$$+ \frac{1}{4}g'^2 H^2 W_\mu^+ W^{-\mu} + \frac{1}{8}(g^2+g'^2)H^2 Z_\mu Z^\mu \tag{9e}$$

$$- \lambda v H^3 \tag{9f}$$

$$- \frac{1}{4}\lambda H^4 \tag{9g}$$

the mass terms for the W, $m_W = vg'/2$, and Z, $m_Z = v\sqrt{g'^+g^2}/2$, bosons appear in 9b and 9c respectively. An additional particle is foreseen in 9a, the Higgs boson, whose mass is $m_H = v/2\lambda$. The Eqs. 9f and 9g represent the Higgs triple and quartic self couplings. The Higgs potential is thus completely defined by two parameters, the v and λ. The VEV is related to the Fermi constant by the expression $G_F = \frac{g'^2\sqrt{2}}{8m_W^2}$. Since G_F is precisely measured in the $\mu \to e\nu_\mu\nu_e$ process and m_W is known, the numerical value for the Higgs VEV is $v = 246\,\text{GeV}$. The λ parameter can be fixed either directly, from measuring the Higgs quartic coupling, or indirectly from measuring the Higgs boson mass m_H.

1.1.1.3 *Yukawa coupling and fermion masses*

The electroweak lagrangian density written in Eq. 9 is not complete, in fact a new term $\mathcal{L}_F$, Eq. 10 (right handed neutrinos and the second

and third generation leptons and quarks are neglected) to regulate the fermionic interactions with the Higgs field has to be added

$$\mathcal{L}_F = -\lambda_e \bar{L}\phi e_R \tag{10}$$
$$-\lambda_d \bar{Q}\phi d_R \tag{11}$$
$$-\lambda_u \bar{Q}(i\sigma_2)\phi^\star u_R \tag{12}$$

The interaction between a fermionic Dirac field and the scalar Higgs field is know as Yukawa interaction, with λ named as Yukawa coupling.

By substituting explicitly writing the expression for the Higgs field $(0, 1/\sqrt{2}\cdot(v+H))$ in place of ϕ in Eq. 10, Dirac mass terms for the fermions $m_f \bar{f} f$ arise with

$$m_f = \frac{\lambda_i v}{\sqrt{2}} \tag{13}$$

with $i = e, u, d$, and the analogously for the second and third generations. It is therefore evident that the fermionic Higgs coupling are directly proportional to the mass of the fermion.

1.1.2 SM Higgs production at LHC

At the LHC, the SM predicts 4 major production mechanism to contribute to the overall cross-section of the Higgs boson: gluon–gluon fusion (ggH), vector boson fusion (VBF or qqH), vector boson associated production (VH) via Bremsstrahlung and top-quark associated production. The corresponding Feynman diagrams are shown in Fig. 2. The corresponding cross-sections as predicted by the SM as a function of the mass of the Higgs boson, as well as with fixed $m_H = 125\,\text{GeV}$and as a funtion of the center-of-mass energy, are shown in Fig. 3.

Higgs boson production rates via gluon fusion exceed the other production mechanisms by at least one order of magnitude. The Higgs boson production cross-sections for the gluon fusion, vector boson fusion and W/Z and top-quark associated production mechanisms at the LHC for Higgs masses equal to 125 GeVare 19.27 pb, 1.58 pb, 0.70 pb, 0.42 pb and 0.13 pb.

Gluon–gluon fusion The Higgs boson production via gluon–gluon fusion is mediated by triangular loops of quarks. Since the Higgs coupling strength is proportional to the mass of the fermions 1.1.1.3, top loops dominate whilst bottom loops are still not negligible and accounted for in the MC simulation. Due to the enhanced partonic gluon luminosity at high energies and the large couplings to especially top-quarks, the production mechanism has the largest contribution to the overall Higgs production cross-section. The cross section is highly dependent

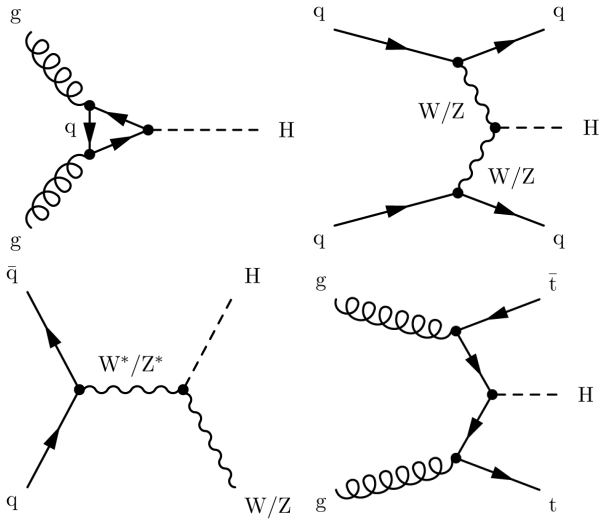

Figure 2: Dominant Feynman diagrams for the LHC Higgs production mechanisms. Gluon-gluon fusion (top-left), vector boson fusion (top-right), W/Z associated production (bottom-left) and top-quark associated production (bottom-right).

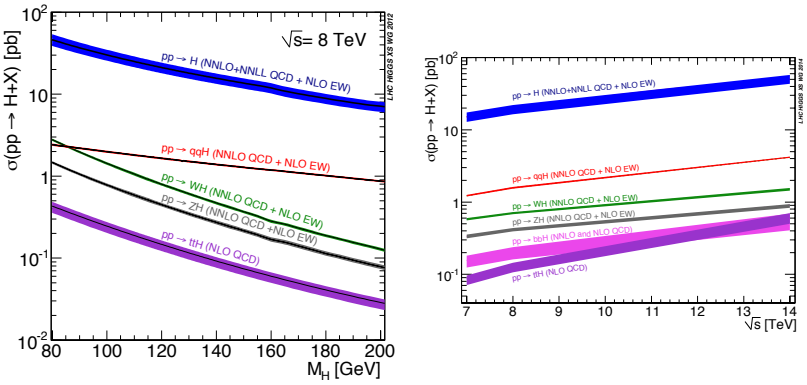

Figure 3: Higgs production cross sections at the LHC including NNLO QCD and NLO electroweak higher order corrections as a function of m_H for the center of mass energy of 8 TeV (left). Higgs production cross sections at the LHC including NNLO QCD and NLO electroweak higher order corrections as a function of center of mass energy from 7-14 TeV or $m_H = 125$ GeV(right).

on higher order QCD corrections. Up to next-to-leading order (NLO) in α_s, the cross section prediction has been calculated

maintaining the full dependency on the Higgs and top- and bottom-quark masses. The NLO corrections increase the leading order prediction by about 80%. Additionally, the NNLO contributions have been calculated in the approximation of the large top-mass limit, increasing the cross section by about 20%. NLO electroweak contributions have been computed to further enhance the cross section by about 5%. Matching of the NNLO hard scattering matrix element to the soft-gluon contributions at next-to-next-to-leading logarithm (NNLL) accuracy have been achieved.

Vector Boson Fusion The VBF production of the Higgs boson has the second largest contribution to the overall cross-section of the Higgs boson at the LHC, as shown in Fig. 2. The process is induced by t- and u-channel Z or W boson exchange interaction of two (anti-)quarks of the incoming protons, with the Higgs boson being radiated off the weak bosons, linking the two quarks. VBF production via W bosons exceeds the one with Z bosons by a factor of about 3, due to the larger W coupling to fermions. The VBF production mechanism leads to a distinct final state topology with two jets in the final state. Due to the absence of color exchange at leading order between the two incoming protons (weak bosons are color singlets), additional gluon radiation in the central rapidity region between the two final-state quarks is strongly suppressed, and the quarks color connect with the respective proton remnant. This leads to two highly energetic jets at large pseudo-rapidity and the two opposite hemispheres. As opposed to other Higgs production mechanisms and to most of background processes, the presence of additional energetic jets in the pseudo-rapidity region comprised between the two forward jets is disfavoured. Furthermore, despite also the Z boson could be produced via VBF, with an identical topology as the Higgs VBF process, this process is suppressed by g'^4 whereas the Higgs production through VBF is enhanced, because of the high mass of the vector bosons to which the Higgs couples with m_V^2. The VBF cross section predictions have been calculated including NNLO QCD and NLO electroweak contributions of about 5-10%, respectively.

Z/W+H and tt+H The Higgs boson production via Bremstrahlung off weak vector bosons and heavy quark associated Higgs production processes, are additional important LHC Higgs production mechanisms. The cross sections at the LHC are low compared to the gluon-gluon fusion and VBF production cross sections. In the $H \to \tau_h\tau_h$ analysis, these processes are inclusively taken into account. However due to the small corresponding production cross sections no dedicated strategy is pursued to

exploit the distinct production signatures. In the context of the general $H \to \tau\tau$ CMS search, the Z/W+H production process is specifically searched for by dedicated analyses that exploit the leptonic decays of the associated vector boson. Top-pair associated Higgs boson production, provides direct sensitivity to the top-quark Yukawa coupling of the Higgs boson, and the CMS and ATLAS collaborations pursued dedicated analyses to study this production mode for several Higgs boson decay modes. For W/Z associated Higgs production the cross section was calculated with NNLO QCD accuracy, increasing (mostly NLO corrections of Drell-Yan type) the LO cross section by about 30%. Electroweak NLO corrections have been calculated and they enhance the cross-section by 5-10%. The cross section for ttH production is only known up to NLO QCD accuracy, increasing the LO cross section at the LHC by about 20%.

1.1.3 Search and discovery of a Higgs boson

The direct search for a Higgs boson has been a longstanding endeavour in particle physics. Moreover, since the Higgs mechanism is a fundamental part of the electroweak sector in the SM, the existence of a Higgs boson can also be indirectly tested through precise measurements of the SM interactions. At the Large-Electron Positron collider (CERN) an extensive programme of indirect and direct searches was deployed. No direct evidence was found, and a limit at 95% CL was set at $114.4 < m_H < 246\,\text{GeV}$ [23]. At the Tevatron $p - \bar{p}$ collider (Fermilab) the direct search for a Higgs eventually led, in 2012, to observe an excess around $m_H = 135\,\text{GeV}$, with significance of about 3 standard deviations, in the $H \to b\bar{b}$ channel [6].

On the 4^{th} of July 2012, the ATLAS and CMS Collaborations announced the observation of a new boson with mass around 125 GeV compatible with the SM Higgs boson [38, 3, 41]. The search was carried out in the $H \to ZZ$, $H \to W^+W^-$, $H \to \gamma\gamma$, $H \to \tau^+\tau^-$, $H \to b\bar{b}$ channels. Both ATLAS and CMS observed an excess, mainly in the bosonic channels (mass plots for he high resolution channels $\gamma\gamma$ and ZZ are in Fig. 4), with significance larger than 5 standard deviations. The properties of this newly observed particle were found to be consistent, within the current experimental accuracy, with the SM Higgs boson in terms of spin, parity and couplings, Fig. 5.

1.2 THE MINIMAL SUPERSYMMETRIC STANDARD MODEL

The SM particle masses and interactions have been tested with outstanding accuracy in many experiments, proving that the SM pro-

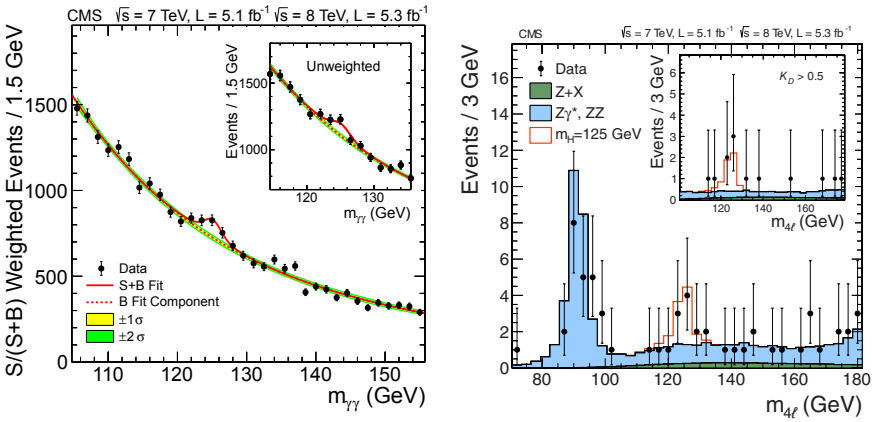

Figure 4: Di-photon and four-lepton mass distributions for the $\gamma\gamma$ (left) and ZZ (right) channels, respectively, in CMS at the time of the Higgs discovery. An excess around $m_H = 125\,\text{GeV}$ is visible in both plots.

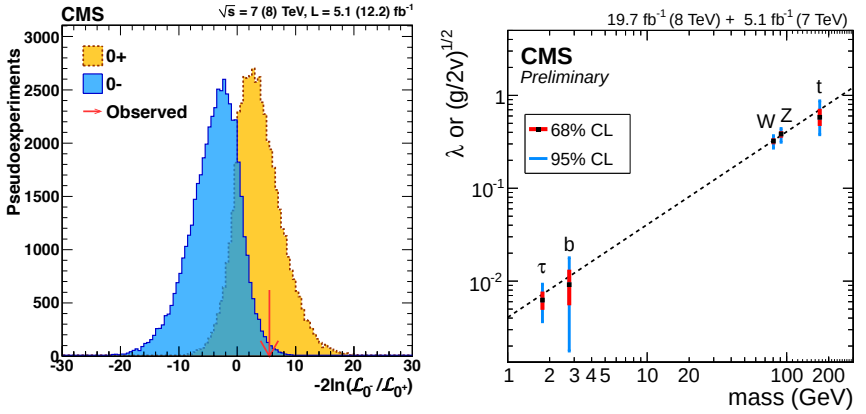

Figure 5: Spin parity hypothesis test (left). Higgs coupling strength (square root of the coupling strength, divide by twice the VEV for the vector bosons) as a function of the mass of the particle (right). The mass of the bottom quark is evaluated at the Higgs mass scale $m_b(mH = 125.7\text{GeV}) = 2.763\,\text{GeV}$. The new particle behaves as a scalar and its couplings depend on the mass (or the square of). This is in excellent agreement with the SM Higgs. These plots refer to the latest public CMS results on the full Run I statistics.

vides a firm description of Nature up to the threshold of the TeV scale with no hints of additional structures. However, the SM is thought not to be a completely exhaustive theory. In fact, a number of theoretical and experimental issues cannot be solved within the framework of the SM:

Hierarchy and unification: the coupling of the fundamental forces span over tens of order of magnitudes and, albeit running, do not converge event at very high energy, e. g. Plank or GUT scale 10^{16-18}.

Naturalness: the finiteness (and lightness) of the Higgs mass is possible only through an massive *fine tuning* of the radiative correction cancellations;

Dark Matter: no SM particles is a good candidate to explain the Dark Matter (DM);

Bariogenesis: the "amount" of CP violation predicted in the SM is greatly insufficient to explain the large matter/anti-matter asymmetry observed in Nature

The hierarchy and the naturalness problems are intimately related, in fact, the SM can be regarded as an effective theory, valid in a certain range of energies, from the MeV up to an unknown scale Λ. Its low energy quantities (masses, couplings) are expected to be functions of the parameters of a more fundamental theory valid at a scale $Q > \Lambda$. The one-loop quantum corrections to the Higgs boson mass depend on the Higgs coupling to bosons (λ_V) and fermions (λ_f), their masses (m_f and m_V) and on the cutoff scale Λ:

$$\Delta m^2 = \frac{|\lambda_f^2|}{16\pi^2}\left[-2\Lambda^2 + m_f^2 \ln\frac{\Lambda}{m_f}\right] + \frac{\lambda_V}{16\pi^2}\left[\Lambda^2 + m_V^2 \ln\frac{\Lambda}{m_V}\right] \quad (14)$$

If naturalness is considered as a desirable feature of a theory, the quantum correction to the Higgs mass cannot be too large, since m_H is as low as 125 GeV Fig. 6. From eq. 14 it is clear that this correction is quadratically divergent with respect to Λ. Therefore, to keep the correction small, Λ should be $\leqslant 1$ TeV or an extremely fine tuning of the parameters should occur.

1.2.1 Supersymmetry overview

The Supersymmetric extension of the SM (SUSY) [118] proposes a neat solution to the hierarchy and naturalness problems. Referring to eq. 14, if there were two scalars for each fermion, then it would read:

$$\Delta m^2 = \frac{\lambda_V - |\lambda_f^2|}{8\pi^2}\Lambda^2 + \mathcal{O}\left(\ln\frac{\Lambda}{m}\right) + \dots \quad (15)$$

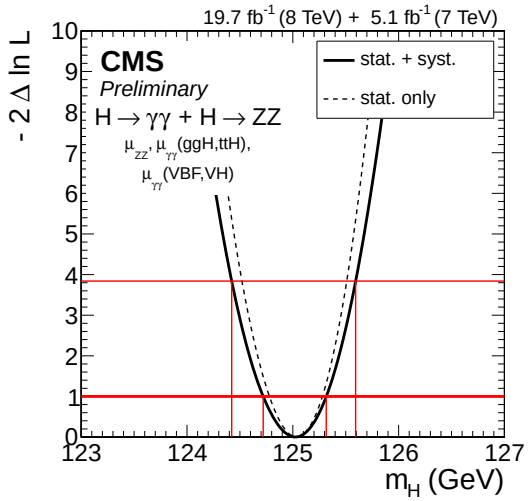

Figure 6: Higgs boson mass, as measured by CMS. $m_H = 125.03^{+0.26}_{-0.27}\text{stat.}^{+0.13}_{-0.15}\text{syst. GeV}$.

in addition, requiring that the couplings are $\lambda_V = |\lambda_f^2|$, the quadratic divergence exactly cancels out, Fig. 7:

$$\Delta m^2 = \mathcal{O}\left(\ln \frac{\Lambda}{m}\right) + \dots \tag{16}$$

Therefore, if a symmetry between fermions and bosons existed such that for each fermion (boson) implied the presence of a bosonic (fermonic) counterpart with the same coupling to the Higgs and the same mass (at least before soft symmetry breaking occurs), then the hierarchy problem would be solved. A further internal symmetry is therefore introduced: *Supersymmetry*. The supersymmetry generators Q have the following properties:

- $Q|\text{fermion}\rangle = |\text{boson}\rangle, \quad Q|\text{boson}\rangle = |\text{fermion}\rangle$;
- commutation rules: $\{Q, Q^\dagger\} = P^\mu$, $\{Q, Q\} = \{Q^\dagger, Q^\dagger\} = 0$ and $[P^\mu, Q] = [P^\mu, Q^\dagger] = 0$, P^μ being the 4-momentum operator.

The effect of Q is to transform SM particles into their Supersymmetric partners, namely *Superpartners*. The pair of a particle and its superpartner is called *supermultiplet* and contains both fermions and bosons.

From the properties above, it turns out that, for every Supermultiplets, superpartners must have the same masses and the same couplings. Supermultiplets have two states of helicity, λ_{max} and $\lambda_{min} = \lambda_{max} - 1/2$, thus swapping from fermions to bosons and viceversa.

Since there is no experimental evidence of superpartners having exactly the same mass as their SM siblings, a soft supersymmetry breaking (SSB) is conjectured. This mechanism assignes to the supersymmetric particles masses that are larger than their SM counterparts. One of the goals of LHC is the search for SUSY particles.

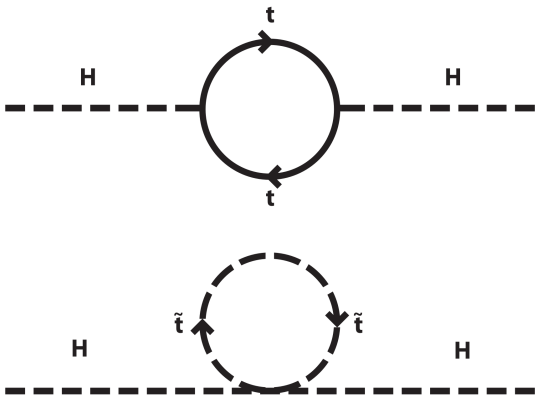

Figure 7: Higgs mass radiative corrections due to top (up) and its supersymmetric partner, stop (bottom), loop diagrams. Both contributions are present in SUSY and, whilst both are quadratically divergent, they are opposite phased and perfectly cancel out each other. In the SM only the former is present and it diverges quadratically.

Two kinds of Supermultiplets can be defined: *Chiral* and *Vector* Supermultiplets. Chiral (or Matter) Supermultiplets are composed of a state with $\lambda_{max} = 1/2$ and the other one with $\lambda_{min} = 0$. The simplest example is a Weyl fermion and two real (one complex) scalars called *sfermion*. Vector (or Gauge) Supermultiplets, instead, have $\lambda_{max} = 1$ and $\lambda_{min} = 1/2$ like, for example, a gauge vector boson and a fermion called *gaugino*.

The simplest Supersymmetric extension of the SM, called *Minimal Supersymmetric Standard Model* (MSSM) hypnotizes the existence the super partners of the SM particles and does not add any other particle to the scheme.

Indeed, the only difference with respect to the SM is the presence of two complex Higgs doublets instead of one. In fact, in the SM Lagrangian, H gives mass to up-type quarks, while its conjugate H^c to down-type fermions. The invariance of the Lagrangian under supersymmetric transformation requires the existence of two different scalar fields, in order to give mass to up- and down- fermions.

In the end, it is worth mentioning that the MSSM could not only provide a proper solution to the hierarchy problem, but also predicts the existence of the *neutralino*, the superpatrner of the neutrino, which is a weakly interactive particle and an interesting candidate for Dark Matter. Moreover, MSSM allows for a Grand Unification when $M_{GUT} \simeq 10^{16}$ is approached.

1.2.2 The Higgs sector in the MSSM

The MSSM requires two complex Higgs doublets in order to cancel loop corrections in perturbative process. The two doublets are:

$$H_u = \frac{1}{\sqrt{2}} \begin{pmatrix} H_u^+ \\ H_0 \end{pmatrix} \qquad H_d = \frac{1}{\sqrt{2}} \begin{pmatrix} H_0 \\ H_d^- \end{pmatrix} \tag{17}$$

where H_d couples only with down-type fermions and H_u couples only to up-type fermions.

The MSSM Higgs scalar potential is expressed as:

$$\begin{aligned} V \; = & (|\mu|^2 + m_{H_u}^2)(|H_u^0|^2 + |H_u^+|^2) + \\ & (|\mu|^2 + m_{H_d}^2)(|H_d^0|^2 + |H_u^-|^2) + \\ & [b(H_u^+ H_d^- - H_u^0 H_d^0) + \text{c.c.}] + \\ & \frac{1}{8}(g^2 + g'^2)(|H_u^0|^2 + |H_u^+|^2 - |H_d^0|^2 - |H_d^-|^2)^2 + \\ & \frac{1}{4} g^2 |H_u^+ H_d^{0*} + H_u^0 H_d^{-*}|^2 \end{aligned} \tag{18}$$

and, given the residual gauge freedom, it is possible to transform the fields in order to obtain $H_u^+ = H_d^- = 0$ and H_u^0 and H_d^0 real and positive in the minimum, thus rewriting the potential as follows:

$$\begin{aligned} V \; = & (|\mu|^2 + m_{H_u}^2)(|H_u^0|^2) + \\ & (|\mu|^2 + m_{H_d}^2)(|H_d^0|^2) + \\ & [b H_u^0 H_d^0 + \text{c.c.}] + \\ & \frac{1}{8}(g^2 + g'^2)(|H_u^0|^2 - |H_d^0|^2)^2 \end{aligned} \tag{19}$$

In the minima of the Higgs potential, the electroweak symmetry breaking occurs, and the two Higgs fields acquire, separately, the two vacuum expectation values v_u and v_d, as in Eq. **??**.

$$labeleq : vev - mssm \langle H_u \rangle = \frac{1}{\sqrt{2}} \begin{pmatrix} v_u \\ 0 \end{pmatrix} \qquad \langle H_d \rangle = \frac{1}{\sqrt{2}} \begin{pmatrix} 0 \\ v_d \end{pmatrix} \tag{20}$$

which are related to each other through the formula in Eq. 21, that involves the W boson mass.

$$v^2 = v_u^2 + v_d^2 = 4 m_W^2 / g^2 \simeq (174 \text{ GeV})^2 \tag{21}$$

The ratio between the vacuum expectation values is parametrised as

$$\tan \beta = \frac{v_u}{v_d}$$

The diagonalization angle of the neutral Higgs bosons mass matrix is α.

From the diagonalization of the mass matrices and requiring the field to be in the minimum, the following Higgs mass eigenstates arise:

- Two CP-odd neutral scalars

$$\begin{pmatrix} G^0 \\ A^0 \end{pmatrix} = \sqrt{2} \begin{pmatrix} \sin\beta & -\cos\beta \\ \cos\beta & \sin\beta \end{pmatrix} \begin{pmatrix} \mathfrak{I}H_u^0 \\ \mathfrak{I}H_d^0 \end{pmatrix} \tag{22}$$

- Four charged scalars

$$\begin{pmatrix} G^\pm \\ A^\pm \end{pmatrix} = \begin{pmatrix} \sin\beta & -\cos\beta \\ \cos\beta & \sin\beta \end{pmatrix} \begin{pmatrix} H_u^\pm \\ H_d^\pm \end{pmatrix} \tag{23}$$

- Two CP-even neutral scalars

$$\begin{pmatrix} h^0 \\ H^0 \end{pmatrix} = \sqrt{2} \begin{pmatrix} \cos\alpha & -\sin\alpha \\ \sin\alpha & \cos\alpha \end{pmatrix} \begin{pmatrix} \mathfrak{R}H_u^0 \\ \mathfrak{R}H_d^0 \end{pmatrix} \tag{24}$$

$G^\pm$ and G^0 are the Goldstone bosons that give mass to the $W^\pm$ and Z bosons, while $H^\pm$, h^0, H^0 and A^0 are the physical degrees of freedom.

At the tree level, the Higgs sector is described by two parameters only: $\tan\beta$ and m_A. The Higgs masses are defined in the following equations

$$m_A^2 = \frac{2b}{\sin(2\beta)} = 2|\mu|^2 + m_{H_u}^2 + m_{H_d}^2 \tag{25}$$

$$m_{H^\pm}^2 = m_A^2 + m_W^2 \tag{26}$$

$$m_{H,h}^2 = \frac{1}{2}(m_A^2 + m_Z^2 \pm \sqrt{(m_A^2 + m_Z^2)^2 - 4m_A^2 m_Z^2 \cos^2(2\beta)}) \tag{27}$$

the different masses are organized into a hierarchy:

$$m_{H^\pm}^2 > m_A^2 \qquad m_h \leqslant m_A \leqslant m_H \qquad m_h < |\cos(2\beta)| m_Z \tag{28}$$

If $m_A \gg m_Z$ (*decoupling limit*), the equation (27) can be written is a simplier form:

$$m_H^2 = m_A^2 + m_Z^2 \sin^2(2\beta) \qquad m_h^2 = m_Z^2 \cos^2(2\beta) \tag{29}$$

thus, for high $\tan\beta$ values, A and H masses and couplings degenerate and, together with $H^\pm$, form an isospin double. Moreover h acquires a much lower mass.

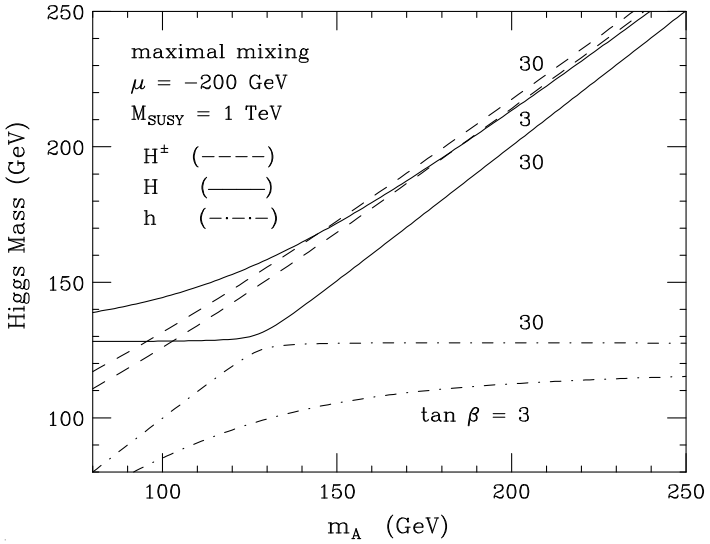

Figure 8: Mass of the heavy, CP-even neutral Higgs boson H versus the mass of the CP-odd neutral Higgs boson A, for different values of the parameter $\tan\beta$. In the decoupling limit and for high values of $\tan\beta$, the A boson is degenerate with the light neutral Higgs boson h and with H for low and high m_A respectively. Despite the third equation in Eq. 29 bounds h mass to be smaller than m_Z, large radiative corrections can shift the upper bound on m_h up to about 135 GeV, as shown in this plot.

	Down-type quarks Lepton pairs	**Up-type quarks**	**$W^{\pm}$, Z**
h	$-\sin\alpha/\cos\beta$	$\cos\alpha/\sin\beta$	$\sin(\beta-\alpha)$
H	$\cos\alpha/\cos\beta$	$\sin\alpha/\sin\beta$	$\cos(\beta-\alpha)$
A	$-i\gamma_5\tan\beta$	$-i\gamma_5\cot\beta$	0

Table 2: Rescaling factor fot Higgs couplings to SM particles in MSSM.

The couplings of the Higgs bosons to SM particle in the MSSM mirror the usual SM behavior except for a α or β dependent rescaling factor.

In Ch. 4, the search for a neutral MSSM Higgs boson ϕ (ϕ indicates either one of the three MSSM neutral Higgs bosons A, H, h, which are, in certain configurations of the parameter space degenerate Fig. 8) decaying into a pair of tau leptons is presented. The coupling of the A boson with down-type fermions is proportional to $\tan\beta$, therefore, for moderate to high values of $\tan\beta$, the Higgs to taus decay rate is enhanced and the di-tau becomes a very sensitive search channel.

The SSB mechanism preserves the structure of the theory, does not affect the cancellation of the quadratic divergences of eq: 14, being

only couplings are involved, but allows to give different masses to SM particles and their Superpartners.

The definition of few additional parameters are required in order to sketch a complete description of the MSSM, nominally the SSB mass M_{SUSY}, the *gaugino* mass M_2, the *Higgs mass parameter* μ, the Higgs coupling at the electroweak scale A and the *gluino* mass $m_{\tilde{g}}$. Different theoretical scenarios are defined by setting the values of these parameters. In Ch. 4 exclusion limits are extracted for various scenarios defined by different configuration of these parameters.

2 THE COMPACT MUON SOLENOID DETECTOR

2.1 THE LARGE HADRON COLLIDER

The Large Hadron Collider (LHC) at CERN, Geneva, is a proton-proton collider[1] built to address the key unresolved questions in particle physics. It was designed to provide the high luminosity and the high center of mass energy, which are crucial in order to investigate rare events of new physics.

The LHC was designed to provide $proton - proton$ collisions with a center of mass energy of $\sqrt{s} = 14$ TeV at an instantaneous luminosity up to to $\mathcal{L} = 10^{34}$ cm^{-2}s^{-1}. The high luminosity of the LHC is obtained by a high frequency of bunch crossing and densely populated bunches: each beam contains up to 2808 bunches, each bunch consists of 1.15×10^{11} protons providing a collision rate of 40 MHz. Each bunch crossing can generate tens of low transverse momentum particles, the so called *minimum bias* events. Usually these events are of little physical interest, but contribute to enhance the *pile-up* (PU) (Fig. 9), which has a deleterious impact on the reconstruction performances. In fact, due to the finite spacial granularity of the detector, particles produced in a given bunch crossing that are close to each other are effectively reconstructed as aa single particle. Moreover, particle identification algorithms that exploit information from relatively large regions of the detector, such as the isolation, can be particularly spoilt by PU. The spatial, in-time component of the PU gets worse as the particle multiplicity increases. A time component of PU is also present: particles produced in two distinct bunch crosses are overlap because of the limited time resolution of the detector.

Thus the high interaction rate and multiplicity required the detectors to have a very fast response time (25-50 ns) and fine granularity in order to reduce the *pile-up*. An online and offline trigger system has been implemented in order to efficiently select only interesting events rejecting most of background and reducing detector dead time.

The two colliding beams orbit around the LHC ring inside a continuous vacuum tube passing through 1232 dipole bending magnets.

1 It is also able provide heavy ions collisions. In fact the study of physics phenomena such as the quark-gluon plasma, accessible only through heavy ions collisions, are part of the vast physics programme of the LHC. ALICE, one of the four large scale experiments installed along the LHC ring, is specifically designed for the heavy ions physics.

Since protons travel with an energy as high as 7 TeV and the beam pipe has a bending radius R ~ 2780 m, the required magnetic field is B = 8.4 T, achieved by the NiTi superconductive dipole magnets, kept cool at 1.9 K by a huge liquid He cryogenic system. A current of about 12 kA passes trough the magnets.

The first run of data taking took place during the 2010-2012 period, with a center-of-mass energy of 7 TeV during the first two years and of 8 TeV during the last year. The maximum instantaneous luminosity reached by the machine during Run I is $\mathcal{L} = 7 \cdot 10^{33}$ $cm^{-2}s^{-1}$. During this running period, the LHC delivered an integrated luminosity of about $6fb^{-1}$ at $\sqrt{s} = 7$ TeV and about $23fb^{-1}$ at $\sqrt{s} = 8$ TeV, Fig. 10. The next data taking, Run II, will start in 2015: the machine is expected to eventually reach the design center-of-mass energy and even exceed the design luminosity.

The LHC is installed in the former LEP tunnel which measures 27 km in circumference and is buried 100 m underground on average. The older CERN's accelerators, LINAC ($E_{beam} = 1.4$ GeV), PS ($E_{beam} = 25$ GeV) and SPS ($E_{beam} = 450$ GeV), provide the preliminary acceleration stages for protons before being injected in the LHC.

2.2 PHYSICS GOALS AT LHC

The LHC physics programme pursues mainly these following goals:

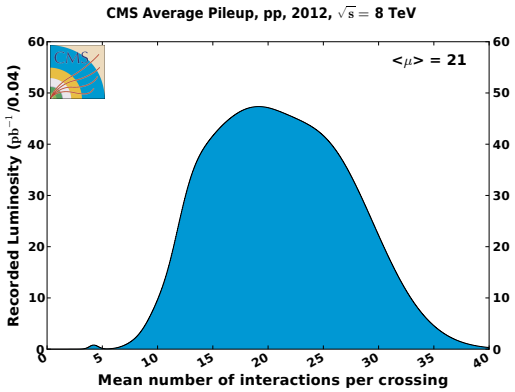

Figure 9: Recorded luminosity as a function of the number of interactions per bunch crossing, as measured by the CMS experiment during 2012. On average, 21 p–p collisions, that can be broadly identified with the number of primary vertices present in the event, occur at the same time at each bunch crossing, and the so produced particles overlap in the detector and degrade the object reconstruction performances. To mitigate the effect of the PU, ingenuous techniques have been developed.

SEARCH FOR THE HIGGS BOSON: in the SM, the Higgs mechanism explains particle masses by breaking spontaneously the electroweak symmetry. As a consequence, a corresponding scalar, massive particle, the Higgs boson, is predicted.On July 4th 2012, the ATLAS and CMS Collaborations announced the observation of a scalar particle, with mass around 125 GeV. The measurements of the couplings and the quantum numbers of this particle are in good agreement with the expectation for a SM Higgs boson [3, 41, 38].

LOOK FOR BEYOND THE STANDARD MODEL PHYSICS, e. g., evidence for supersymmetry (SUSY). This symmetry relates elementary particles to other particles that differ by half a unit of spin (superpartners), so that for every type of boson (fermion) there exists a corresponding type of fermion (boson). SUSY models are very attractive from a theoretical point of view, because they could solve a number of problems that can otherwise not be explained in the SM, most notably the fine tuning problem and the unification of forces. A more complete description of the motivations for SUSY models is given in Sec. 1.2.

ANSWER TO OPEN PROBLEMS IN THE SM: at TeV energy scale and beyond, many issues could be clarified, such as the origin of the matter-antimatter asymmetry in the universe and the existence of dark matter candidates.

PERFORM PRECISION MEASUREMENTS OF SM: the LHC will also allow to study of QCD, electroweak, and flavour physics. Measuring properties of the known particles with the highest precision as possible is a complementary approach to direct searches for particles, in fact, any deviation from the SM expectation is a signal of new physics.

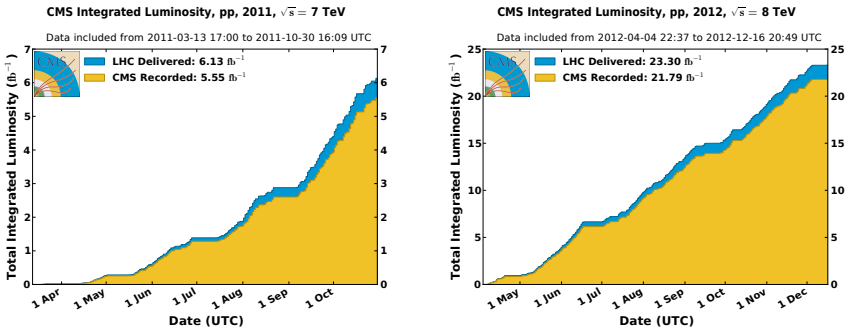

Figure 10: Integrated luminosity delivered (blue) by the LHC and recorded by the CMS experiment, described in Sec. 2.3, in 2011 (left) and 2012 (right), as a function of time.

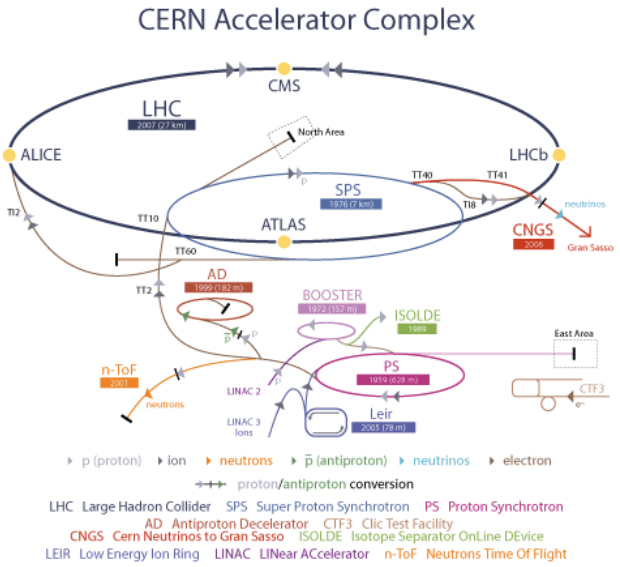

Figure 11: Accelerator facilities at CERN. Protons running in the LHC are pre-accelerated up to 450 GeV by several booster stages. Four large scale, CMS, ATLAS, ALICE and LHCb experiments are installed in the intersection points of the LHC.

Four large scale experiments are installed along the LHC: CMS, a general purpose experiment, described in section 2.3, ATLAS, the other multi purpose detector that shares the main physics goals with CMS but employs different subdetector technologies, ALICE, whose aim is to investigate the gluon-quark plasma generated in Heavy Ions collisions and LHCb, focussed on the b-quark study, heavy flavors physics and CP violation.

2.3 THE CMS DETECTOR

The *Compact Muon Solenoid* (CMS), located in LHC Point 5, has a typical collider detector design: it is barrel shaped, enclosed by two end caps, covering the full 4π solid angle (hermetic up to pseudorapidity $\eta = 5$, corresponding to $\theta \simeq 0.8$, 2.3.1), as sketched in fig 12. The overall dimensions of the CMS detector are 21.6 m (length) $\times$ 14.6 m (diameter) for a total weight of 12500 tons.

It features, from the collision point outwards (Fig. 13), an inner pixel/strips silicon tracker, lead glass fully active scintillating electromagnetic calorimeter, sampling hadronic calorimeter, 3.8 T superconductive solenoidal magnet and, at last, the muon chambers interleaved with the iron return yoke.

The detector requirements for CMS [60] [61] to meet the goals of the LHC physics programme can be summarized as follows:

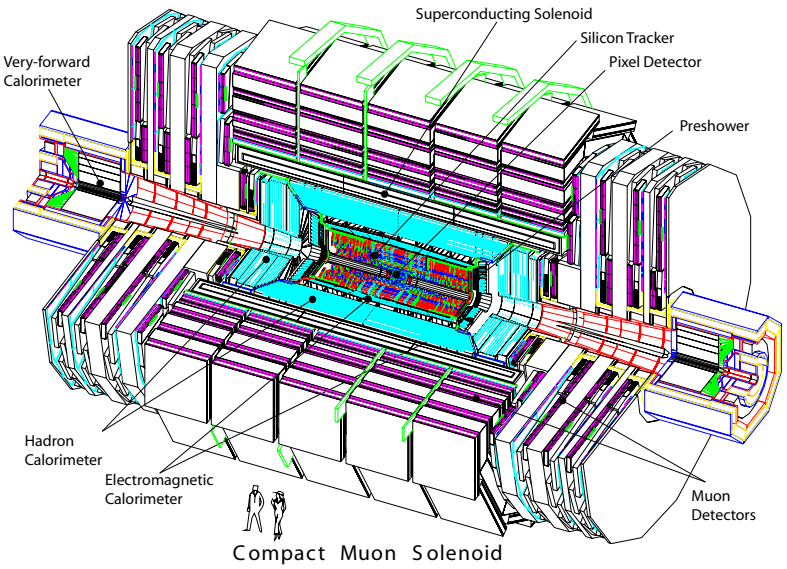

Figure 12: Synoptic view of the CMS detector

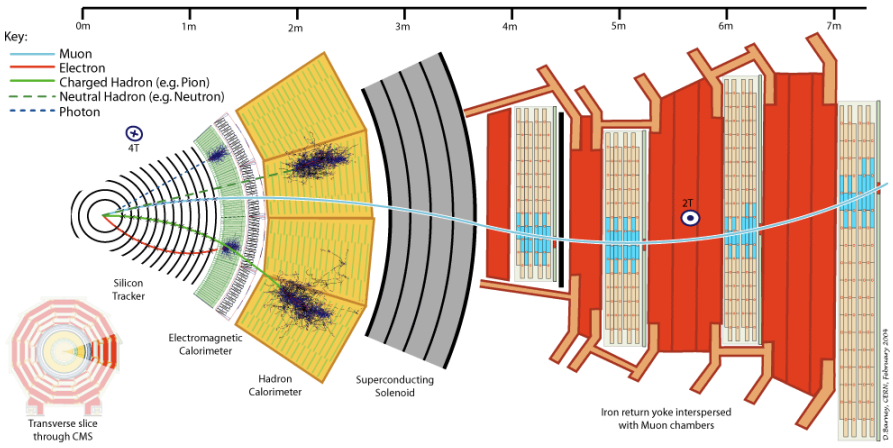

Figure 13: Transverse section of the barrel region of the CMS detector. The typical experimental signatures of the detectable, stable particles are reported. Neutrinos escape the detector without interacting and manifest themselves as missing transverse energy, $\not{E}_T$.

- Good muon identification and momentum resolution over a wide range of momenta in the region $|\eta| < 2.5$, good dimuon mass resolution, and the ability to determine unambiguously the charge of muons with $p < 1$ TeV.

- Good charged particle momentum resolution and reconstruction efficiency in the inner tracker. Efficient triggering and offline tagging of τ and b jets, requiring pixel detectors close to the interaction region.

- Good electromagnetic energy resolution, good diphoton and dielectron mass resolution ($\approx$ 1% at 100 GeV), wide geometric coverage ($|\eta| < 2.5$), measurement of the direction of photons and correct localization of the primary interaction vertex, π^0 rejection and efficient photon and lepton isolation at high luminositiy.

- Good $\not{E}_T$ and di-jet mass resolution, requiring hadron calorimeters with a large hermetic geometric coverage ($|\eta| < 5$) and with fine lateral segmentation.

2.3.1 Coordinate system

The coordinates system in CMS are chosen with the z axis along the beam direction, the x axis directed towards the center of the LHC ring and the y axis directed upward, orthogonally to the z and x axes. The origin is set in the nominal interaction point and the system is right handed.

Another commonly used coordinate set exploits the cylindrical structure of the detector: r, ϕ, η where r is the distance from the from the beam axis in the transverse plane, ϕ the azimuthal angle in the transverse plane and η is the *pseudorapidity* defined as $\eta = -\ln(\tan(\theta/2))$, where θ is the angle from the beam axis.

2.3.2 Magnet

The huge superconductive magnet [56] is the core feature of the CMS, allowing for strong bending power, 3.8 T, crucial to achieve fine track momentum resolution, especially for muons.

The solenoid is made up of 4 layers of NbTi superconductor. It is housed in a liquid He cryostat measuring 13 m long and 5.9 m inner diameter. At a nominal current of 20 kA, the stored energy in the magnet is 2.6 GJ. The 2 T return field flows in an iron yoke, allowing four layers of muon chambers to be housed in it, ensuring robustness and full geometric coverage.

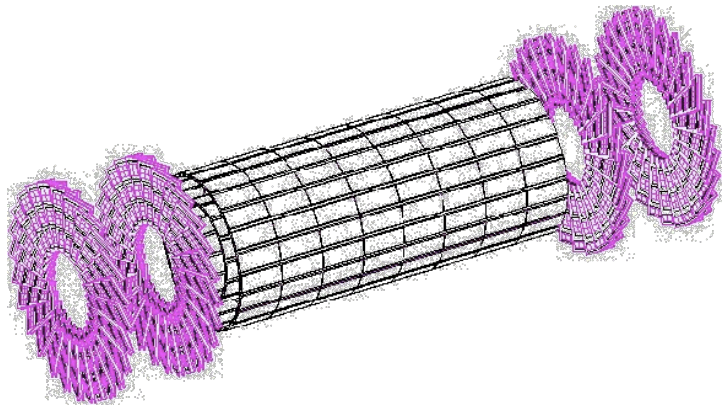

Figure 14: The inner pixel detector. The three barrel layers and the two disks of the endcap with blades disposed in a turbine-like shape are visible.

The field in the outer region is opposite to the field in the inner region, thus the muons trajectories are bended in two opposite directions, improving the momentum resolution.

2.3.3 Inner Tracking System

The Tracker is the innermost subdetector in CMS placed in the 3.8 T magnetic field, it determines the interaction vertex, the secondary vertices and measures the momentum of charged particles. It is designed in order to operate despite the hard radiation flux spreading from the interaction point. Nonetheless some degradation over the operational time occurs.

Three regions can be defined in the tracker, considering the charged particle flux at various radii:

1. Closest to the interaction vertex where the particle flux is the highest ($\approx 10^7$/s at $r \approx 10$ cm), pixel detectors are placed. The size of a pixel is $\approx 100 \times 150$ μm^2, giving an occupancy of about 10^{-4} per pixel per bunch crossing.

2. In the intermediate region ($20 < r < 55$ cm), the particle flux is low enough to enable use of silicon microstrip detectors with a minimum cell size of 10 cm$\times$80 μm, leading to an occupancy of $\approx 2-3\%$ per bunch crossing.

3. In the outermost region ($r > 55$ cm) of the inner tracker, the particle flux has dropped sufficiently to allow use of larger-pitch silicon microstrips with a maximum cell size of 25 cm$\times$180 μm, whilst keeping the occupancy to $\approx 1\%$.

Close to the interaction vertex, in the barrel region, are three layers of hybrid pixel detectors at a radii of 4.4, 7.3, and 10.2 cm. The size of

the pixels is 100×150 μm^2. In the barrel part, the silicon microstrip detectors are placed at r between 20 and 110 cm. The forward region has 2 pixel and 9 microstrip layers in each of the 2 endcaps. The barrel part is separated into an *Inner* and an *Outer* one. In order to avoid excessively shallow track crossing angles, the Inner Barrel is shorter than the Outer Barrel, and there are an additional 3 Inner Disks in the transition region between the barrel and endcap parts, on each side of the Inner Barrel. The total area of the pixel detector is ≈ 1 m^2, whilst that of the silicon strip detectors is 200 m^2, providing coverage up to $|\eta| < 2.4$. The inner tracker comprises 66 million pixels and 9.6 million silicon strips.

2.3.3.1 *Pixel Tracker*

The pixel detector consists of 3 barrel layers with 2 endcap disks on each side of them (Fig. **??**). The 3 barrel layers are located at average radii of 4.4 cm, 7.3 cm and 10.2 cm, and have a length of 53 cm. The 2 end disks, extending from 6 to 15 cm in radius, are placed on each side at $|z| = 34.5$ cm and 46.5 cm. In order to achieve the optimal vertex position resolution, a design with an almost square pixel shape of 100×150 μm^2 in both the (r,ϕ) and the z coordinates has been adopted. The barrel comprises 768 pixel modules arranged into half-ladders of 4 identical modules each. The endcap disks are assembled in a turbine-like geometry and comprise 672 pixel.

This design allows to obtain at least three 3D measurement points per track in the $|\eta| < 2.4$ region for tracks originating from the central interaction point. The total number of cells is about 66 millions, organized in about 16000 modules of 52 columns and 80 rows. The total active area is close to 1 m^2.

The pixels resolution is improved thanks to the charge sharing due to the Lorentz drift and the non-zero incident angle with respect to the module surface:

- as far as the barrel is concerned, the resolution along r is improved thanks to a Lorentz angle of about 32^o (cluster size ~ 2), while the the cluster size along the z-coordinate is 1-7 depending on the incident angle;
- for the forward pixels, a turbine geometry of 20^o was chosen to improve the resolution in r thanks to the Lorentz effect and in rϕ thanks to the non-zero incident angle (average cluster size 2).

2.3.3.2 *Strip Tracker*

The barrel tracker region is divided into 2 parts: a TIB (Tracker Inner Barrel) and a TOB (Tracker Outer Barrel). The TIB is made of 4 layers and covers up to $|z| < 65$ cm, using silicon sensors with a thickness

of 320 μm and a strip pitch which varies from 80 to 120 μm. The first 2 layers are made with "stereo" modules in order to provide a measurement in both $r-\phi$ and r-z coordinates. A stereo angle of 100 mrad has been chosen. This leads to a single-point resolution of between 23-34 μm in the $r-\phi$ direction and 230 μm in z.

The TOB comprises 6 layers with a half-length of $|z| < 110$ cm. As the radiation levels are smaller in this region, thicker silicon sensors (500 μm) can be used to maintain a good S/N ratio for longer strip length and wider pitch. The strip pitch varies from 120 to 180 μm. Also for the TOB the first 2 layers provide a "stereo" measurement in both coordinates. The stereo angle is again 100 mrad and the single-point resolution varies from 35-52 μm in the $r-\phi$ direction and 530 μm in z.

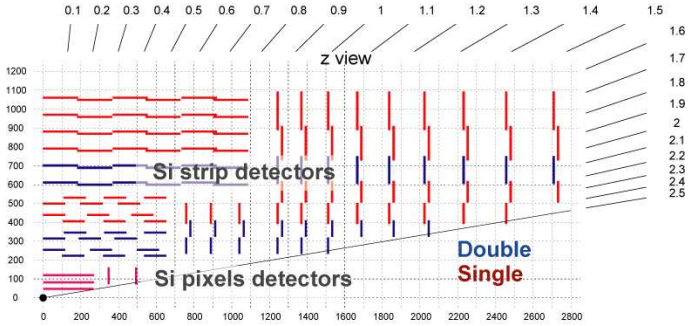

Figure 15: The tracker layout. One quarter in the z view.

The endcaps are divided into the TEC (Tracker End Cap) and TID (Tracker Inner Disks). Each TEC comprises 9 disks that extend into the region 120 cm$< |z| <$ 280 cm, and each TID comprises 3 small disks that fill the gap between the TIB and the TEC. The TEC and TID modules are arranged in rings, centred on the beam line, and have strips that point towards the beam line, therefore having a variable pitch. The first 2 rings of the TID and the innermost 2 rings and the fifth ring of the TEC have "stereo" modules. The thickness of the sensors is 320 μm for the TID and the 3 innermost rings of the TEC and 500 μm for the rest of the TEC. The entire silicon strip detector consists of almost 15400 modules, mounted on carbon-fibre structures and housed inside a temperature controlled outer support tube. The operating temperature is around -20^{o}C.

The CMS tracker, therefore, provides a full coverage for $|\eta| < 2.4$ with more than 10 high-resolution measurement points among which at least 5 provide a 3-dimensional position measurement.

Main drawback for the all-silicon CMS tracker is the large amount of material due to detector modules, support structure, cooling plant, cables and electronic devices. The total material budget in terms of radiation length is estimated to raise up to 1.8 for $\eta \sim 1.5$, corresponding to about 0.5 interaction lengths (Fig. **??**).

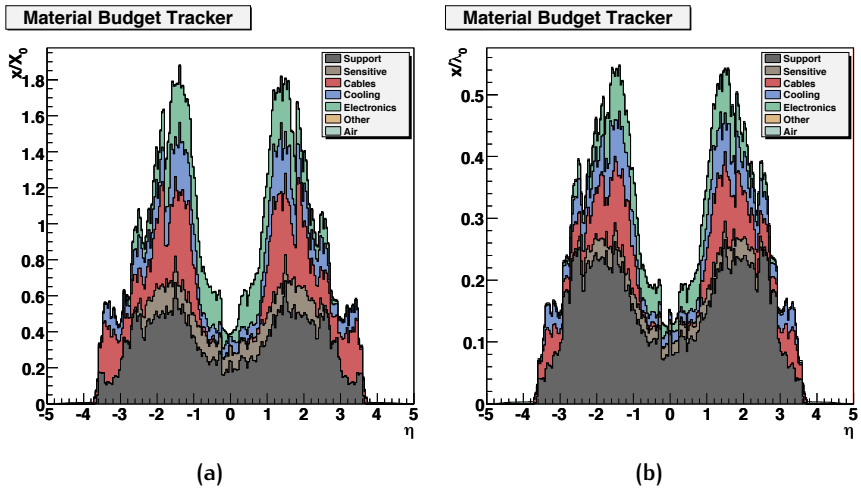

Figure 16: Material budget as a function of η expressed in terms of radiation length X_0 16a and in terms of interaction length λ_0 16b. The peak around $|\eta| = 1.5$ corresponds to the cables and services of the tracker.

The excellent performances of the tracking system are critical for the physics objects reconstruction though the the particle flow (PF) algorithm [46, 49, 50, 51], in particular taus, jets and $\not{E}_T$.

2.3.4 Electromagnetic Calorimeter

The electromagnetic calorimeter (ECAL) measures the energy of the electrons and photons. The design of the CMS ECAL [55] was driven by the requirements imposed by the search of the Higgs boson in the channel $H \to \gamma\gamma$, where a peak in the di-photon invariant mass placed at the Higgs mass, has to be distinguished from a continuous background. A good resolution and a fine granularity are therefore fundamental: both of them improve the invariant mass resolution on the di-photon system by improving respectively the energy and angle measurement of the two γs. The fine granularity also allows to separately reconstruct in different cells the two γ originated from a π^0 decay, thus improving the π_0/γ separation.

The ECAL is hermetic and homogeneous calorimeter, comprising 61 200 lead tungstate ($PbWO_4$) scintillating crystals mounted in the central barrel part, closed by 7324 crystals in each of the two endcaps. Crystals have short radiation ($X_0 = 0.89$ cm) and Molière (2.2 cm) lengths, are fast (80% of the light is emitted within 25 ns) and radiation hard (up to 10 Mrad). However, the relatively low light yield (30γ /MeV) requires use of photodetectors with intrinsic gain that can operate in a magnetic field.

	NaI(Tl)	$PbWO_4$
Density [g/cm^3]	3.67	8.28
Radiation length [cm]	2.59	0.89
Interaction length [cm]	41.4	22.4
Molière radius [cm]	4.80	2.19
Light decay time [ns]	230	5 (39%) 15 (60%) 100 (1%)
Relative light output	100	1.3

Table 3: Comparison between NaI and $PbWO_4$ crystals. The lead glass is better than the sodium iodide in every aspect, except for the light output. For this reason, in ECal, crystals are coupled to photodiodes. It is worth pointing out that the short radiation length allows ECal to be compact and that the quick response (80% of light emitted within 25 ns) is comparable with LHC bunch crossing, 25 ns.

Silicon avalanche photodiodes (APDs) are used as photodetectors in the barrel, since they can operate in magnetic field, and vacuum phototriodes (VPTs) in the endcaps. In addition, the sensitivity of both the crystals and the APD response to temperature changes requires a temperature stability. In order to preserve the ECAL energy resolution performances, a water cooling system guarantees a long term stability at the 0.1° C. The use of $PbWO_4$ crystals has thus allowed the design of a compact calorimeter inside the solenoid that is fast, has fine granularity, and is radiation resistant.

The barrel section (EB) has an inner radius of 129 cm. It is structured as 36 identical "supermodules", each containing 1700 crystals, covering half the barrel length and 20° angle in ϕ. The pseudorapidity coverage is of $0 < |\eta| < 1.479$. A supermodule is composed of four modules, each formed by submodules with five pairs of crystals. The barrel crystals have a front face cross-section of $\sim 22 \times 22$ mm^2 and have a length of 230 mm, corresponding to 25.8 X_0. In order to avoid that particles escape through the dead regions between the crystals, their axes are oriented with a 3° tilt with respect to the pointing geometry.

The endcaps (EE) are located at a distance of 314 cm from the vertex and cover a pseudorapidity range of $1.479 < |\eta| < 3.0$, ensuring precision measurements up to $\eta = 2.5$; they are structured as "Dees" consisting of semi-circular aluminium plates from which are cantilevered structural units of 5×5 crystals, known as "supercrystals". The endcap crystals, like the barrel crystals, off-point from the nominal vertex position, but are arranged in an xy grid. They are all identical and have a front face cross section of 28.6×28.6 mm^2 and a length of 220 mm ($24.7X_0$).

A preshower device, a $3X_0$ lead radiator coupled to a silicon strip detector, is placed in front of the crystal calorimeter covering most of the endcap pseudorapidity range, its main function is to provide π_0/γ separation The active elements of this device are two planes of silicon strip detectors, with a pitch of 1.9 mm, which lie behind disks of lead absorber at depths of 2 X_0 and 3 X_0.

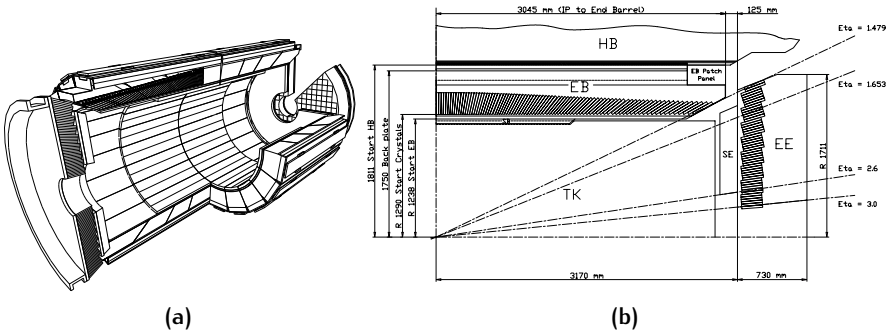

(a) (b)

Figure 17: In fig. 17a a 3-D view of the electromagnetic calorimeter. In fig. 17b longitudinal section of the electromagnetic calorimeter (one quadrant) fig. .

The energy resolution of ECal is parametrised as:

$$\left(\frac{\sigma}{E}\right)^2 = \left(\frac{a}{\sqrt{E}}\right)^2 + \left(\frac{\sigma_n}{E}\right)^2 + c^2 \tag{30}$$

where a is the stochastic term, σ_n the noise, and c the constant term (fig. 18).

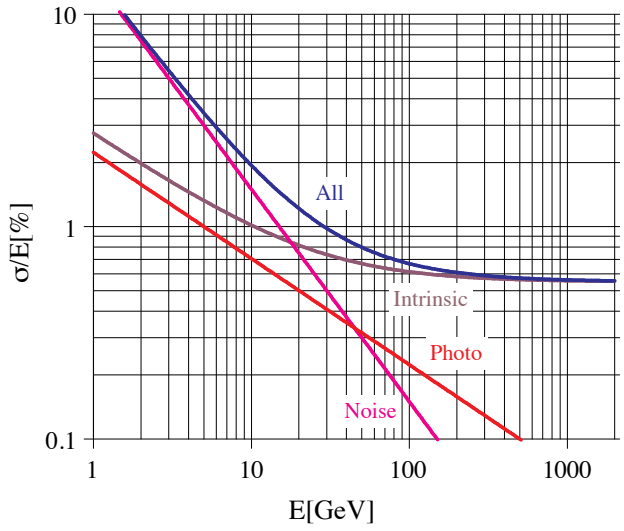

Figure 18: Different contributions to the energy resolution of the $PbWO_4$ calorimeter.

The constant term must be kept down to ~ 0.6% in order to profit from the excellent stochastic term of $PbWO_4$ in the energy range rel-

evant for the Higgs search. To achieve this goal, in situ calibration/-monitoring using isolated high p_T electrons is performed using the $Z \to ee$.

2.3.5 Hadron Calorimeter

The goal of the hadron calorimeter (HCal) is to measure jet and missing transverse energy. It is a sampling calorimeter, made up of brass absorbers staggered by plastic scintillators arranged in tiles.

The HCal is located inside the magnet coil and surrounds the ECal system. An important requirement of HCal is to minimize the non-Gaussian tails in the energy resolution and to provide good containment and hermeticity for the $\not{E}_T$ measurement. Hence, the HCal design maximizes material inside the magnet coil in terms of interaction lengths. This is complemented by an additional layer of scintillators (hadron outer detector HO) lining the outside of the coil.

Brass has been chosen as absorber material as it has a reasonably short interaction length, 6.42 cm, is easy to machine and is non-magnetic. The innermost and the outermost absorber layers are made of stainless steel for structural reason. The active medium consist of 17 layers of plastic scintillator tiles read out with embedded wavelength-shifting (WLS) fibres. The WLS fibres are spliced to high attenuation-length clear fibres outside the scintillator that carry the light to the readout system. The photodetection readout is based on multi-channel hybrid photodiodes (HPDs). The absorber structure is assembled by bolting together precisely machined and overlapping brass plates so as to leave space to insert the scintillator plates, which have a thickness of 3.7 mm.

Resolution is poorer with respect to ECal, due to the intrinsic complexity of hadronic interaction, and can be parametrized as:

$$\frac{\sigma_E}{E} = \frac{65\%}{\sqrt{E}} \oplus 5\% \tag{31}$$

The **Hadron Outer**(HO) detector contains scintillators with a thickness of 10 mm, which line the outside of the outer vacuum tank of the coil and cover the region $-1.26 < |\eta| \langle 1.26$. The tiles are grouped in 30 sectors, matching the Φ segmentation of the DT chambers. They sample the energy from penetrating hadron showers leaking through the rear of the calorimeters and so serve as a "tail-catcher" after the magnet coil. They increase the effective thickness of the hadron calorimetry to over 10 interaction lengths, thus reducing the tails in the energy resolution function. The HO also improves the $\not{E}_T$ resolution of the calorimeter.

The **Hadron Forward**, made of steel/quartz fibres, covers pseudorapidities between 3.0 and 5.0. The design leads to narrow and short hadronic showers in order to sample the neutral component. The

front face is located at 11.2 m from the interaction point and the depth of the absorber is 1.65 m. The signal originates from Cerenkov light emitted in the quartz fibres, which is then channeled by the fibres to photomultipliers. The absorber structure is created by machining 1 mm square grooves into steel plates, which are then diffusion welded. The diameter of the quartz fibres is 0.6 mm and they are placed 5 mm apart in a square grid. The quartz fibres, which run parallel to the beam line, have two different lengths (namely 1.43 m and 1.65 m) which are inserted into grooves, creating two effective longitudinal samplings.

2.3.6 Muon system

In CMS, the muon detectors are placed beyond the calorimeters and the solenoid. The muon system [57] consists of four active stations interleaved by the iron absorber layers which constitute the return yoke for the magnetic field. The muon system has three functions: muon identification, momentum measurement, and triggering. Good muon momentum resolution and trigger capability are enabled by the high field solenoidal magnet and its flux-return yoke. The latter also serves as a hadron absorber for the identification of muons.

Three different typologies of detectors are employed: drift tubes (DT) in the barrel region, cathode strip chambers (CSC) in the endcaps and, in addition to DT and CSC, resistive plate chambers (RPC) in both regions.

2.3.6.1 *Drift Tubes*

In the barrel region, where the neutron-induced background is small, the muon rate is low, and the magnetic field is uniform and mostly contained in the steel yoke, drift chambers with standard rectangular drift cells are used. The barrel drift tube (DT) chambers cover the pseudorapidity region $|\eta| < 1.2$ and are organized into 4 stations interspersed among the layers of the flux return plates. The first 3 stations each contain 8 chambers, in 2 groups of 4, which measure the muon coordinate in the $r - \phi$ bending plane, and 4 chambers which provide a measurement in the z direction, along the beam line. The fourth station does not contain the z-measuring planes.

2.3.6.2 *Cathode Strip Chambers*

In the two endcap regions of CMS, where the muon rates and background levels are high and the magnetic field is large and non-uniform, the muon system uses cathode strip chambers (CSC). With their fast response time, fine segmentation, and radiation resistance, the CSCs identify muons between $|\eta|$ values of 0.9 and 2.4. There are 4 stations of CSCs in each endcap, with chambers positioned perpendicular to

the beam line and interspersed between the flux return plates. The cathode strips of each chamber run radially outward and provide a precision measurement in the $r-\phi$ bending plane. The anode wires run approximately perpendicular to the strips and are also read out in order to provide measurements of r and the beam-crossing time of a muon. Each 6-layer CSC provides robust pattern recognition for rejection of non-muon backgrounds and efficient matching of hits to those in other stations and to the CMS inner tracker. A crucial characteristic of the DT and CSC subsystems is that they can each trigger on the p_T of muons with good efficiency and high background rejection. A complementary, dedicated trigger system consisting of resistive plate chambers (RPC) was added in both the barrel and endcap regions.

2.3.6.3 *Resistive Plate Chambers*

The RPCs provide a fast, independent, and highly-segmented trigger with a sharp p_T threshold over a large portion of the rapidity range ($|\eta| < 1.6$) of the muon system. The RPCs are double-gap chambers, operated in avalanche mode to ensure good operation at high rates. They produce a fast response, with good time resolution but coarser position resolution than the DTs or CSCs. They also help to resolve ambiguities in attempting to make tracks from multiple hits in a chamber.

2.3.7 Trigger

At the design luminosity of 10^{34} $cm^{-2}s^{-1}$, each bunch crossing results in an average of about 20 inelastic $p-p$ events producing approximately 1 MB of raw data and the expected event rate is about 10^9 Hz. These figures are many order of magnitude larger than the achievable storage capability of $O(10^2)$ Hz at data rates of $O(10^2)$ MB/s.

Indeed, most of the events are soft interactions that generate particles with low p_T, scarcely interesting for high energy physics, thus the triggering system must have a large reduction factor and maintain, at the same, time high efficiency on the potential interesting events, reducing the rate down to 100 Hz, which is the maximum sustainable rate for storing events.

The CMS trigger consists of two physical levels: a Level-1, hardware–based trigger and a software–based High Level Trigger (HLT) [2] .

2 Possibly an intermediate software–based trigger level, referred to as Level-2, can be inserted between the Level-1 and the HLT steps, for a given number of trigger paths, such as the di-tau triggers.

2.3.7.1 *The Level-1 trigger*

The Level 1 trigger [58] (L1) is a fully hardware (electronics) system that reduces the rate of selected events down to 50 (100) kHz for the low (high) luminosity running. The full data are stored in pipelines of processing elements, while waiting for the trigger decision. The L1 decision has to be taken in 3.2 ms. If the L1 accepts the event, the data are processed by the High Level Trigger.

To deal with the 25 ns bunch crossing rate, the L1 trigger has to take a decision in a time too short to read data from the whole detector, therefore it employs calorimetric and muon data only, since the tracker algorithms are too sophisticated for this purpose.

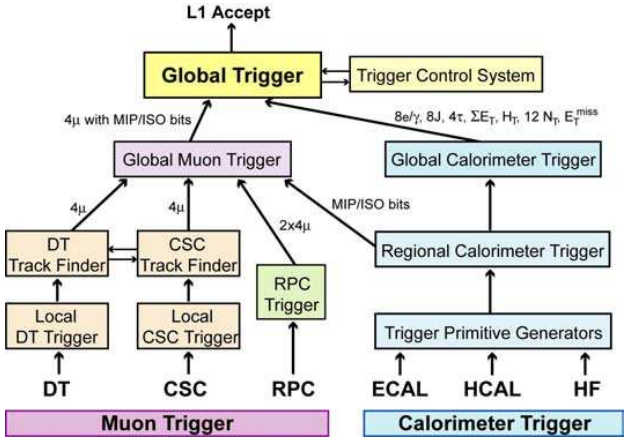

Figure 19: Architecture of the Level-1 Trigger

The Level-1 trigger is organized into a Calorimeter Trigger and a Muon Trigger whose information is transferred to the Global Trigger which takes the decision. The Calorimeter Trigger is based on trigger towers, arrays of 5 crystals in ECAL, which match the granularity of the HCAL towers. The trigger towers are grouped in calorimetric region of 4×4 trigger towers. The Calorimeter Trigger identifies, from the calorimetric region information, the best four candidates of each of the following classes: electrons and photons, central jets, forward jets and b-jets identified from the profile of the deposited energy. The information of these objects is passed to the Global Trigger, together with the measured $\not{E}_T$. The Muon trigger is performed separately for each muon detector. The information is then merged and the best four muon candidates are transferred to the Global Trigger. The Global Trigger takes the accept/reject decision exploiting both the characteristic of the single objects and of combination of them.

2.3.7.2 *The High Level Trigger*

The High Level Trigger [59] reduces the output rate down to 100 Hz. The idea of the HLT trigger software is the regional reconstruction

on demand, that is only those objects in the useful regions are reconstructed and the uninteresting events are rejected as soon as possible. This leads to the development of three "virtual trigger" levels: at the first level only the full information of the muon system and of the calorimeters is used, in the second level the information of the tracker pixels is added and in the third and final level the full event information is available.

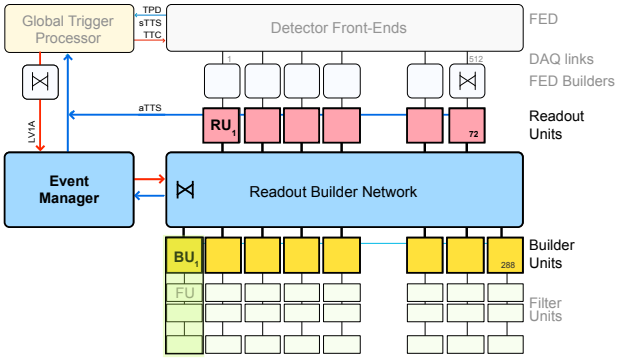

Figure 20: Architecture of the HLT Trigger

3 SEARCH FOR A SM HIGGS BOSON DECAYING INTO A PAIR OF τ LEPTONS

3.1 INTRODUCTION AND MOTIVATIONS

3.1.1 Analysis motivations

The measurement of the couplings of the Higgs boson at 125 GeV is of fundamental to assess its nature. Whilst the discovery of this particle in the ZZ, WW and $\gamma\gamma$ channels [41, 3] demonstrated the direct coupling of the Higgs to bosons, those channels can test the fermion coupling only indirectly thought loops at both production (gluon-gluon fusion) and decay (in the $\gamma\gamma$ channel) ends.

The Higgs to fermions coupling can be proved directly in the fermionic Higgs decay channels. The Yukawa coupling governs the SM Higgs interaction with the fermions and is proportional to the mass of the fermion, therefore the decay modes into heavier fermions are favoured. Being the top quark mass above the kinematic threshold for the 125 GeVHiggs decay, the dominant fermionic decay mode (branching ratio 58%) is into a pair of b–quarks (Fig. 21). However, this channel presents outstanding experimental difficulties, most notably, the overwhelming contamination from QCD multijet processes.

The relatively clean signature and the sizeable 6.3% branching ratio (Fig. 21), which is at least two order of magnitude larger than for the other leptons, make the di-tau channel the most promising to probe the Higgs to fermions coupling.

3.1.2 Analysis strategy

The search for a SM Higgs decaying into a pair of tau leptons encompasses several sub-channels and categories in order to increase the analysis sensitivity.

At the LHC the dominant contribution to the production of Higgs bosons in the SM is gluon-gluon fusion as shown in Fig. 22 (left). The gluon-fusion process suffers from the large SM Drell-Yan background with a di-τ in the final state : $Z/\gamma^{\star} \to \tau\tau$. However, a signature for gluon-fusion can be searched for by selecting boosted (high p_T) di-τ events. The initial state gluons in the Higgs production increase the likelihood of an initial state parton compared to the dominate Drell-Yan background, which is mostly produced through quark–quark an-

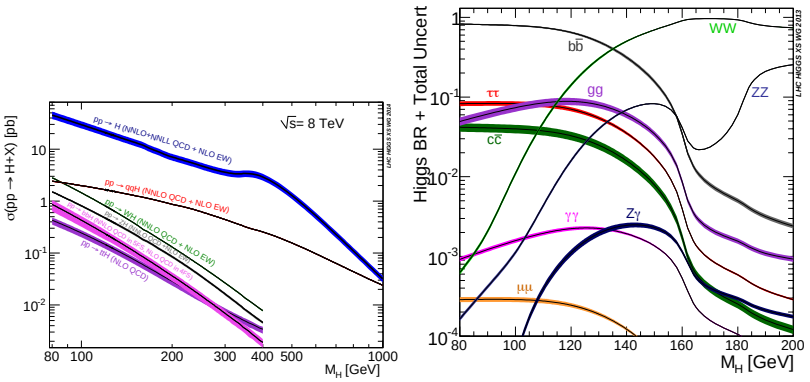

Figure 21: Higgs production cross sections for proton-proton collisions at $\sqrt{s} = 8$TeV are shown in the leftmost plot. The dominant production mechanism takes place from the fusion of two gluons through a quark loop ($pp \rightarrow H$ in the plot); the second most important mode is the Vector Boson Fusion (referred to as VBF, $pp \rightarrow qqH$ in the plot) followed by the W/Z associated production (referred to as VH, $pp \rightarrow WH$, $pp \rightarrow ZH$ in the plot). Each of these different production processes gives rise to a peculiar experimental signature: ggH can be accompanied by extra jet(s), VBF is characterised by the presence of two back-to-back quark jets in the forward region and VH can be singled out by and extra lepton(s) indicating the presence of a vector boson. The SM Higgs branching ratios as a function of m_H are shown in the rightmost plot.

nihilation. This initial state parton manifests itself as a collimated jet in the reconstructed event leading to the higher transverse momentum of the di-τ system. The high p_T of the recoiling jet in addition allows for a more precise measurement of the $\not{E}_T$ and additionally a favourable kinematic setting, which improves the reconstructed mass resolution of the di-τ system.

The VBF process (Fig. 22 middle) allows for a more efficient suppression of the Drell-Yan background due to the presence of two light quark jets with a distinctive signature of a large rapidity gap, leading to a large di-jet invariant mass. The VH production process (Fig. 22 right) offers a clean environment due to the requirement of one or two muons or electrons in addition to the $\tau\tau$ decay products. Despite the lower production crossections and the irredicible ZZ and WZ SM backgrounds, these channels combined offer a sensitivity of 2.3 x the SM signal for $M_H = 125GeV$. Furthermore these channels place important upper limits on the V-H couplings.

For these three Higgs boson production processes all the six di-τ final states (Tab. 4 and 5) are considered: $\mu\tau_h$, $e\tau_h$, $\tau_h\tau_h$, $e\mu$, $\mu\mu$, and ee.

The events are then classified in mutually exclusive categories according to the number of reconstructed jets in the final state and,

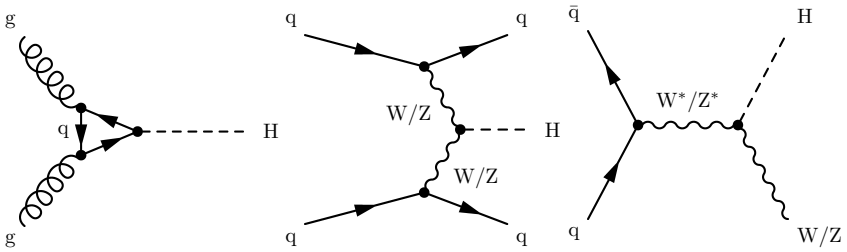

Figure 22: Main contributions to the production of the Higgs boson in the SM: (left) gluon-gluon fusion, (middle) vector boson fusion and (right) Higgs production in association with a vector boson Z or W.

Decay Mode	Resonance	Mass [MeV]	Brancing Ratio
$\tau \to e\nu_e\nu_\tau$			17.8%
$\tau \to \mu\nu_\mu\nu_\tau$			17.4%
$\tau \to h\nu_\tau$			11.6%
$\tau \to h\pi^0\nu_\tau$	ρ	770	26.0%
$\tau \to h\pi^0\pi^0\nu_\tau$	a1	1220	10.8%
$\tau \to h^\pm h^\pm h^\mp \nu_\tau$	a1	1220	9.8%
$\tau \to h^\pm h^\pm h^\mp \pi^0 \nu_\tau$			4.8%
Other hadronic modes			1.7%

Table 4: The τ is the heaviest lepton, $m_\tau = 1.78$ MeV, and it is unstable, with lifetime equal to $2.91 \cdot 10^{-13}$ s. It decays into either light leptons, electrons or muons or into hadrons h (pions, in more than 95% of the events, else kaons). The leptonic decaying taus are effectively identified as isolated electrons or muons in the final state. The hadronically decaying tau reconstruction algorithm, described in Sec. 3.3.4, can distinguish the decay modes by counting the charged and neutral hadrons lying together within a cone. In all cases, at least one neutrino is produced, which manifests as a contribution to the missing transverse energy $\not{E}_T$.

in particular, the contribution of the VBF production process is enhanced by requiring a large rapidity gap between the two jets with the highest transverse momentum. Moreover, the transverse momentum of the τ (for $\mu\tau_h$, $e\tau_h$ channels) or the μ (for $e\mu$ channel) and the transverse momentum of the Higgs candidate are used to further split the events in order to profit from signal-enhanced regions of the phase space.

For the Higgs boson production in association with a vector boson, Fig. 22 rightmost graph, the presence of one or two additional light leptons, ascribable to a W or a Z boson respectively, is required.

Channel	Fraction of di-τ events
$\mu\tau_h$	22.6%
$e\tau_h$	23.0%
$\tau_h\tau_h$	42.0%
$e\mu$	6.2%
$\mu\mu$	3.0%
ee	3.2%

Table 5: Di-tau final states and their relative abundances.

Four channels are considered for the WH process: $\mu + \mu\tau_h$, $\mu + e\tau_h/e + \mu\tau_h$, $\mu + \tau_h\tau_h$ and $e + \tau_h\tau_h$, whilst eight channels are aimed at identifying the ZH process: $\ell\ell + \mu\tau_h$, $\ell\ell + e\tau_h$, $\ell\ell + \tau_h\tau_h$, $\ell\ell + e\mu$, where $\ell\ell$ can be either $\mu\mu$ or ee.

The present work is focused on the study of the $\tau_h\tau_h$ final state. The definition of the physics objects is presented in Sec. 3.3, the selections, the category layout and the estimates of the backgrounds are detailed in Sec. 3.4, 3.5 and 3.6 respectively. The statistical interpretation and the results are then shown in Sec. 3.7.2 and Sec. 4.5.

All the six di-tau channels were included into the search for the SM Higgs decaying into a pair of taus: some parts of the analysis, such as the physics object definition and the statistical interpretation, are common for all of them. In the last section, both the $\tau_h\tau_h$ and the combined results are reported.

3.2 DATASETS AND SAMPLES

The datasets used for the analysis and 2012 data are summarized in Table 6. The total integrated luminosity of the analyzed data amounts to 19.7 fb^{-1} for which good quality runs are selected by applying the JSON file listed below:

```
Cert_190456-208686_8TeV_22Jan2013ReReco_Collisions12_JSON.txt
```

Data Sample for Event Selection 2012	**Integrated Luminosity [pb^{-1}]**
/Tau/Run2012A-22Jan2013-v1/AOD	876.2
/TauParked/Run2012B-22Jan2013-v1/AOD	4411.0
/TauParked/Run2012C-22Jan2013-v1/AOD	7054.8
/TauParked/Run2012D-22Jan2013-v1/AOD	7369.0

Table 6: Summary of the data samples used for the analysis of the data collected in 2012. The table lists all samples used for the main event selection. In the MSSM analysis, period 2012A is dropped and period 2012B is considered only for a partial integrated luminosity of 3870 pb^{-1} is considered.

The data is compared to the expectation from all applicable signal and background processes. For the signal these expectations are based on theoretical calculations by the means of Monte Carlo simulations. The simulated production processes for a SM Higgs boson are listed below:

- **ggH ($gg \to H$):** The main production process of gluon-gluon fusion.
- **qqH ($qq \to H$):** The production process via vector-boson fusion (VBF).
- **VH ($qq \to VH$) / ttH ($gg \to t\bar{t}H$):** The production in association with vector-bosons or $t\bar{t}$ quarks.

These production processes have been produced using the NLO program *Powheg* [14, 122] [121, 90, 15] interfaced to the *Pythia* event generator to account for additional QCD initial and final state radiation [129]. The inclusive yields have been normalized according to the inclusive cross section and Branching Ratios as described in [115].

For the background processes both Monte Carlo simulations and estimates from data have been used. The background processes for each individual decay channel are categorized as:

- **Drell-Yan τ-pair production ($Z \to \tau\tau$).** The kinematics of this dominant background is estimated using the $2 \to N$ LO event

generator *Madgraph* [17] (for $N \leqslant 4$) interfaced to *Pythia* to account for additional QCD initial and final state radiation. The inclusive yields have been normalized according to the cross section of inclusive Z boson production as measured in a control region of $Z \to \mu\mu$ events. A scale factor following efficiency corrections between data and Monte Carlo predictions is used to correct the overall $Z \to \tau\tau$ yield. The simulation by the *Madgraph* event generator does not include any processes that accounts for the production of Z bosons via VBF. For a better estimate of migrations between the different event categories, as they will be defined in Section 3.5, $Z \to \mu\mu$ events in data are used making use of an *embedding* algorithm. According to this algorithm the reconstructed muons are interpreted as τ leptons and the subsequent decays are added to the event from the simulation. This technique has been validated to be unbiased, within the statistical precision of the analysis, using simulated $Z \to \mu\mu$ events, to which the embedding algorithm has been applied, and comparing these events to fully simulated $Z \to \tau\tau$ events.

- **QCD multijet production**: a jet or a non-isolated lepton is misinterpreted as τ_h (also referred to as *Fakes*). The kinematics and normalization of these backgrounds is estimated from data as described in Section 3.6.2. Simulated QCD multijet events are used for the validation of the data–based background estimation methods within their uncertainties. These events have been generated using *Pythia*, taking additional QCD initial and final state radiation into account and preselecting for the presence of at least one muon or electron above given p_T thresholds at generator level.

- **W +jets production**: the W boson decays into a lepton, electron, muon or tau, plus the corresponding neutrino. The largest fraction of selected W +jets events is made up by $W \to \tau\nu$ decays, where the tau subsequently decays into hadrons. In the remaining events, either the electron or the muon is misidentified as a τ_h The second hadronic tau of the event is given by jet faking an hadronic tau. The kinematics of *W*+jets production is simulated using the *Madgraph* event generator interfaced to *Pythia* to account for additional QCD initial and final state radiation as described above.

- **Z +jets production**, where the Z boson decays into two muons or two electrons. The two selected hadronic taus can be given by the two leptons being misidentified as τ_h (mostly electron) or by one of such leptons and an additional jet faking a τ_h.

- **Inclusive $t\bar{t}$ production**. This background is simulated using the *Madgraph* event generator interfaced to *Pythia* to account for additional QCD initial and final state radiation as described above. The event yields are normalized according to the inclusive $t\bar{t}$ production cross section as measured by CMS [71]. In 2012 data, in light of the missing cross section measurement, the $t\bar{t}$ normalization is performed by measuring the observed $t\bar{t}$ yields in bins of the number of jets where at least one b-tag is applied.

- **Di-Boson production**, where the bosons decay into leptons according to the analyzed decay channel. This background is simulated using either the *Pythia* event generator or *Madgraph* interfaced with *Pythia* as described above. The event yields are normalized according to the inclusive NLO cross sections as calculated from [120, 119].

For all signal and background samples that explicitly include τ-leptons, the subsequent decay of the τ-lepton is simulated using the *Tauola* software package [134]. A summary of all simulated event samples for 2012 is given in Tab. 7. All generated events have been processed through the full simulation of the CMS detector based on the *Geant 4* package [12, 16] and the detailed simulation of the CMS trigger system. The presence of pileup is incorporated by simulating additional interactions using *Pythia* and reweighing the simulated events to match the distribution of additional interactions, observed in a minimum bias data sample. The reweighting procedure is described in [1].

3.3 OBJECT IDENTIFICATION & SELECTION

3.3.1 Event Vertex

The vertices of proton-proton interactions are reconstructed using the *Deterministic Annealing* (DA) clustering algorithm [126]. These vertices are then required to satisfy the following criteria:

- The distance in the z direction from the vertex to the nominal interaction points to the nominal interaction point must be smaller then 24 cm

- The corresponding distance in the the transverse plane must be smaller than 2 cm

- The number of degrees of freedom of the vertex fit is required to be larger than 4

Higgs Signal Processes		
Process	Dataset Name	$\sigma\times$ BR [pb] m_H =125 GeV
$gg \to H$	/GluGluToHToTauTau_M-*_8TeV-powheg-pythia6	19.27 * 0.0637
$qq \to qqH$	/VBF_HToTauTau_M-*_8TeV-powheg-pythia6	1.58 * 0.0637
$gg \to t\bar{t}/VH$	/WH_ZH_TTH_HToTauTau_M-*_8TeV-pythia6-tauola	1.12 * 0.0637
Background Processes 2012		
Process	Dataset Name	$\sigma\times$ BR [pb]
$t\bar{t} \to ll$	TTJets_FullLeptMGDecays_8TeV-madgraph-tauola	249.5 * 0.105
$t\bar{t} \to lqq$	TTJets_SemiLeptMGDecays_8TeV-madgraph-tauola	249.5 * 0.438
$t\bar{t} \to qqqq$	TTJets_HadronicMGDecays_8TeV-madgraph	249.5 * 0.457
$t \to X$ (tW)	/T_tW-channel-DR_TuneZ2star_8TeV-powheg-tauola	11.1
$\bar{t} \to X$ ($\bar{t}W$)	/Tbar_tW-channel-DR_TuneZ2star_8TeV-powheg-tauola	11.1
$Z \to ll$+jets	/DYJetsToLL_M-50_TuneZ2Star_8TeV-madgraph-tarball	3503.7
$Z \to ll$+1jet	/DY1JetsToLL_M-50_TuneZ2Star_8TeV-madgraph-tarball	561.0
$Z \to ll$+2jets	/DY2JetsToLL_M-50_TuneZ2Star_8TeV-madgraph-tarball	181.0
$Z \to ll$+3jets	/DY3JetsToLL_M-50_TuneZ2Star_8TeV-madgraph-tarball	51.1
$Z \to ll$+4jets	/DY4JetsToLL_M-50_TuneZ2Star_8TeV-madgraph-tarball	23.04
W+jets	/WJetsToLNu_TuneZ2Star_8TeV-madgraph-tarball	36257.2
W+1jet	/W1JetsToLNu_TuneZ2Star_8TeV-madgraph-tarball	6381.2
W+2jets	/W2JetsToLNu_TuneZ2Star_8TeV-madgraph-tarball	2039.8
W+3jets	/W3JetsToLNu_TuneZ2Star_8TeV-madgraph-tarball	612. 5
W+4jets	/W4JetsToLNu_TuneZ2Star_8TeV-madgraph-tarball	251.0
WW	/WWJetsTo2L2Nu_TuneZ2star_8TeV-madgraph-tauola	5.824
WZ	/WZJetsTo3LNu_TuneZ2_8TeV-madgraph-tauola	1.058
WZ	/WZJetsTo2L2Q_TuneZ2star_8TeV-madgraph-tauola	2.207
ZZ	/ZZJetsTo4L_TuneZ2star_8TeV-madgraph-tauola/	0.181
ZZ	/ZZJetsTo2L2Nu_TuneZ2star_8TeV-madgraph-tauola/	0.716
ZZ	/ZZJetsTo2L2Q_TuneZ2star_8TeV-madgraph-tauola/	2.502

Table 7: Samples of simulated events used for the analysis of the data collected in 2012. The name of the file sets is to be extended by *Summer12-DR53X-PU_S10_START53_V*/AODSIM* for each sample in 2012. The production cross sections for the SM Higgs boson are given for $m_H = 125$ GeV. The W+1jets ,W+2jets, W+3jets and the W+4jets samples are merged with the inclusive sample where the inclusive sample in order to increase the statistics. As a consequence, the equivalent luminosity (number of generated events divided the cross section) resulting MC sample is differs for events with different jet multiplicity. To cure this undesired effect and to make the sample easily usable, the events are appropriately weighed to level the corresponding luminosity across the different jet multiplicity bins. The same procedure is applied for DY+jets samples.

Out of the selected vertices, the one with the largest summed squared p_T of the tracks associated to that vertex is chosen as the event vertex corresponding to the hard scattering process. All other vertices are considered to come from additional soft scattering collisions at collision time (pile-up).

3.3.1.1 *Pile-up re-weighting*

In order to represent the pile-up as observed in data the simulated events are re-weighted as a function of the number of additional simulated iteractions as described in [1]. A minimum bias cross section of 69.4 mb (68.0 mb) is used for generating the expected pile-up distribution in 2012 (2011) data. The validity of this process is reflected in the distribution of reconstructed primary vertices, which is correlated with the number of interactions. In Fig. 23 the number of reconstructed primary vertices is shown before and after the reweighting of the (upper row) 2011 and (lower row) 2012 data in the $e\mu$-channel. This channel, at the preselection level, is the dominated by the DY$\rightarrow \tau\tau$ contribution, which is the standard candle for the $H \rightarrow \tau\tau$, therefore it well suits the purpose of this figure. Remaining discrepancies are taken into account in the systematic uncertainties, by re-weighting the simulated events within the boundaries given by the statistical precision of the data. Object reconstruction has been chosen to be minimally sensitive to pile-up. These uncertainties are therefore anticipated to be small.

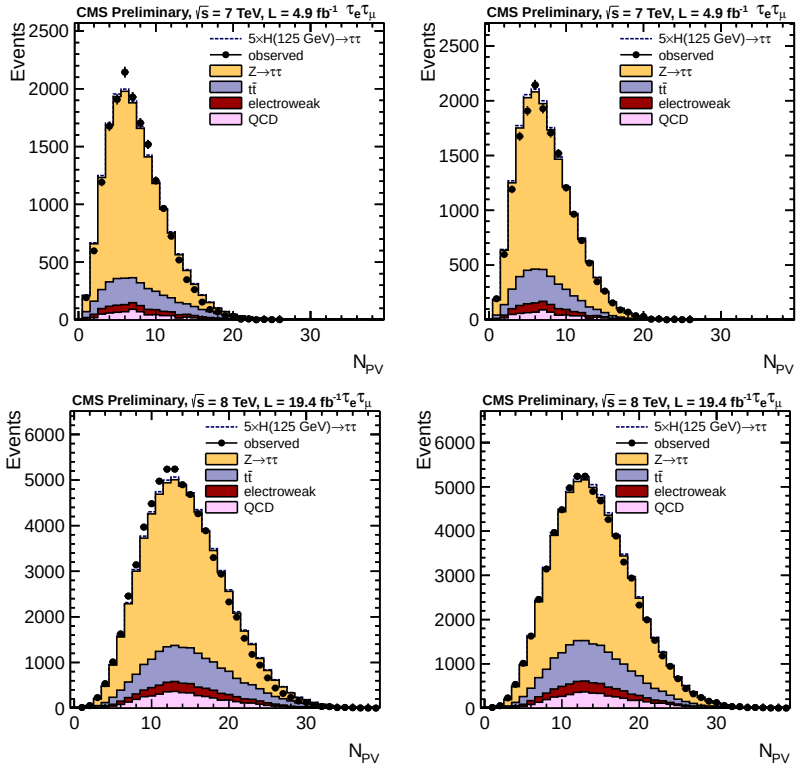

Figure 23: Expected and observed number of reconstructed primary vertices for the data collected in (upper row) 2011 and (lower row) 2012 (left) before and (right) after the pileup re-weighting as described in [1]. These distributions have been taken from the $e\mu$ decay channel.

3.3.2 Particle-Flow Reconstruction

All reconstructed energy deposits and tracks in the CMS detector are combined to form a complete and unambiguous event description with the aim to reconstruct and identify all particles produced in the hard interaction as completely as possible. This reconstruction is referred to as particle-flow. A full description of the particle-flow algorithm is given in [46]. The reconstructed particle-flow candidates are classified as muons, electrons, photons, neutral hadrons and charged hadrons. They are further on used to reconstruct and select all higher analysis objects used for this analyses as described in the following sections.

To reduce the dependency of the analysis on pile-up a further separation of all charged particle-flow candidates, which do have a track (charged hadrons, electrons and muons) is applied, depending on whether the track can be associated to the selected primary vertex or not. A track is considered as associated to the selected primary vertex if the distance between the vertex and the track along the z direction of the experiment is smaller than 0.1 cm. Any charged particle-flow candidate, whose tracks cannot be associated to the selected primary vertex, is considered to come from pile-up (generally referred to *pfPileup* in the analysis). Those charged particle-flow candidates, whose tracks can successfully be associated to the selected primary vertex, are considered as coming from the hard interaction (generally referred to as *pfNoPileup* in the analysis). Such a distinction is not possible for neutral particle-flow candidates.

3.3.3 Muons and Electrons

Muon Identification:

Muons are required to be reconstructed by the *Tracker* or the *Global* muon reconstruction algorithm [67] and to be identified as muons by the particle-flow algorithm as described in [39, 46]. The particle-flow algorithm identifies muons by separating them into three object categories:

- **Isolated:** For this category strong isolation requirements are imposed on the reconstructed muon candidate. These isolation requirements are imposed on the muon candidate already on the particle flow reconstruction level. They are independent of the isolation requirements that are applied later in the analysis. Other quality requirements on the reconstructed muon candidate are kept very loose.

- **PF-Tight:** For this category no isolation requirement is imposed. The candidate is required to have a minimum number of hits on the track, to be compatible with a track segment in the muon

detector and to have an associated energy deposition in the calorimeter, which is compatible with a muon as defined by a template based on the full detector simulation of the CMS detector.

- **PF-Loose:** For reconstructed muon candidates, which do not fall into any of the above categories and whose associated energy depositions in the calorimeter are not compatible with a charged hadron hypothesis, the requirement on the number of hits on the track is relaxed and the compatibility with a track segment in the muon detector is replaced by a looser matching requirement of the track to hits in the stations of the muon detector.

After the *Isolated* muons have been identified, the remaining candidates are categorized according to the *PF-Tight* and *PF-Loose* object category. The latter two categories have been optimized to identify muons in jets. A reconstructed muon candidate is considered as particle-flow identified if it falls into any of these categories. A number of additional *Tight Muon* requirements, as recommended by the *Muon POG* are applied for the muons selected in the $e\mu$ and $\mu\tau_h$ channels:

- Impact parameter constrains between the muon track and the selected primary vertex require $d_z < 0.1$ cm and $d_0 < 0.02$ cm in the $e\mu$ channel and $d_z < 0.2$ cm and $d_0 < 0.045$ cm in the $\mu\tau_h$ channel.
- The χ^2/ndof of the global track fit must be smaller than 10
- At least one segment in the muon detector is included in the global track fit
- Muon track segments in at least two stations of the muon detector
- At least one hit in the pixel detector and hits in more than 5 layers of the inner track detector

Electron Identification:

Electrons are required to pass an identification variable based on a multivariate *Boosted Decision Tree* (BDT) discriminator based on track quality, cluster shape and kinematic quantities. The BDT has been trained on data selecting genuine electron candidates from well reconstructed $Z \to ee$ events and mis-identified (fake) electron candidates from Z+jets events, from which the electrons, which have been used to reconstruct the Z boson candidate, have been excluded. For the training, all electrons (without any trigger requirement) have been taken into account. The training has been performed in two bins of

p_T and three bins of η of the electron as shown in Tab. 8. The BDT has the following 19 variables as input:

- The normalized χ^2 of the common track fit, the number of valid hits in the track fit, the normalized χ^2 of the *GSFTrack* fit.
- The distance in η ($\Delta\eta_{SC}(Track_{vtx})$) and ϕ ($\Delta\phi_{SC}(Track_{vtx})$) between the reconstructed super cluster in the calorimeter and the track evaluated at the primary vertex position, the distance in η between the super cluster seed and the track evaluated at the calorimeter surface.
- The cluster shape variables $\sigma_{i\eta,i\eta}$ and $\sigma_{i\phi,i\phi}$, where $i\eta$ ($i\phi$) indicate the integer label of the electromagnetic calorimeter cell in η (ϕ), the cluster shape variable $f_e = 1 - e1X5/e5X5$, where $e1X5$ ($e5X5$) indicate the energy deposition in an array of 1×5 (5×5) cells in the vicinity of the super cluster seed, the cluster shape variable $R9 = e3x3/E_{SC}$, where $e3x3$ and E_{SC} indicate the energy in an array of 3×3 cells in the vicinity of the super cluster seed and the raw energy of the reconstructed super cluster.
- The ratio of the hadronic energy over electromagnetic energy of the super cluster (H/E), the ratio of the super cluster energy over the momentum of the associated track evaluated at the selected primary vertex (E/P), the variable $1/E_e - 1/p_e$, where E_e and p_e indicate the reconstructed energy and momentum of the electron candidate, the ratio of the electron cluster over the momentum of the associated track and the ratio of the seed cluster over the associated track, where each time the track momentum has been evaluated at the surface of the calorimeter.
- The ratio of the energy that has been reconstructed in the preshower detector over the raw energy of the reconstructed super cluster. The momentum and η of the reconstructed electron candidate.

An electron is considered as well identified if the BDT discriminator falls above the thresholds shown in Tab. 8. In addition the electron candidate is required to have a distance from the selected primary vertex of $d_z < 0.1$ cm along the z direction of the experiment and $d_0 < 0.02(0.045)$ cm in the plane perpendicular to z in the $e\mu$ ($\mu\tau_h$ / $e\tau_h$) decay channel. Further there should be no missing hits in the inner layers of the pixel detector, no hits before the selected primary vertex and a vertex fit probability of more than $P > 10^{-6}$ to minimize the probability that the electron candidate originates from a photon conversion.

Muon and Electron Isolation:

	BDT Discriminator Value (>)		
	$\lvert\eta\rvert < 0.8$	$0.8 \leqslant \lvert\eta\rvert < 1.479$	$1.479 \leqslant \lvert\eta\rvert$
$p_T \leqslant 20$	0.925	0.915	0.965
$p_T > 20\,\text{GeV}$	0.905 (0.925)	0.955 (0.975)	0.975 (0.985)

Table 8: Thresholds for the BDT discriminator to identify electrons. For an identified electron the discriminator value has to fall above the indicated threshold. The values correspond to the *LooseIF* working points as recommended by the *EgammPOG*. For electrons with $p_T > 20$ GeV, the values in braces correspond to the *TightID* working points (as recommended by the *EgammaPOG*) which has been chosen in the $e\tau_h$-channel.

To reduce the contamination from muons (electrons) originating from b- or c-quark decays within jets or decays in flight, the selected muons (electrons) are required to be isolated. The isolation is based on particle-flow candidates, of which all photon and neutral hadron candidates and all charged particle-flow candidates (including charged hadrons, electrons and muons), which have been associated to the selected primary vertex (*pfNoPileup*) are considered. For the muon isolation, the photon and neutral hadron candidates are required to have a transverse energy of $E_T > 0.5$ GeV.

The transverse energy (momentum) of the particle-flow candidates reconstructed within a cone of radius $\Delta R < 0.4$, centered on the trajectory of the lepton candidate, are considered in the computation of the isolation. The lepton itself is excluded by comparing the shared track when comparing to charged particle-flow candidates and by implying a veto cone depending on the lepton to be isolated and on the type of particle-flow candidates in consideration as detailed in Tab. 9.

The so called $\Delta\beta$ corrections are applied in order to account for the energy of additional neutral particles due to the presence of pile-up: the transverse momentum of all charged hadron candidates within the isolation cone, which do not fulfill the primary vertex restriction (*pfPileup*) as described above, is summed. For these charged hadron candidates no threshold on the momentum is required for the electron isolation, while for the muon isolation they are required to have a $p_T > 0.5\,\text{GeV}$ and to lie outside an inner veto cone of $\Delta R_{inner} > 0.01$. This transverse momentum sum is corrected by a factor of 2:1 to account for the amount of neutral energy with respect to the amount of charged energy in the isolation cone. A relative combined isolation variable is then defined as:

$$I_{rel} = \frac{\sum p_T(\text{charged}) + \max\left(\sum E_T(\text{neutral}) + \sum E_T(\text{photon}) - \Delta\beta, 0\right)}{p_T(\mu \text{ or } e)} \tag{32}$$

where $p_T(\mathrm{charged})$ corresponds of the p_T of all charged particle candidates, $p_T(\mathrm{photon})$ and $p_T(\mathrm{neutral})$ correspond to the transverse energy of the photon and neutral hadron candidates and $\Delta\beta$ corresponds to the energy estimate of neutral particles due to pile-up. In the $\mu\tau_h$- ($e\tau_h$-)channel $I_{rel} < 0.1$ is required, both for muons and electrons. In the $e\mu$-channel the restriction on I_{rel} is chosen to be $I_{rel} < 0.15$ in the barrel ($|\eta| < 1.479$) and $I_{rel} < 0.1$ in the endcap ($|\eta| \geqslant 1.479$) region of the detector, for electrons and correspondingly in the central ($|\eta| < 1.5$) and encap ($|\eta| \geqslant 1.5$) region of the detector for muons. In the $\mu\mu$-channel $I_{rel} < 0.1(0.15)$ is required for the leading (sub-leading) muon. This isolation has been endorsed by the *EgammaPOG* for the analysis of 2011 and 2012 data.

	Charged Part. Cand.	Phot. Cand.	Neutr. Had. Cand.	Charged Part. (PU)
μ	0.0001	0.01	0.01	0.01
e (Barrel)	0.01	0.08	none	none
e (Endcap)	0.015	0.08	none	none

Table 9: Summary of the veto cones used for the calculation of I_{rel} as defined in Eq. 32 for all decay channels. The cones are defined in the η-ϕ space.

Electron and Muon veto definitions

Looser identifcation and isolation criteria are used to define veto objects, with requirements varying channel by channel to reduce specific backgrounds:

- In the $\mu\tau_h$ channel events are vetoed if they contain an opposite-sign muon pair in which each muon has $p_T > 15$ GeV, $|\eta| < 2.4$, $d_z < 0.2$ cm, $d_0 < 0.045$ cm, is reconstructed by the tracker and global algorithms and has $I_{rel} < 0.3$. The muons must also have a minimum separation of $\Delta R > 0.15$. This veto is optimised to reject the background of $Z \to \mu\mu$ events.

- In the $e\tau_h$ channel events are vetoed if they contain an opposite-sign electron pair in which each electron has $p_T > 15$ GeV, $|\eta| < 2.5$, $d_z < 0.2$ cm, $d_0 < 0.045$ cm, passes the *veto* cut-based criteria defined by the *EGamma POG*, and has $I_{rel} < 0.3$. The electrons must also have a minimum separation of $\Delta R > 0.15$. This veto is optimised to reject the background of $Z \to ee$ events.

- In the $e\tau_h$, $\mu\tau_h$, $e\mu$ and $\tau_h\tau_h$ channels events are vetoed if they contain any muon (or any additional muon in $\mu\tau_h$ and $e\mu$) with $p_T > 10$ GeV, $|\eta| < 2.4$, $d_z < 0.2$ cm, $d_0 < 0.045$ cm, which satisfies the *Tight* indentification detailed above and has $I_{rel} < 0.3$.

- In the same channels events are vetoed if they contain any electron (or any additional electron in $e\tau_h$ and $e\mu$) with $p_T > 10\,\text{GeV}$, $|\eta| < 2.5$, $d_z < 0.2$ cm, $d_0 < 0.045$ cm, which fulfils the *loose* MVA-based indentification detailed above and has $I_{rel} < 0.3$.

3.3.4 Tau leptons: hadronic decays

Hadronic decays of tau leptons are reconstructed by the "Hadrons plus Strips" (HPS) identification algorithm [35]. The constituents of the jets are analyzed in order to identify individual tau lepton hadronic decay modes. The presence of extra particles within the jet, not compatible with the reconstructed decay mode of the tau, is used as criterion to discriminate hadronic tau decays from quark and gluon jets. A set of additional discriminators is provided by the algorithm to separate hadronic tau decays from electrons and muons.

3.3.4.1 *Decay mode reconstruction*

The decay mode reconstruction algorithm is seeded by jets reconstructed by the anti–k_T algorithm [28] with distance parameter $R = 0.5$, using particles reconstructed by the PF algorithm [46] as input.

In order to reconstruct the tau decay mode the algorithm needs to build candidate π^0 mesons. Photons originating from $\pi^0 \to \gamma\gamma$ have a high probability to convert within the volume of the tracking detector. The algorithm takes this into account by clustering photons reconstructed by the PF algorithm into $\eta - \phi$ "strips". The size of the strips, 0.20×0.05, is enlarged in η–direction to acount for the bending of e^+e^- pairs produced by photon conversions in the 4 Tesla magnetic field of the tracking detector. Strips containing one or more photons and passing a cut $p_T > 2.5\,\text{GeV}$ on the sum of photon transverse momenta are kept as π^0 candidates for further processing.

Once the collection of π^0 candidates has been built, the tau reconstruction proceeds with building τ_h candidates by pairing the strips with charged hadrons reconstructed by the PF algorithm. A combinatorial approach is again employed for the tau candidate building. A tau candidate hypothesis is built for every combination of jet constituents (π^0 candidates plus charged hadrons) which has a multiplicity consistent with a hadronic tau decay:

- **Three Hadrons**: A combination of three charged hadrons of $p_T > 0.5$ GeVwithin a mass window of $0.8 < M < 1.5$ GeV. The tracks are required to be compatible with originating from the same event vertex within $\Delta z < 2$ mm and to sum to unit charge. This decay mode corresponds to the signature expected for $\tau^\pm \to a_1^\pm \nu_\tau \to \pi^\pm\pi^\mp\pi^\pm\nu_\tau$ decays ($\mathcal{BR} \sim 10\%$).

- **Hadron plus two Strips:** A combination of one charged hadron with two strips within a mass window of $0.4 < M < 1.2 \cdot \sqrt{\frac{p_T}{200\,\text{GeV}}}$ GeV in case the τ_h candidate has $200 < p_T < 800$ GeV. For τ_h candidates of $p_T < 200\,\text{GeV}$ (> 800 GeV) the upper limit of the mass window is set to 1.2 GeV (2.0 GeV). This decay mode corresponds to the signature expected for $\tau^\pm \to a_1^\pm \nu_\tau \to \pi^\pm\pi^0\pi^0\nu_\tau$ decays ($\mathcal{BR} \sim 9\%$).

- **Hadron plus one Strip:** A combination of one charged hadron with one strips within a mass window of $0.4 < M < 1.3 \cdot \sqrt{\frac{p_T}{200\,\text{GeV}}}$ GeV in case the τ_h candidate has $200 < p_T < 800$ GeV. For τ_h candidates of $p_T < 200\,\text{GeV}$ (> 800 GeV) the upper limit of the mass window is set to 1.3 GeV (2.1 GeV). This decay mode corresponds to the signature expected for $\tau^\pm \to \rho^\pm \nu_\tau \to \pi^\pm\pi^0\nu_\tau$ decays ($\mathcal{BR} \sim 25\%$).

- **Single hadron:** A single charged hadron reconstructed by the PF algorithm without any strips. This decay mode corresponds to the signature expected for $\tau^\pm \to \pi^\pm \nu_\tau$ decays ($\mathcal{BR} \sim 11\%$).

All charged hadrons and strips considered in the tau decay mode reconstruction are required to be within a narrow cone around the jet axis, of size:

$$\Delta R = \begin{cases} 0.05 & \text{if } p_T > 56\,\text{GeV} \\ \frac{2.8}{p_T} & \text{if } 28 < p_T < 56\,\text{GeV} \\ 0.10 & \text{if } p_T < 28\,\text{GeV} \end{cases}$$

In case of ambiguities, the tau candidate with the smallest amount of jet energy not accounted for by the reconstructed tau decay mode is given preference.

3.3.4.2 *Tau isolation discriminators*

The isolation of τ_h candidates is computed by summing the transverse momenta of charged particles of $p_T > 0.5\,\text{GeV}$ plus photons of $E_T > 0.5\,\text{GeV}$ reconstructed by the PF algorithm within a cone of size $\Delta R = 0.5$ centered on the τ_h direction. Charged hadrons considered in the isolation p_T sum are required to satisfy $\Delta z < 2$ mm with respect to the τ_h production vertex, taken to be the vertex which gives the highest probability of association to the "leading" (highest p_T) track of the τ_h. Charged hadrons used to built the τ_h candidate are excluded from the isolation p_T sum, as are photons used to built any of the strips. The contribution of pile–up to the τ_h isolation is accounted for by applying $\Delta\beta$ corrections:

$$I_{\tau_h} = \sum p_T^{charged}(\Delta z < 2\text{ mm}) + \max\left(p_T^\gamma - \Delta\beta, 0\right).$$

The $\Delta\beta$ corrections are computed by summing the transverse momenta of charged particles that have a longitudinal impact parameters $\Delta z > 2$ mm with respect to the τ_h production vertex and are within a cone of size $\Delta R = 0.8$ around the τ_h direction. The sum is scaled by a factor 0.4576, chosen to make the τ_h identification efficiency insensitive to pile–up:

$$\Delta\beta = 0.4576 \cdot \sum p_T^{charged}(\Delta z > 2 \text{ mm}).$$

Loose, Medium and Tight working–points of the *HPS combined isolation 3–hit discriminator* are defined by requiring the isolation p_T sum not to exceed 0.8, 1.0 and 2.0 GeV respectively. The performances in terms of efficiency and jet rejection are shown in Fig. 24

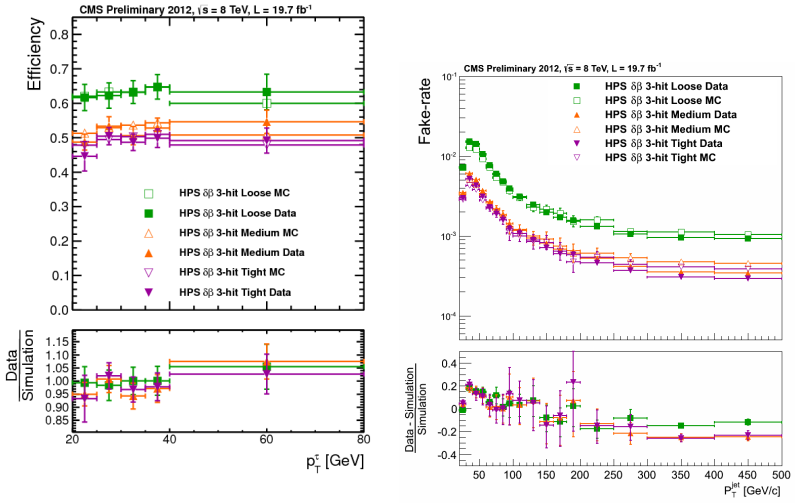

Figure 24: Efficiency for selecting real tau (left) and for selecting a gluon- or quark-initiated jet as a fake tau (right). Data/MC correction factors compatible with 1 within the statistical uncertainty in each bin.

3.3.4.3 *Trigger efficiency in the $\tau_h\tau_h$ channel*

The τ_h trigger efficiency is determined by selecting Drell-Yan $Z \to \mu\tau_h$ events in the single muon dataset. The identified τ_h is then used to compute the trigger efficiency. Since the τ_h trigger is not present in the actual trigger menu, a dedicated re-reconstruction of the single muon dataset is performed so as to measure the trigger. The resulting trigger is then fit with a three parameter turn-on curve, consisting of an effective turn-on point, a plateau efficiency and a turn-on slope. The trigger efficiencies as a function of tau p_T are given in figure 25 for data and simulation. For the kinematic selection of $\tau_h > 45$ GeV an increase in the efficiency is present and flattens

at roughly 80% at 50 GeV. Variation on the tau energy scale and plateau uncertainy yields an overall 4.5% per-leg uncertainty on the tau trigger.

3.3.5 Decay mode and energy scale corrections

The energy measurement of the τ_h is controlled in data and calibrated by means of a maximum-likelihood fit performed on the distribution of the mass or the visible decay products of the taus, using a Drell-Yan to tau tau enhanced sample, in the $\mu\tau_h$ final state Fig. 26. The mass distribution of the Drell-Yan component is coherently scaled by a shift parameter, that, together with the normalisation are adjusted by the fit. This is done separately per each decay mode and provides a full set of normalisation scale factors and energy scale calibrations for each tau decay mode Tab. 10. These corrections are applied to the real taus in all the MC samples before running the full analysis.

Decay Mode	Scale Factor	Energy Scale shift
1 prong	0.88	-
1 prong + n π^0	1.0	+1.2%
3 prongs	1.0	+1.2%

Table 10: Normalisation and energy scale corrections relative to the hadronic decaying taus.

3.3.5.1 *anti–mu discriminator*

The discriminator against muons (Version 2) is based on vetoing taus in case hits in the muon system are found near the τ_h direction. Loose, medium and tight working–points are provided, corresponding to different τ_h identification efficiencies and $\mu \to \tau_h$ fake–rates:

- **anti–mu Loose**: τ_h candidates fail this discriminator in case a track segment in the muon system is found within a cone of size $\Delta R = 0.5$ centered on the τ_h direction.
- **anti–mu Medium**: τ_h candidates fail this discriminator in case they fail the anti–mu Loose discriminator or signals above noise threshold are present in CSC, DT or RPC modules located in the two outermost muon stations within a cone of size $\Delta R = 0.5$ around the τ_h direction.
- **anti–mu Tight**: τ_h candidates fail this discriminator in case they fail the anti–mu Medium discriminator or the energy in ECAL plus HCAL associated by the PF algorithm to the leading track of the τ_h candidate falls short of 20% times the track momentum.

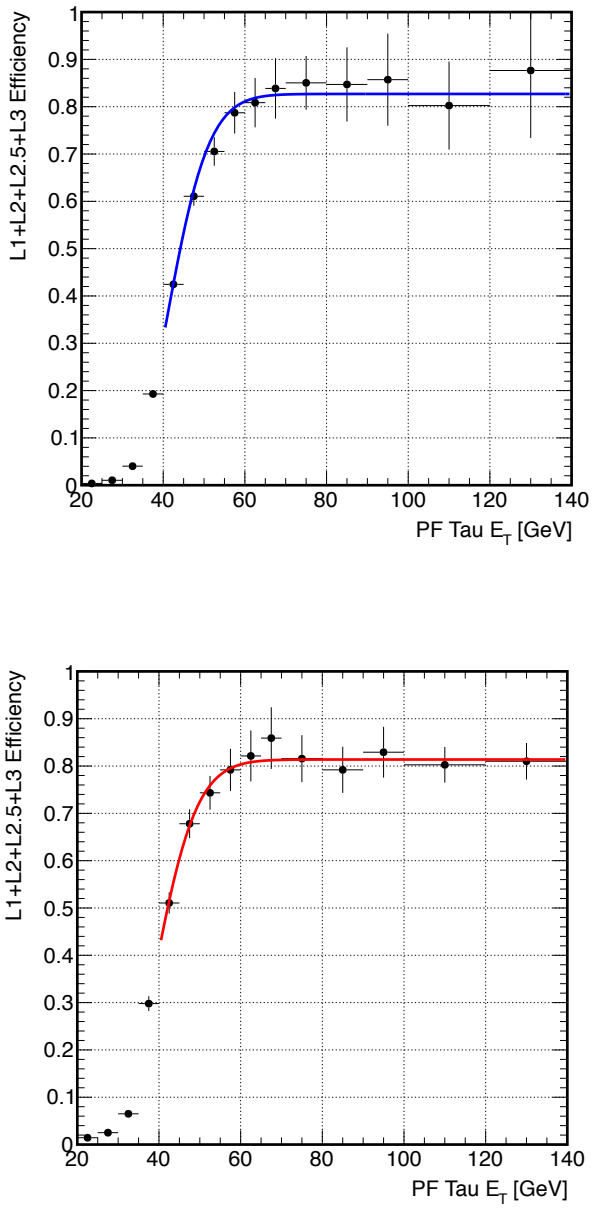

Figure 25: Trigger turn-on curves for an individual leg of the τ_h trigger, for data (left) and simulation (right). Data over MC scale factors are derived from the ratio of the two curves, as a function of tau p_T.

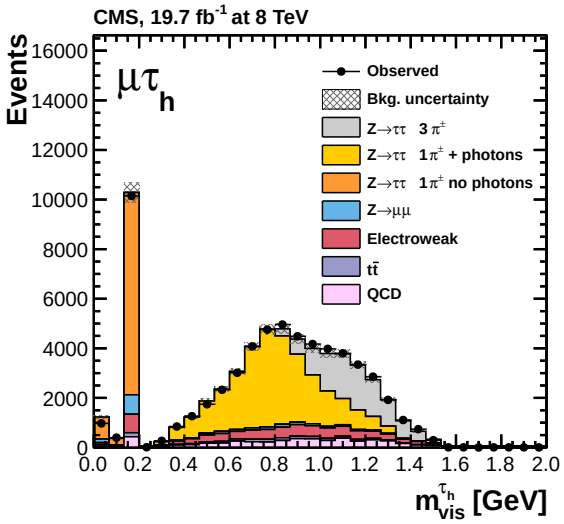

Figure 26: Observed and predicted distributions for the visible τ_h mass, $m_{vis}^{\tau_h}$, in the $\mu\tau_h$ channel after the baseline selection described in Sec. 3.4. The yields predicted for the $Z \to \tau\tau$, $Z \to \mu\mu$, electroweak, $t\bar{t}$, and QCD multijet background contributions correspond to the result of the final fit presented in Sec. 4.5. The $Z \to \tau\tau$ contribution is then split according to the decay mode reconstructed by the hadron-plus-strips algorithm as shown in the legend. The mass distribution of the $\tau_h$built from one charged hadron and photons peaks near the mass of the intermediate ρ resonance; the mass distribution of the $\tau_h$built from three charged hadrons peaks around the mass of the intermediate $a_1(1260)$ resonance. The $\tau_h$built from one charged hadron and no photons are reconstructed with the $\pi^\pm$ mass, assigned to all charged hadrons by the PF algorithm, and constitute the main contribution to the third bin of this histogram. The first two bins correspond to $\tau^\pm$ leptons decaying into $e^\pm\nu\nu$ and $\mu^\pm\nu\nu$, respectively, and for which the electron or muon is misidentified as a τ_h. The electroweak background contribution is dominated by $W+$jets production. a jet is misidentified as a τ_h. The "bkg. uncertainty" band represents the combined statistical and systematic uncertainty in the background yield in each bin. The expected contribution from the SM Higgs signal is negligible.

3.3.6 Jets & b-tagging

For the classification of events according to different production mechanisms of the Higgs boson, jets are used. These jets are clustered from all particle-flow candidates using the anti-k_t algorithm with an opening parameter of $R = 0.5$ [128, 48].

To distinguish those jets that belong to the hard interaction from jets that originate from pile-up a multivariate *Boosted Decision Tree* (BDT) discriminator is used. This discriminator is based on the com-

patibility of the contained tracks with the selected primary vertex, jet shape variables, and the multiplicity of both neutral and charged components within the jet. Currently, three different discriminators have been defined in the *JetMET POG* [66]. For this analysis only the MVA full jet id is considered, where, with this discriminator, jets are required to pass the *Loose* working point of the discriminator corresponding to 95% efficiency for 20 GeV jets within the tracker volume and 85% efficiency for 20 GeV jets outside the tracker volume. For this analysis a cut of 30 GeV is applied to all jets, giving an efficiency of >99 percent within the tracker volume and roughly 95 percent outside the tracker volume.

All selected jets are corrected up to the absolute energy scale applying standard jet energy scale corrections (including *L2L3Residual* corrections on data) as described in [63, 64, 62, 65]. To take any residual effects of pile-up into account *L1Fastjet* corrections are applied. To exclude the selected electrons, muons and τ_h-leptons from the jet collection, the jets are required to be separated by a distance larger than $\Delta R(\mathrm{jet}-\mathrm{lepton}) > 0.5$ from the selected leptons. Jets with a corrected transverse momentum of $p_T > 30\,\mathrm{GeV}$ within a pseudorapidity range of $|\eta| < 4.7$ are taken into account. An uncertainty on the jet energy scale depending on the p_T and the η of the jet according to the prescription of the *JetMET POG* is taken into account and propagated into the measurement. Jet energy corrections and uncertainties of the jet energy scale correspond to the recommendation of the *JetMET POG* for the complete 2011 and 2012 datasets. The difference between these jet energy corrections and the most up to date recommendations of the *JetMET POG* has been verified to be small. Residual differences have been absorbed into an additional jet energy scale uncertainty. Due to the use of dedicated corrections on the $\not\!\!E_T$ in the event the uncertainties on the jet energy scale are not correlated with the uncertainties on $\not\!\!E_T$.

The selection or veto of events containing b-tagged jets forms part of the category definitions in the SM and MSSM analyses. This is particularly important in the latter, where a b-tag category targets the production of a Higgs boson in association with b-jets. A number of b-jet properties such as the long lifetime of the b hadrons and the production of leptons in decay are exploited by CMS through several b-tagging algorithms [40]. In this analysis the Combined Secondary Vertex algorithm, which utilises track impact-parameter and secondary vertex information, is used exclusively. A jet is considered b-tagged if it has $p_T > 20\mathrm{GeV}$, $|\eta| < 2.4$ and discriminator output greater than 0.679. This is the medium working point of the discriminator as defined by the B-Tag POG.

The efficiency for the tagging of b-jets and the mis-tagging rate for light jets has been measured in both data and simulation. Differences are corrected for in the simulation through the application of

efficiency and mis-tag scale factors provided by the B-Tag POG. The values of these factors and a description of the methods used to determine them can be found in Ref. [68] and [74] for 2011 and 2012 data respectively. The simulation is corrected by randomly re- classifying a subset of tagged jets as un-tagged, or vice versa as necessary. The promotion or demotion probabilities for each jet are determined from the p_T, η and jet-flavour dependent scale factors (SF) and simulation tagging efficiencies (Eff) where

$$\begin{aligned} P(\text{demote}) &= 1 - SF && \text{when } SF < 1 \\ P(\text{promote}) &= \frac{(SF-1)}{\frac{SF}{Eff}-1} && \text{when } SF > 1 \end{aligned}$$

Uncertainties on the scale factors are accounted for by varying them by the $\pm 1\sigma$ values and propagating this through the promotion and demotion procedure and ultimately into the change in category yield for each background. The b-tagging and mis-tagging uncertainties are treated as independent nuisance parameters in the maximum-likelihood fit.

3.3.7 Missing Transverse Energy

To discriminate Higgs events from background events consisting of W bosons in association with jets, $t\bar{t}$-quark pairs and to reconstruct the full Higgs and Z boson mass particle flow missing transverse energy ($\not{E}_T$) is utilized. The performance of particle flow in the data for 2011 differs with respect to the Monte Carlo by 2 percent in the response and roughly 10 percent in the resolutions. In 2012 data, the $\not{E}_T$ response is reduced by roughly 5 percent.

To account for this shortcoming, a correction is derived from an independent $Z \to \mu\mu$ event sample, which does not contain any process with inherent missing transverse energy. A parametrization of the longitudinal and transverse component of the p_T response and the resolution of the boson recoil in the Z boson is determined as a function of the p_T and the jet multiplicity of the reconstructed Z boson. This parametrization can be obtained after the *Inclusive Selection* and for each of the event categories defined in Section 3.4 to prevent biases due to differences in the event topology. The parametrization of the recoil as determined from data is applied to all simulated events as a function of the p_T of the generated Higgs, W or Z boson. Finally the $\not{E}_T$ of each simulated event is determined as the transverse energy of the vectorial sum over the visible decay products of the generated particle(s) in consideration and the recoil as parametrized from data.

This method is equivalent to deriving an additional Gaussian smearing that accounts for the degradation of the $\not{E}_T$ resolution due to event pile-up. It is generally referred to as *Recoil Correction*. More details

can be found in [91]. No correction is necessary for the estimation of the most prominent backgrounds from $Z \to \tau\tau$ events and from QCD multijet events, which are taken from data as described in Section **??**.

3.3.7.1 *MVA Missing Transverse Energy*

To discriminate events containing Higgs bosons from background events with W bosons in association with jets or $t\bar{t}$-quark pairs 5 different missing transverse energy ($\not{E}_T$) variables are calculated from particle-flow candidates using the information of the jet identification as described above. These $\not{E}_T$ variables are:

- The negative vectorial sum of all particle-flow candidates (particle-flow $\not{E}_T$).
- The negative vectorial sum of all tracks that have been associated to the selected primary vertex.
- The negative vectorial sum of all tracks that have been associated to the selected primary vertex and all neutral particle-flow candidates within those jets that have passed the jet identification as described above.
- The negative vectorial sum of all tracks that have not been associated to the selected primary vertex and all neutral particle-flow candidates within those jets that have failed the jet identification as described above.
- The negative vectorial sum of all tracks that have been associated to the selected primary vertex and all neutral particle-flow candidates (also those that have not been clustered into jets) plus the *positive* vectorial sum of all neutral particle-flow candidates within jets that have failed the jet identification as described above.

For each $\not{E}_T$ variable the vectorial recoil is calculated as defined by:

$$\vec{u} = \not{E}_T \cdot \hat{\phi} - \sum_i \vec{p_T}^{lep} \tag{33}$$

where $\hat{\phi}$ corresponds to the direction of $\not{E}_T$ in the transverse plane of the detector and $\vec{p_T}^{lep}$ to the p_T vector of the leptons originating from the hard interaction (which in this case corresponds to the respective e, μ or τ_h lepton pair).

The corresponding magnitude, the azimuthal angle ϕ of the recoil and the scalar $\sum E_T$ of each respective $\not{E}_T$ variable, the momentum vectors of the two leading jets and the number of primary vertices are added to a multivariate *Boosted Decision Tree* (BDT) regression, which

is used to compute a correction to both the angle and magnitude of the particle flow recoil to match the true recoil.

The training on the recoil has been performed on a sample of simulated $Z \to \mu\mu$ events and validated on a selection of $Z \to \mu\mu$ events in data. The final corrected recoil is added to the vector sum of the leptons following equation 33 to give the corrected $\not{E}_T$ used further on in the analysis. This correction minimizes the effects of pile-up and reduces the overall $\not{E}_T$ resolution at high pile-up by 40%.

In Fig. 27 the resolution of the hadronic recoil response and resolution for both particle flow and MVA $\not{E}_T$ are shown. The agreement between data and Monte Carlo is slightly improved for the MVA $\not{E}_T$. In both missing energies a drop in the response is present, this is a result mainly of missing transparency corrections in part of the dataset, which cause a gradual drop in the response over time. The agreement between data and simulation in the response and resolution is much improved after corrections and well spanned by the presented systematic uncertainties.

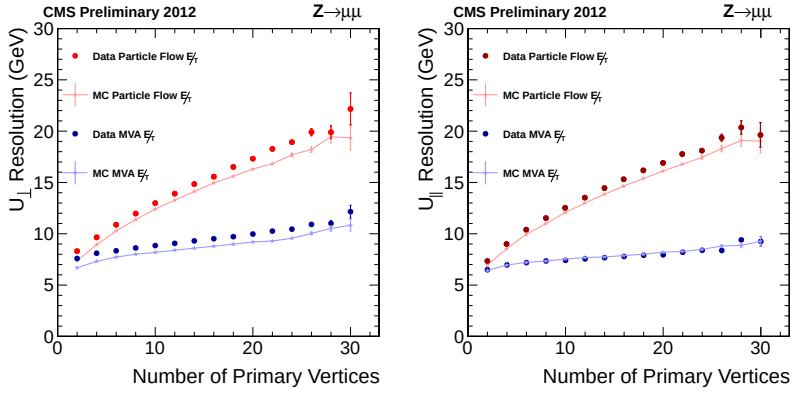

Figure 27: Resolution of the reconstructed recoil in Z boson events projected (left) on the axis perpendicular to the boson direction and (right) on the axis longitudinal to the boson direction.

3.3.8 SV-Fit algotrithm

The visible mass, m_{vis}, of the di-τ system could be used to separate the $H \to \tau\tau$ signal events from the $Z \to \tau\tau$ events, which constitute an important irreducible background. However, the neutrinos from the τ-lepton decay can take away a large amount of energy, thereby limiting the separation power of the m_{vis} variable. In $Z \to \tau\tau$ events and in $H \to \tau\tau$ events where the Higgs boson is produced through gluon-gluon fusion, VBF, or in association with a Z boson, the τ-lepton decay is the only source of neutrinos. Therefore, the $\vec{\not{E}}_T$ can be combined with the momenta of the signal leptons (either taus or light leptons depending on the channel) to build a more precise estimator

of the mass of the parent boson. The collinear approximation [84] provides such an estimator but leads to an unphysical solution for about 20% of the events, in particular when the $\not{E}_T$ and the parent boson p_T are small. The SVFIT algorithm described below estimates the τ-pair invariant mass $m_{\tau\tau}$ with improved resolution and gives a valid solution for more than 99.9% of the events.

Six parameters are needed to specify a hadronic τ-lepton decay: the polar and azimuthal angles of the visible decay product system in the τ-lepton rest frame, the three boost parameters from the τ-lepton rest frame to the laboratory frame, and the invariant mass m_{vis} of the visible decay products. In the case of a leptonic τ decay two neutrinos are produced and the invariant mass of the two-neutrino system is the seventh parameter. The unknown parameters are constrained by four observables that are the components of the four-momentum of the system formed by the visible decay products of the τ lepton, measured in the laboratory frame. For each hadronic (leptonic) τ-lepton decay, 2 (3) parameters are thus left unconstrained. These parameters are chosen to be:

- x, the fraction of the τ-lepton energy in the laboratory frame carried by the visible decay products;
- ϕ, the azimuthal angle of the τ-lepton direction in the laboratory frame;
- $m_{\nu\nu}$, the invariant mass of the two-neutrino system in leptonic τ decays; for hadronic τ-lepton decays, we take $m_{\nu\nu} \equiv 0$ in the fit described below.

The two components $\not{E}_x$ and $\not{E}_y$ of the $\vec{\not{E}}_T$ provide two further constraints, albeit each with an experimental resolution of 10–15 GeV [34, 52].

The fact that the reconstruction of the τ-pair decay kinematics is underconstrained by the measured observables is addressed by a maximum likelihood fit method. The mass, $m_{\tau\tau}$, is reconstructed by combining the measured observables $\not{E}_x$ and $\not{E}_y$ with a likelihood model that includes terms for the τ-lepton decay kinematics and the $\not{E}_T$ resolution. The likelihood function $f(\vec{z}, \vec{y}, \vec{a_1}, \vec{a_2})$ of the parameters $\vec{z} = (\not{E}_x, \not{E}_y)$ in an event is constructed, given that the unknown parameters specifying the kinematics of the two τ-lepton decays have values $\vec{a_1} = (x_1, \phi_1, m_{\nu\nu,1})$ and $\vec{a_2} = (x_2, \phi_2, m_{\nu\nu,2})$, and that the four-momenta of the visible decay products have the measured values $\vec{y} = (p_1^{\text{vis}}, p_2^{\text{vis}})$. This likelihood model is used to compute the probability

$$P(m_{\tau\tau}^i) = \int \delta\left(m_{\tau\tau}^i - m_{\tau\tau}(\vec{y}, \vec{a_1}, \vec{a_2})\right) f(\vec{z}, \vec{y}, \vec{a_1}, \vec{a_2})\, d\vec{a_1}\, d\vec{a_2}, \quad (34)$$

as a function of the mass hypothesis $m^i_{\tau\tau}$. The best estimate, $\hat{m}_{\tau\tau}$, for $m_{\tau\tau}$ is taken to be the value of $m^i_{\tau\tau}$ that maximizes $P(m^i_{\tau\tau})$.

The likelihood $f(\vec{z}, \vec{y}, \vec{a_1}, \vec{a_2})$ is the product of three likelihood functions: the first two functions model the decay parameters $\vec{a_1}$ and $\vec{a_2}$ of the two τ leptons, and the last one quantifies the compatibility of a τ-pair decay hypothesis with the measured $\vec{E}_T$. The likelihood functions modelling the τ-lepton decay kinematics are different for leptonic and hadronic τ-lepton decays. Matrix elements for unpolarized τ-lepton decays from ref. [27] are used to model the differential distributions in the leptonic decays,

$$\mathcal{L}_{\tau,l} = \frac{d\Gamma}{dx\, dm_{\nu\nu}\, d\phi} \propto \frac{m_{\nu\nu}}{4m_\tau^2}[(m_\tau^2 + 2m_{\nu\nu}^2)(m_\tau^2 - m_{\nu\nu}^2)], \tag{35}$$

within the physically allowed region $0 \leqslant x \leqslant 1$ and $0 \leqslant m_{\nu\nu} \leqslant m_\tau\sqrt{1-x}$. For hadronic τ-lepton decays, a model based on the two-body phase space [25] is used, treating all the visible decay products of the τ lepton as a single system,

$$\mathcal{L}_{\tau,h} = \frac{d\Gamma}{dx\, d\phi} \propto \frac{1}{1 - m_{vis}^2/m_\tau^2}, \tag{36}$$

within the physically allowed region $m_{vis}^2/m_\tau^2 \leqslant x \leqslant 1$. It has been verified that the two-body phase space model is adequate for representing hadronic τ-lepton decays by comparing distributions generated by a parameterized MC simulation based on the two-body phase space model with results from the detailed simulation implemented in TAUOLA. The likelihood functions for hadronic (leptonic) τ-lepton decays do not depend on the parameters x, ϕ, and $m_{\nu\nu}$ (x and ϕ). The dependence on x enters via the integration boundaries. The dependence on ϕ comes from the likelihood function $\mathcal{L}_\nu$, which quantifies the compatibility of a τ-lepton decay hypothesis with the reconstructed $\vec{E}_T$ in an event, assuming the neutrinos from the τ-lepton decays to be the only source of missing transverse energy. This likelihood function is defined as

$$\mathcal{L}_\nu(E_x, E_x) = \frac{1}{2\pi\sqrt{|V|}} \exp\left[-\frac{1}{2}\begin{pmatrix} E_x - \sum p_x^\nu \\ E_x - \sum p_y^\nu \end{pmatrix}^T V^{-1} \begin{pmatrix} E_x - \sum p_x^\nu \\ E_x - \sum p_y^\nu \end{pmatrix}\right]. \tag{37}$$

In this expression, the expected $\vec{E}_T$ resolution is represented by the covariance matrix V, estimated on an event-by-event basis using a $\vec{E}_T$ significance algorithm [34]; $|V|$ is the determinant of this matrix.

The relative $m_{\tau\tau}$ resolution achieved by the SVFIT algorithm is estimated from simulation and found to be about 10% in the $\tau_h\tau_h$ decay channel, 15% in the $\ell\tau_h$ channels, and 20% in the $\ell\ell'$ channels.

The resolution varies at the level of a few percent between the different event categories defined in section **??** because in some categories events with a boosted (i.e. high-p_T) Higgs boson candidate and thus a better $\vec{\not{E}}_T$ resolution are selected. The $m_{\tau\tau}$ resolution for each channel and each category is listed in Tab. 19 of appendix **??**. Fig. **??** shows the normalized distributions of m_{vis} and $m_{\tau\tau}$ in the $\mu\tau_h$ channel after the baseline selection for simulated $Z \to \tau\tau$ events and simulated SM Higgs boson events with $m_H = 125\,\text{GeV}$. The SVFIT mass reconstruction allows for a better separation between signal and background than m_{vis} alone, yielding an improvement in the final expected significance of $\sim 40\%$.

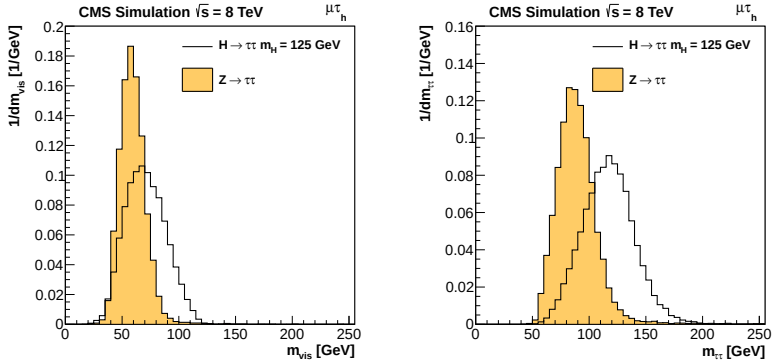

Figure 28: Normalized distributions obtained in the $\mu\tau_h$ channel after the baseline selection for (left) the invariant mass, m_{vis}, of the visible decay products of the two τ leptons, and (right) the SVFIT mass, $m_{\tau\tau}$. The distribution obtained for a simulated sample of $Z \to \tau\tau$ events (shaded histogram) is compared to the one obtained for a signal sample with a SM Higgs boson of mass $m_H = 125\,\text{GeV}$ (open histogram).

In the case of Higgs boson production in association with a W boson, the neutrino from the W-boson decay is an additional source of $\not{E}_T$. Therefore, in the these channels, the signal is extracted from the distribution of the visible mass, m_{vis}, of the $\ell\tau_h$ system.

3.4 EVENT SELECTION

All events in consideration are required to have a well reconstructed primary vertex as defined in Sec. 3.3.1. Di-τ events are selected in the fully hadronic channel requiring two isolated, opposite sign τ_h.

3.4.1 Trigger Paths

Selected events are required to pass one of the following triggers

- `HLT_DoubleMediumIsoPFTau25,30_Trk5,1_eta2p1_Jet30`
- `HLT_DoubleMediumIsoPFTau35_Trk5,1_eta2p1`

All triggers select two isolated, high p_T taus; in addition the first ones requires the presence of a further jet, with p_T larger than 30 GeV and within $\eta < 3.0$. The di-tau plus jet trigger had been available for the entire 2012 data taking and was part of the `Tau` primary dataset, whereas the di-tau trigger was deployed later, starting from 2012B period, and was included in the `TauParked` primary dataset, covering an integrated luminosity of 18.3 out of 19.7 fb^{-1} collected by CMS in 2012.

The events selected by these two triggers present a non-null overlap, but they are also complementary. In fact, thanks to lower tau p_T thresholds, the di-tau plus jet trigger can select events where at least one tau is too soft to fire the di-tau trigger and, in turn the di-tau trigger can select events where no additional jet accompanies the two hadronic taus.

In order to maximise the signal acceptance, both triggers were employed according to the following logic: at first the event is required to pass the di-tau trigger; if the event fails, then it is checked against the di-tau plus jet trigger. The event is rejected only in case none of the two triggers is fired.

For the selected events, the two offline taus (and possibly the extra jet) are required to be ΔR-matched (within a cone size equal to 0.5) to the corresponding trigger objects.

The selected MC events are corrected by means of tau p_T-depended scale-factors, meant to adjust the efficiency of the simulated trigger to the trigger efficiency as measured in data. The technique used to measure the trigger efficiency in both data and MC is described in detain in App. A.

The Drell–Yan embedded sample does not contain the HLT simulation, therefore, each event passing the offline selection is weighed by the trigger efficiency measured in data.

3.4.2 Event Selection

In the offline selection at least two τ_h leptons with $p_T > 45$ GeV and $|\eta| < 2.1$ are required. To further discard events where either a muon or an electron fakes an hadronic tau, the anti–muon and anti–electron loose woking point discriminators must be passed.

All the possible di-tau pairs are built and only the one whose taus are the most isolated is kept as Higgs candidate. The maximum isolation criterion is preferred over the more common maximum p_T sum because it does not bias the QCD, which is estimated using the method described in Sec. 3.6.2, that relies on the relaxation of the tau isolation requirements.

The characteristic trigger efficiency curve as a function of the offline tau p_T, detailed in App. A, presents a broad rising edge, referred to as *turn on*, around the nominal HLT tau p_T cut, as in Fig. 25. This effect is caused by the coarse resolution of the Level-2 tau reconstruction. The relatively high offline tau p_T threshold ensures to select events whose p_T is far from the shoulder of the turn on curve, which is difficult to properly model, and are closer to the efficiency plateau.

The selected taus are further required to have opposite charge, where for the τ_h the charge is determined from the particle-flow charged hadron candidate(s) in the one-prong (three-prong) decay channel. In addition to the previous, to remove overlap with analysis in the VH channel and to further reduce the backgrounds, the event is removed from the selection if an additional electron or muon is found according to:

- **muon**
  - $p_T > 10$ GeV
  - $|\eta| < 2.4$
  - muon loose ID (as defined in [39])
  - relative isolation < 0.3
- **electron**
  - $p_T > 10$ GeV
  - $|\eta| < 2.5$
  - electron loose ID (WP95 as defined in [47])
  - relative isolation < 0.3

The events passing this selection, referred to as *lepton selection* in the following, are still dominated by QCD multijet processes. This background is reduced by further kinematic and topological requirements.

3.4.3 Control Plots

The modeling of the observables that are relevant for the analysis is checked for the events that pass the lepton selection 3.4.2, before any further selection and categorisation is applied.

Unless mentioned otherwise, the following control plots are shown after requiring the lepton selection to be satisfied. For these figures residual global normalisation correction factors (post-fit corrections) have been applied, representing corrections to background normalisations and selection efficiencies that have been determined from the maximum likelihood fit **??** to the data which is applied prior to the limit calculation. Correction factors resulting from shape uncertainties, which do not modify the normalisation, are not applied in the plots. The *background uncertainty* hashed band includes both the statistical and residual post–fit systematic uncetainties.

The p_T and $|\eta|$ of the selected taus are shown in Fig. 29. The transverse missing energy $\not{E}_T$ and the number of reconstructed primary vertices in the event are shown in Fig. 30.

The separation in ΔR between the two signal taus and Higgs system p_T (constructed from the vectorial sum of the taus and $\not{E}_T$) are shown in Fig. 31.

The number of selected jets and the number of b-tagged jets are shown in Fig. 34. The p_T and η of the leading jet for events with at least one jet and of the sub-leading jet for events with at least two jets are shown in Fig. 32. The difference in pseudorapidity between the two leading jets, $|\Delta\eta_{jj}|$, and the invariant mass of the two leading jets are shown in Fig. 33 for events with at least two jets with $p_T > 30$ GeV. The p_T and η of the leading b-tagged jet with $p_T > 20$ GeV is shown in Fig. 35 for events where at least one jet passes the medium CSV discriminator working point 3.3.6.

3.4.4 Higgs system transverse momentum selection

In order to reduce the background contamination originating primarily from QCD multi-jet events, additional kinematic cuts targeted explicitly at removing QCD events are applied. In the SM analysis, the vast majority of QCD background originates from 3-jet events, where the jets are typically biased to more forward regions. In some instances, the selection originates from dijet events where a third jet emerges from off radiated partons that fragment into a third jet that gets identified as a τ_h. Thus, both such events which fake a hadronic tau tend to have a relatively large ΔR between the two identified τ_h.

In addition to a selection on ΔR, other similar selections are available which considerably reduce the QCD background. One, in particular, exploits the boosted configuration of such a Higgs events. In this selection, a cut on the p_T of the Higgs system defined as in Equa-

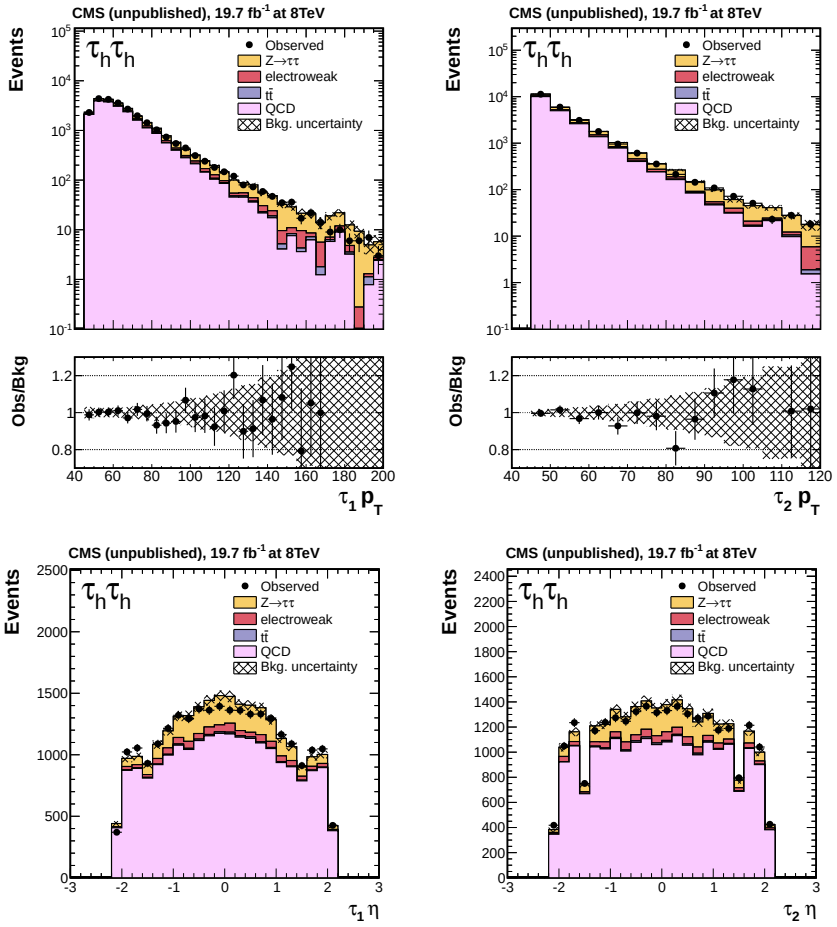

Figure 29: Transverse momentum p_T (upper row) and pseudorapidity η (lower row) for the selected tau with the higher p_T (τ_1, left column) and tau with the lower p_T (τ_2, right column). The η distributions present a small discrepancy which is due to the QCD background estimation. This effect is known, it is evident only in these plots and has no impact on the analysis, therefore no reweigh procedure is applied to correct it.

tion 38 also reduces the background by a similar amount. Application of such a cut both reduces the QCD multijet background by a similar amount while simultaneously removing the kinematic bias of the mass distribution towards low mass, thus allowing for a flatter mass distribution of the QCD events.

$$p_T^{Higgs} = \left(\vec{p}_T^{\,1} + \vec{p}_T^{\,2} + \vec{\not{E}}_T\right)_T \tag{38}$$

As a common baseline, a cut on $p_T^H > 100$ GeV is applied. This allows for the rejection of 97% of the otherwise overwhelming QCD background while retaining up to 70% of the Higgs signal, depending

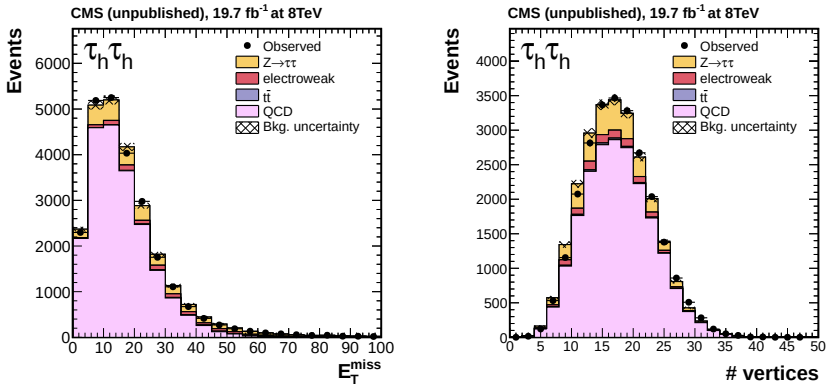

Figure 30: Transverse missing energy $\not{E}_T$ (left, upper row) and number of reconstructed primary vertices (lower row). The number of PV distribution presents a small discrepancy which is due to the QCD background estimation. This effect is known, it is evident only in this plot and has no impact on the analysis, therefore no reweigh procedure is applied to correct it.

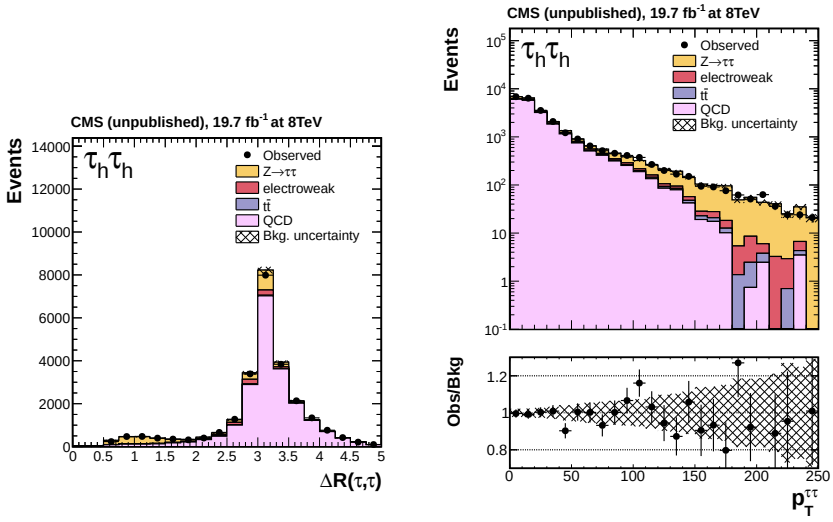

Figure 31: Separation in ΔR between the two signal taus, after the lepton selection (left) and Higgs candidate p_T (right). In the QCD events, the taus tend to be apart from each other and the transverse momentum of the Higgs system is low.

on the production mode. In fact the high tau p_T threshold already select events where the Higgs system is boosted. The effect of this selection on the $m_{\tau\tau}$distribution is shown in Fig. 36.

The selection based on the p_T of the Higgs system is used in the SM analysis only, whereas in the MSSM analysis no selection that implies a boost of the system, i.e. the requirement of an additional

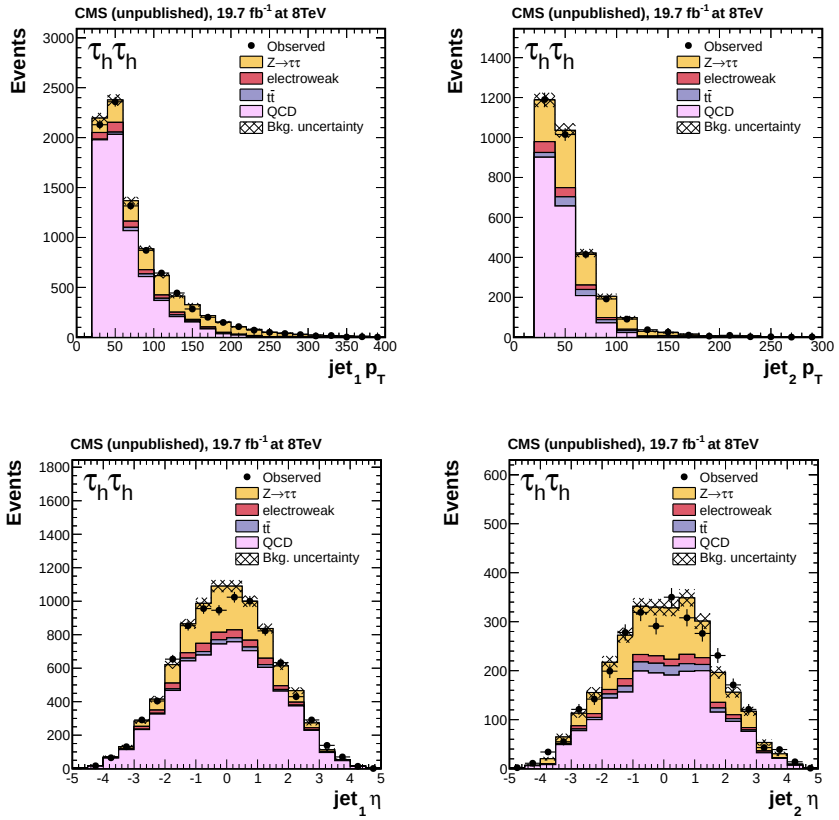

Figure 32: Transverse momentum p_T (upper row) and pseudorapidity η (lower row) for the leading jet (left column) in events with at least one jet and for the trailing jet (right column) in events with at least two jets.

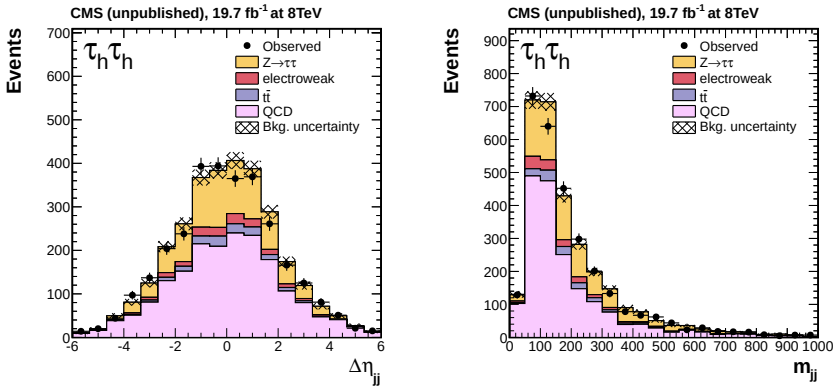

Figure 33: Difference between the two leading jets in pseudorapidity $|\Delta\eta_{jj}|$ (left) and invariant mass of the two leading jets m_{jj} (right) for events with at least two jets with $p_T > 30$ GeV.

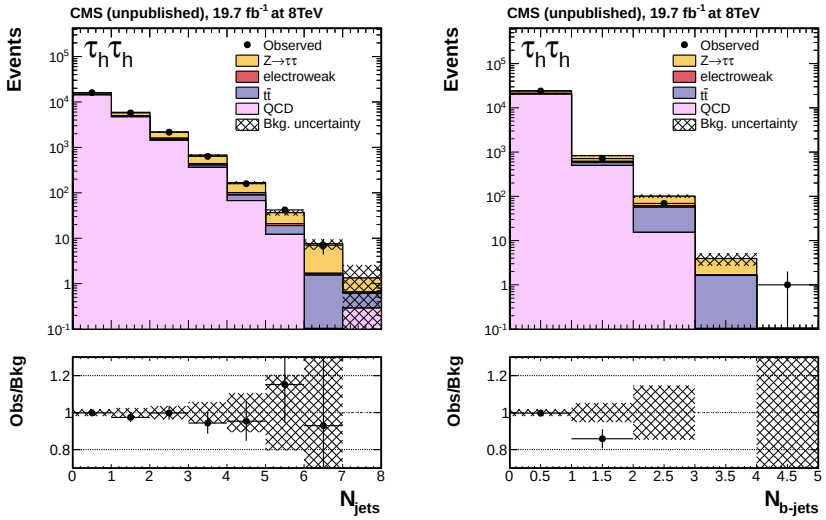

Figure 34: Number of jets with $p_T > 30$ (left) and number of b-tagged jet with $p_T > 20$ (right). The discrepancy between the observed data and the prediction in the rightmost plot is due to a contamination of $t\bar{t} \to \mu\mu$ events in the DY embedded sample. This is not relevant in the SM analysis because, effectively only the events in the zero b–jet bin are employed.

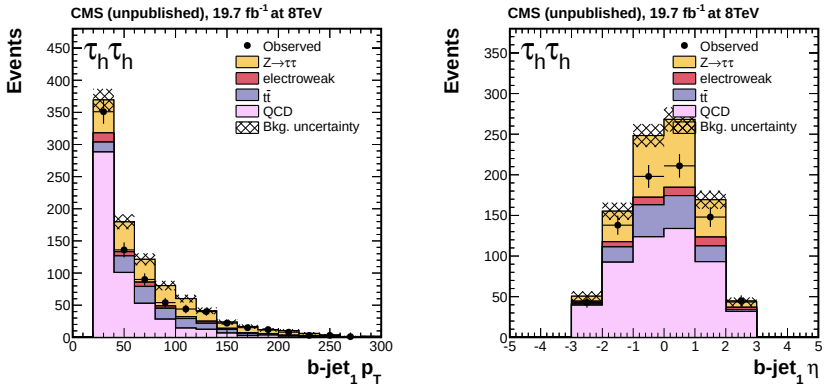

Figure 35: Transverse momentum p_T (left) and pseudorapidity η (right) for the leading b-tagged jet with $p_T > 20$ GeV in events passing the b-tag category selections The discrepancy between the observed data and the prediction is due to a contamination of $t\bar{t} \to \mu\mu$ events in the DY embedded sample. This is not relevant in the SM analysis because events with at least one b–jet are rejected.

jet, a cut on the angular separation of the taus or a cut on the p_T of the Higgs system is applied. This guarantees the analysis to be model independent. This affects the amount and the shape of the

QCD contamination, that remains by far the dominant background in the MSSM analysis.

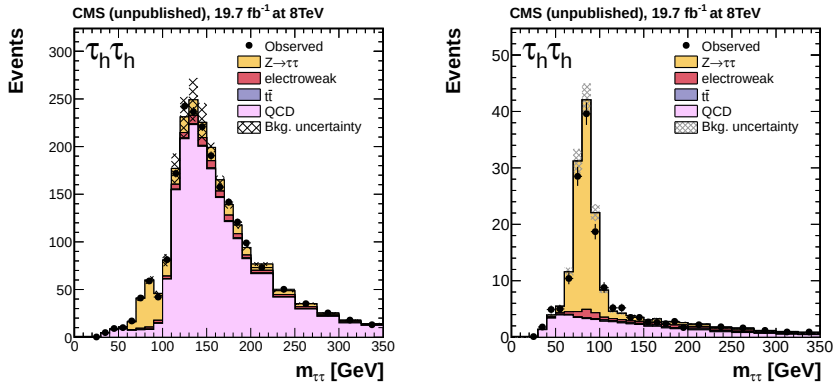

Figure 36: Di-tau invariant mass distribution $m_{\tau\tau}$before (left) and after (right) requiring $p_T^H$to be larger than 100 GeV. The QCD background is vastly reduced, and its shape is almost flat and much easier to model.

3.4.5 b–jet veto

The Higgs production processes directly probed by this analysis, gluon–gluon fusion and VBF, do not explicitly involve any b–quarks. Therefore, in order to reduce primarily the $t\bar{t}$ background, the events containing at least one jet with $p_T > 20$ GeV, $\eta < 2.4$ and passing the medium CSV working point (defined in Sec. 3.3.6) are rejected. The signal acceptance is reduced by 5% and 2% for the VBF and the gluon-gluon fusion processes respectively, whereas, at the same time, the $t\bar{t}$ contribution is reduced by 75%.

3.5 EVENT CLASSIFICATION

The events that pass the lepton selection, the p_T^Hcut and the b–tag veto are further sorted into mutually exclusive categories, defined by the presence of additional jets and their topology and by the kinematics of the Higgs candidate. It is therefore possible to single out signal enriched regions of the phase space by exploiting the peculiar experimental signatures of the gluon–gluon fusion and VBF Higgs production modes.

3.5.1 2 jets, VBF

The Higgs produced via Vector Boson Fusion presents a distinctive experimental signature. The two spectator quarks initiate two oppositely directed, forward jet and the hadronic activity in the rapidity gap is expected to be small. Since these two jets are back-to-back, the invariant di-jet invariant mass is large.

The selections applied in VBF category are reported below:

- two jets with $p_T > 30$ GeV (leading jet $p_T > 50$ GeV in case diTauJet trigger is fired)
- $|\Delta\eta_{jj}|$ between the two jets > 3.5
- no jets (with $p_T > 30$ GeV) in between them
- di-jet invariant mass $m_{jj} > 500$ GeV
- $p_T > 100$ GeV of the Higgs system

These selections are softer compared to the corresponding ones in the semi-leptonic channels. The reason of this choice is that the QCD estimation uncertainty is statistically limited in the control region. Using a selection tighter than what proposed below, the QCD uncertainty would grow with a negative impact on the analysis sensitivity. With the following selections the QCD uncertainty is kept at the level of 30%. Moreover, the high p_T threshold of the taus already reduces the signal acceptance and a tighter VBF selection is not going to improve signal purity.

3.5.2 1 jet, high Higgs p_T

This category collects events that fail to enter the VBF category, but have of at least 1 jet with transverse momentum exceeding 30 or 50 GeV in case the di-tau or the di-tau plus jet trigger is fired, respectively. To further reduce the QCD background to a negligible level, the transverse momentum of the Higgs system, p_T^H, is required to exceed 170 GeV. The remaining background contamination is formed almost exclusively by DY$\rightarrow \tau\tau$ events. The high Higgs boost drastically improves the Z/H mass separation and make this category very sensitive to the gluon-gluon fusion signal.

3.5.3 1 jet, medium Higgs p_T

The events not included in the former two categories are grouped in this category. Thanks to the low signal over background ratio, this category provides additional statistical power for the *in-situ* calibration of the tau energy scale and tau identification efficiency uncertainties.

3.6 ESTIMATES OF THE BACKGROUND CONTRIBUTIONS

3.6.1 Drell-Yan $Z/\gamma^\star \to \tau\tau$

The most important irreducible background, $Z/\gamma^\star \to \tau\tau$, is estimated using the so-called *embedded* sample, detailed in Ref. [72]. This sample is derived from a selection of inclusive $Z \to \mu\mu$ events in data where each muon has been interpreted as a reconstructed τ lepton. The decay of these leptons is simulated using *Tauola* (Ref. [109]). The inclusive yield of the embedded sample is normalized to the expected yield from Drell-Yan Monte Carlo, where the simulation is normalized according to a control region of inclusive $Z \to \mu\mu$ events where all correction factors have been applied. This normalisation is performed after requiring two, medium isolated, opposite charge τ_h and passing the selection described in Section 3.4.2 and the full suite of scale factors. This normalisation is further cross checked with a control region of $Z \to ee$ events.

An additional shape uncertainty is further propagated into the DY shape by assessing the statistical uncertainty in each mass bin the sample yielding into a set of independently floating bin-by-bin uncertainties. This goes on top of the shape systematic uncertainty related to the uncertainty on the tau energy scale described in [73] and covers residual possible shape biases.

In the VBF category the $Z \to \tau\tau$ mass template is taken from a region where the jet selection is relaxed to $m_{jj} > 200$ and $|\Delta\eta_{jj}| > 2.0$. normalisation is fixed to the yield obtained when the full selection is applied. This ensures for a smoother template and smaller bin by bin shape uncertainties.

Since the embedded samples originates from di-muon data sample, a contamination of genuine $t\bar{t} \to \mu\mu + X$ events is present. This is expected to be negligible for all the SM categories and for no b-tag MSSM category, since the b-tag veto there applied significantly reduces $t\bar{t}$ like event.

In the b-tag category, however, where at least one b-jet must be present, the $t\bar{t}$ contamination in the embedded sample in enhanced and measures up to 30% in the high mass (above 200 GeV) tail of the embedded sample. To correct for this effect, the shape obtained using a Monte Carlo $t\bar{t} \to \mu\mu + X$ sample, on which the embedding procedure is applied, is subtracted from the DY embedded shape.

3.6.2 QCD Multijets

In the $\tau_h\tau_h$-channel the background contribution from QCD multijet events is the second major background and originates from jets being mis-identified as τ_h. The estimate of QCD multijet background is

based on the fact that the combinations of the reconstructed τ_h candidates are uncorrelated. Therefore the QCD enriched, same charge region (same-sign, SS) and the QCD background in the signal selected opposite charge region(opposite-sign, OS) behave similarly. However, because much of the fake di-τ events originate from di-jet events the rate of OS to SS QCD events is not the same.

To estimate the rate of production an additional control region defined by OS non-isolated τ leptons is utilized. This thus defines three QCD enriched control regions to regulate the shape and yield of the QCD multijet background:

- **SS isolated** : Full event selection applied except the opposite charge requirement is inverted to require same charge
- **SS non-isolated** : Same charge di-τ_h events where both τ_h pass full identification and are loosely isolated ($\sum p_T$ in the isolation cone < 10 GeV). Overlap with the SS isolated control region is avoided by further requiring that at least one of the two taus fails the HPS combined isolation 3–hits Medium WP.
- **OS non-isolated** : Opposite charge di-τ_h events where both τ_h pass full identification and are loosely isolated ($\sum p_T$ in the isolation cone < 10 GeV). Overlap with the OS isolated signal region is avoided by further requiring that at least one of the two taus fails the HPS combined isolation 3–hits Medium WP.

The choice of the relaxed isolation thresholds is optimised to retain sizeable statistics in the region from which the QCD shape is taken, thus allowing to obtain a smooth template. However, the tau isolation is found to have a mild correlation with some observables, most notably the SVfit di-tau mass. In fact, if the QCD shape is taken from a very loosely isolated region, which is distant from the signal, fully isolated region, it is possible to introduce biasses in the mass distribution. This effect is studied in SS events, where the QCD background dominates, and the threshold for the non-isolated regions are therefore chosen to avoid such mismodeling.

The choice of different isolation thresholds for non-isolated regions follows the idea of minimizing the shape bias, as could happen if a too loose threshold is chosen, while retaining a good statistics in the control regions so that the yield uncertainties are small and the shapes are smooth.

The shape of the QCD estimate in all variables is determined from the OS non-isolated region in data. The non-QCD backgrounds determined by Monte-Carlo scaled prediction are subtracted from the OS non-isolated region in data to obtain the QCD estimate. To validate the predicted shape is correct a comparison of the non-isolated QCD shape with the isolated QCD shape in the same sign region is performed. In this region, the non-QCD backgrounds are again

subtracted, however the contribution in the non-isolated region is almost completely negligible. All biases in the mass shape variables are found to be within associated bin uncertainties, thus no additional uncertainties nor corrections are applied to the QCD shape estimate.

The method described above is is used the 1-jet categories, because, when used in the VBF category, it shows clear statistical limitations that would negatively impact the QCD uncertainties and thus the expected limit and significance. These limitations would manifests themselves in both shape and normalisation as the low statistics in OS non-isolated does not allow to extract a smooth shape for the the QCD contribution and few events survive in the SS isolated region making the normalisation uncertainty large.

For this reason, in the VBF category, four QCD enriched control regions are defined to regulate the shape and yield of the QCD multijet background:

- **SS isolated**, relaxed VBF : Full event selection applied except the opposite charge requirement is inverted to require same charge and the VBF topological selection is relaxed $m_{jj} > 200$ GeV and $|\Delta\eta_{jj}| > 2.0$
- **SS non-isolated**, full VBF : Same charge di-τ_h events where both τ_h pass full identification and are loosely isolated ($\sum p_T$ in the isolation cone < 10 GeV). Overlap with the SS isolated control region is avoided by further requiring that at least one of the two taus fails the HPS combined isolation 3–hits Medium WP.
- **SS non-isolated**, relaxed VBF : Same charge di-τ_h events where both τ_h pass full identification and are loosely isolated ($\sum p_T$ in the isolation cone < 10 GeV), at least one of the two taus fails the HPS combined isolation 3–hits Medium WP and the VBF topological selection is relaxed $m_{jj} > 200$ GeV and $|\Delta\eta_{jj}| > 2.0$
- **OS non-isolated**, relaxed VBF : Opposite charge di-τ_h events where both τ_h pass full identification and are loosely isolated ($\sum p_T$ in the isolation cone < 10 GeV), at least one of the two taus fails the HPS combined isolation 3–hits Medium WP and the VBF topological selection is relaxed $m_{jj} > 200$ GeV and $|\Delta\eta_{jj}| > 2.0$

Since the tau isolation is very mildly correlated to the VBF topological variables such as m_{jj} and $|\Delta\eta_{jj}|$ (Fig. 37), it is therefore possible to decouple the two effects and break down the normalisation factor into two, factorized, terms: the first one gives the efficiency of passing the full VBF selection for QCD events (ratio of the events in SS isolated, full VBF to SS non-isolated, relaxed VBF) and the second one gives the isolation fake rate (ratio of the events in SS isolated, relaxed VBF to SS non-isolated, relaxed VBF).

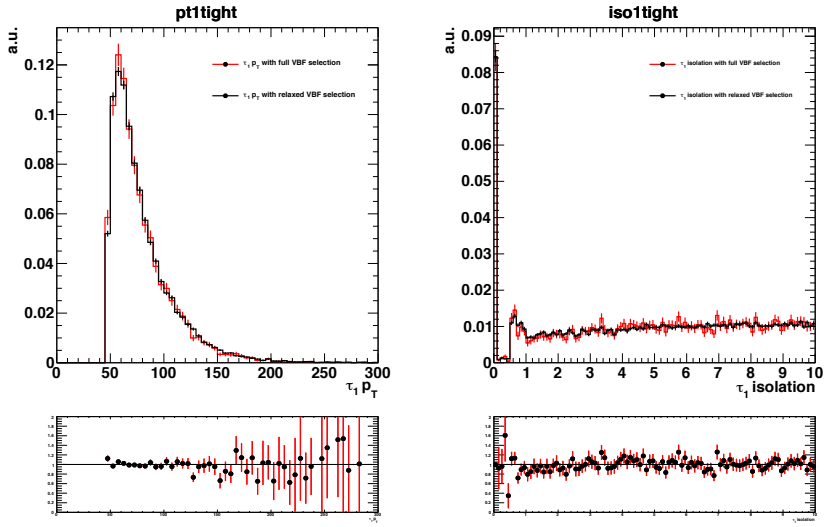

Figure 37: Transverse momentum p_T (left) and isolation (right) for the leading tau when full VBF selection ($m_{jj} > 500$ and $|\Delta\eta_{jj}| > 3.5$, in red) and relaxed VBF selection ($m_{jj} > 200$ and $|\Delta\eta_{jj}| > 2.0$, in black) are applied. The same charge requirement is applied. The isolation is relaxed to allow for sufficient statistics. The tau kinematic is mostly uncorrelated to VBF topology cuts.

These two extrapolation factors are then applied to OS non-isolated, relaxed VBF event yield to get the final QCD normalisation.

The uncertainty on the total number of events is determined by propagating the statistical uncertainty on all of the subtracted backgrounds along with the statistical uncertainty of the non-isolated region through the background subtraction. On top of this statistical uncertainty, the systematical uncertainty related to the background subtraction, due to the normalisation uncertainty of each of these background, is also accounted. The propagation of these uncertainties and all others through the calculation of the QCD normalisation gives an overall uncertainty of 35%.

An additional shape uncertainty is further propagated into the QCD shape by assessing the statistical uncertainty in each mass bin in the loose isolation sample yielding into a set of independently floating bin-by-bin uncertainties. This is a purely shape uncertainty: the yield variation caused by the modification of each single bin is reabsorbed and the normalisation is conserved. This avoids to double count the normalisation uncertainty due to the finiteness of the statistics. The coverage of the bin-by-bin uncertainties for systematic variations originating from using a loosened isolation template is validated by comparing the variations seen in the SS control region with the bin-by-bin uncertainties assigned for each category.

3.6.3 W/Z + jets

In the $\tau_h\tau_h$ channel, events with a W boson and additional jets in the final state constitute a minor background mainly constituted by events where the W boson decays into a hadronic tau and a mis-identified jet (as a τ_h).

The kinematics of this background are taken from the simulation, while the normalisation scale factor is taken from a W boson enriched control sample in the $\mu\tau_h$ channel. The specific selection of the full hadronic channel is applied in such control sample in order to reproduce the correspondent kinematics and, in addition, the transverse mass between the μ and the $\not{E}_T$ is required to be larger that 70 GeV in order to increase the W purity. The non-W samples were subtracted before determining this ratio. This scale factor is computed per each category in both SM and MSSM analyses and the numbers found and the uncertainties are summarized in Tab. 11.

Category	**Scale-Factor**	**Uncertainty**
Inclusive	0.73	30%
No b-tag	0.73	30%
B-tag	1.50	30%
Boost low	0.87	30%
Boost high	0.76	30%
VBF	1.03	30%

Table 11: W+Jets normalisation scale-factors and their corresponding uncertainty.

For the mass templates in both the Boost categories, the isolation is loosened down to 10 GeV (as for the QCD estimation in Section 3.6.2). This gives minimal bias on the mass shape and allows for large increase in MC event yields in these category. Following the same idea, in the VBF category the mass template is taken from a control region where the also the jet kinematics are loosened to have $m_{jj} > 200$ GeV and $\Delta\eta > 2.0$. In addition, isolation requirement is loosened down to $\sum p_T$ in the isolation cone < 10 GeV.

Z+jets events can occur as a background in two ways:

- both leptons, either ee or $\mu\mu$ are mis-identified as hadronic taus,
- one lepton, either e or μ is mis-identified as an hadronic taus, the second lepton falls outside the acceptance and a jet is mis-identified as an hadronic tau

In both cases the expected contribution is very small and both shape and normalisation are taken from the stitched MC scaled to the collected integrated luminosity according to the DY cross section.

In the VBF category the mass template is taken from a control region where the also the jet kinematics are loosened to have $m_{jj} > 200$ GeV and $\Delta\eta > 2.0$.

3.6.4 Di-bosons and top quark

The irreducible background from $t\bar{t}$ and di-boson production in each corresponding decay channel is taken from the simulation. The yield of $t\bar{t}$ events is normalized to the inclusive production cross section as measured by CMS [71], with an uncertainty of 8%. The event categorisation for the signal extraction corresponds to kinematic regions of the topology of $t\bar{t}$ events, which might not be well understood. The only appreciative uncertainty concerning the extrapolation into these regions originates from the uncertainty of the kinematics of $t\bar{t}$ events. Measurements by CMS indicate that these are well under control [70], which is also indicated by all control regions related to background from $t\bar{t}$ events. Therefore this uncertainty is assumed to be small.

The yields of di-boson production are normalized to the NLO cross sections as determined by [120, 119]. A correction based on the 7 TeV di-boson cross section measurements is applied to the overall cross section. A 15% uncertainty is assigned to this normalisation, which is close to the accuracy of recent measurements of CMS [69]. The overall contribution of this background is small.

3.7 RESULTS

The search for a SM Higgs decaying into a pair of tau leptons carried out in CMS encompasses several sub-channels and categories in order to increase the analysis sensitivity.

Two main analyses strategies, referred to as non-VH and VH in the followings, have been developed. The non-VH analysis is designed to probe the gluon–gluon fusion and the VBF Higgs production modes and comprises all the six possible di-tau final states $\mu\tau_h$, $e\tau_h$, $\tau_h\tau_h$, $e\mu$, $\mu\mu$, and ee. The fully hadronic channel $\tau_h\tau_h$, which is the main topic of this thesis, is a fundamental part of the non-VH analysis. The VH analysis is aimed at identifying the Higgs production in association with a W or a Z boson.

The two analyses and their several channels are combined together as complementary parts of the $H \to \tau\tau$ search. In this section, the combined results are presented. These results are published in Ref. [45].

3.7.1 Event categories

The categories used in the combined fit for the signal are shown in Fig. 38 and 39, for the 7 TeV and 8 TeV analyses respectively. In the case of the non-VH channels the 0-Jet categories are used to constrain some of the systematic uncertainties. The categories with signal sensitivity are with 1-Jet requirements, where the gluon–gluon fusion process gives a boosted Higgs recoiling off a jet originated by a parton in the initial state, or with 2-Jet requirements where the jets a have VBF signature. In these figures Low/High refers to the p_T range of the τ_h (muon) in the semi- (fully-) leptonic channels [1]. In the $\ell\tau_h$ channels these ranges correspond to 30-45 GeV, and >45 GeV, for the leptonic channels the *Low/High* ranges correspond to < 35 GeV and > 35 GeV. *Boost* refers to a High category ($p_T(\tau_h) > 45$ GeV) where in addtion the Higgs boson has $p_T > 100$ GeV. For the VBF categories, *Loose* refers to the selections: $m_{jj} > 500$ GeV and $\Delta\eta > 3.5$ in addition to the central jet veto. VBF *Tight* refers to the category with stringent requirements on the di-jet mass and di-jet $\Delta\eta$: $m_{jj} > 700$ GeV and $\Delta\eta > 4.0$, in the l-τ_h channels in addition there is a Higgs p_T selection as in the Boosted category. In total the combined fit for the SM Higgs boson is performed on 58 non-VH and 32 VH mass distributions.

1 The symbol ℓ refers to an electron or a muon, and the symbol L to any kind of reconstructed charged lepton, namely electron, muon, or τ_h.

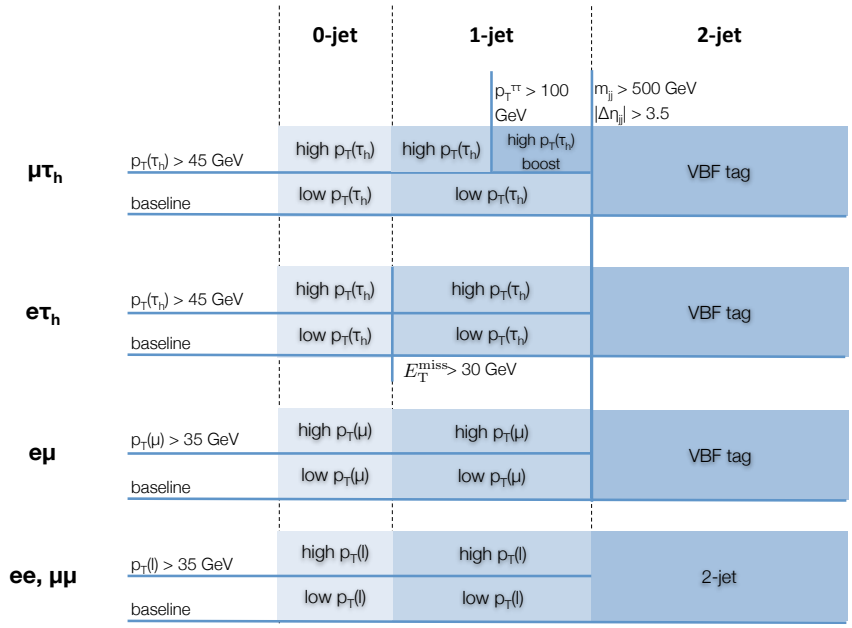

Figure 38: List of all 7 TeV, non-VH event categories used in the combined fit.

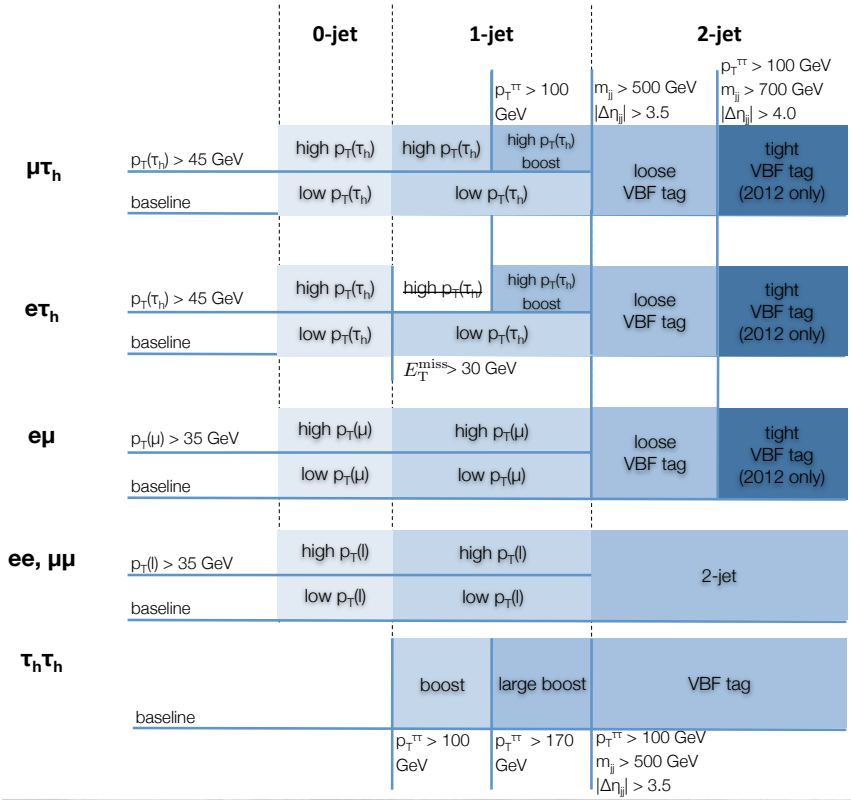

Figure 39: List of all 8 TeV, non-VH event categories used in the combined fit. For the fully hadronic channel, only 8 TeV data are used.

3.7.2 Signal extraction

3.7.2.1 *Final discriminants and mass distributions*

The search for an excess of SM Higgs boson events over the expected background involves a global maximum likelihood fit [21, 37] based on final discriminating variables:

- **full di-tau invariant mass** $m_{\tau\tau}$ reconstructed with the SVFit algorithm, used in the $\ell\tau$, $e\mu$, $\tau_h\tau_h$, ZH channels;
- **visible di-tau mass** $m_{\mathbf{vis}}$ used in the WH channel;
- **final discriminator** D for the ee and $\mu\mu$ channels.

This variable D is built for a given event from the output of two boosted decision trees B_1 and B_2. The two BDTs are based on kinematic variables related to the $\ell\ell$ system and the $\vec{\not{E}}_T$, on the distance of closest approach between the leptons, and, in the 2-jet category, the m_{jj} and $|\Delta\eta_{jj}|$ variables. The first BDT is trained to discriminate $Z \to \tau\tau$ from $Z \to \ell\ell$ events, whereas the second BDT is trained to discriminate $H \to \tau\tau$ from $Z \to \tau\tau$ events. Both BDTs are separately trained in the 2-jet category and in the combined 0-jet and 1-jet categories. The final discriminant is defined as

$$D = \int_{-\infty}^{B_1} \int_{-\infty}^{B_2} f_{sig}(B_1', B_2')\, dB_1'\, dB_2'. \tag{39}$$

In this expression, f_{sig} is the two-dimensional joint probability density for the signal. Therefore, D represents the probability for a signal event to have a value lower than B_1 for the first BDT and B_2 for the second BDT.

Figs. 40 and 41 show the $m_{\tau\tau}$ distributions observed for the 8 TeV dataset in the most sensitive categories of the $\mu\tau_h$, $e\tau_h$, $\tau_h\tau_h$, and $e\mu$ channels together with the background distributions resulting from the global fit described in detail below. The discriminator distributions for the 8 TeV dataset in the $\ell\ell$ channels are shown in figure 42. The signal prediction for a Higgs boson with $m_H = 125\,\text{GeV}$ is normalized to the SM expectation. The corresponding event yields for all event categories are given in Tab. 19 and 20 in App. **??**.

3.7.2.2 *Maximum likelihood fit*

For the global fit, the distributions of the final discriminating variable obtained for each category and each channel at 7 and 8 TeV are combined in a binned likelihood, involving the expected and observed numbers of events in each bin. The expected number of signal events is the one predicted by the SM for the production of a Higgs boson of mass m_H decaying into a pair of τ leptons, multiplied by a signal strength modifier μ, treated as free parameter in the fit.

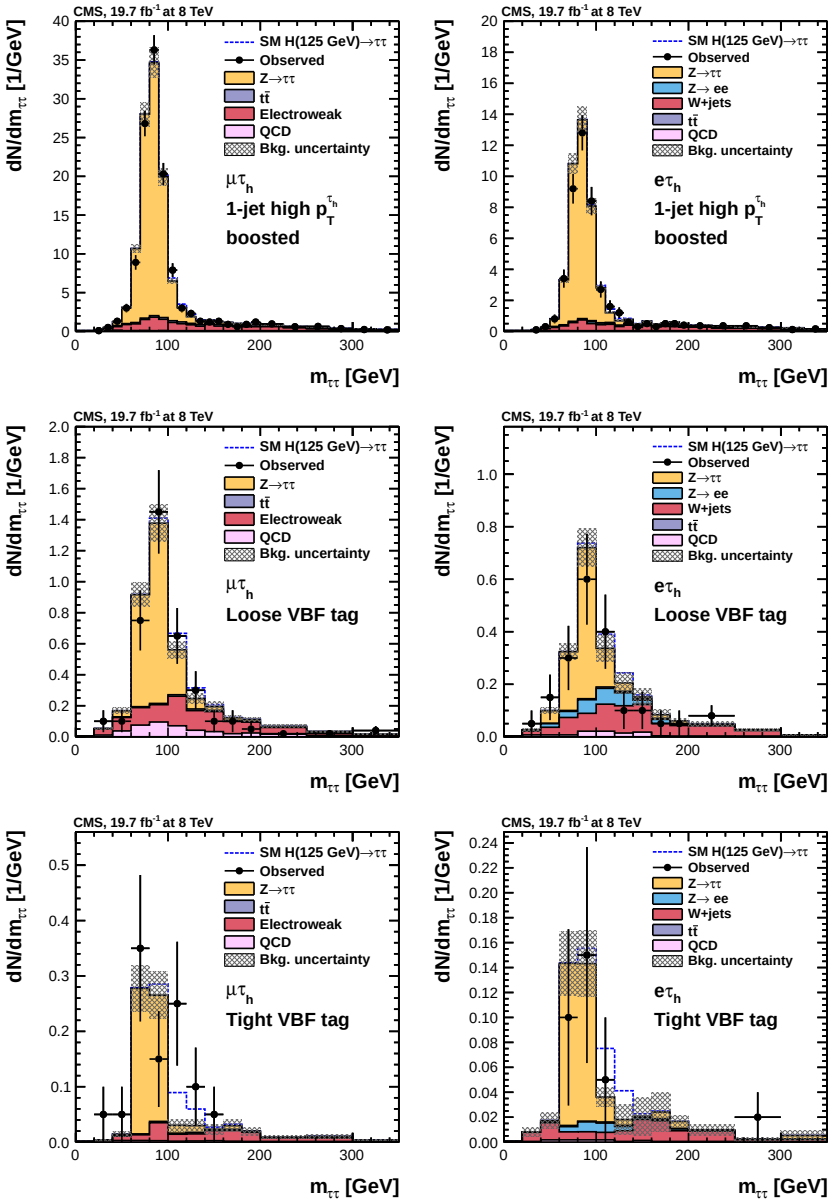

Figure 40: Observed and predicted $m_{\tau\tau}$ distributions in the 8 TeV $\mu\tau_h$ (left) and $e\tau_h$ (right) channels, and for the 1-jet high-$p_T^{\tau_h}$ boosted (top), loose VBF tag (middle), and tight VBF tag (bottom) categories. The normalization of the predicted background distributions corresponds to the result of the global fit. The signal distribution, on the other hand, is normalized to the SM prediction. The signal and background histograms are stacked.

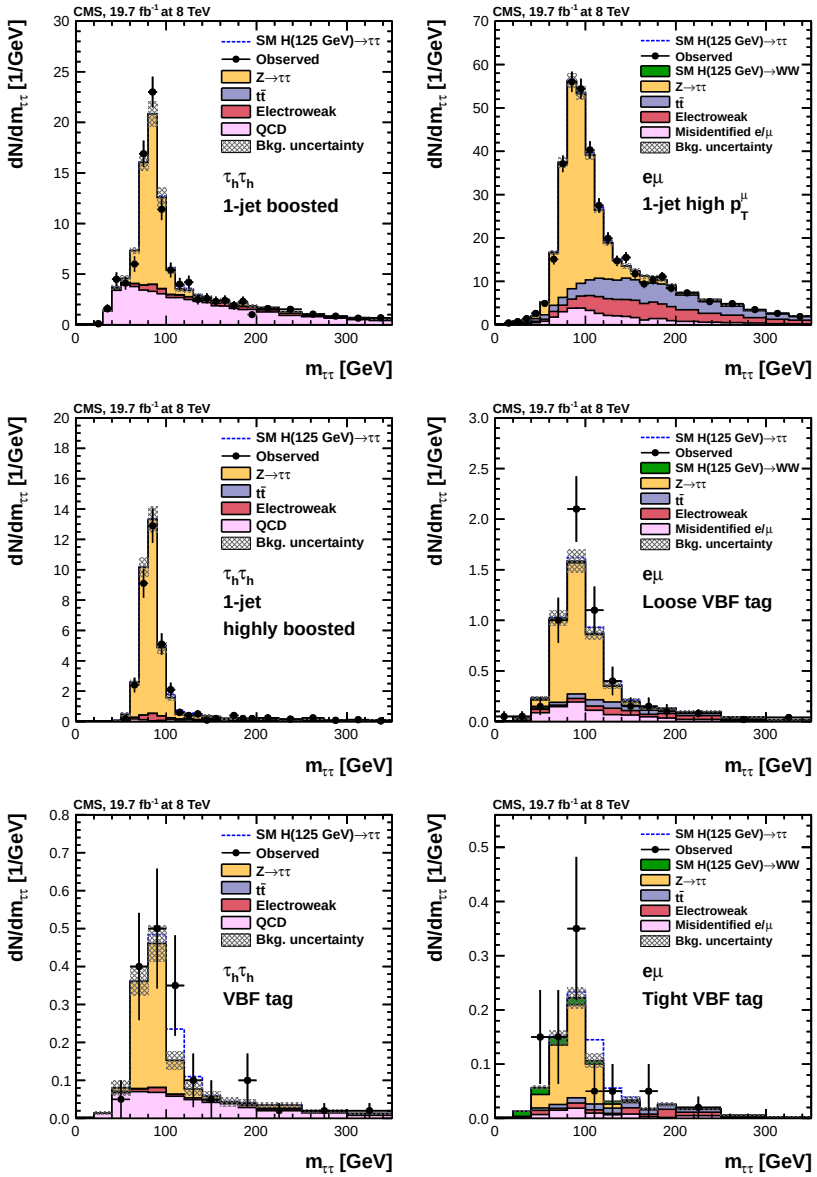

Figure 41: Observed and predicted $m_{\tau\tau}$ distributions in the 8 TeV $\tau_h\tau_h$ (left) channel for the 1-jet boosted (top), 1-jet highly-boosted (middle), and VBF-tagged (bottom) categories, and in the 8 TeV $e\mu$ (right) channel for the 1-jet high-p_T^{μ} (top), loose VBF tag (middle) and tight VBF tag (bottom) categories. The normalization of the predicted background distributions corresponds to the result of the global fit. The signal distribution, on the other hand, is normalized to the SM prediction. In the $e\mu$ channel, the expected contribution from $H \to WW$ decays is shown separately. The signal and background histograms are stacked.

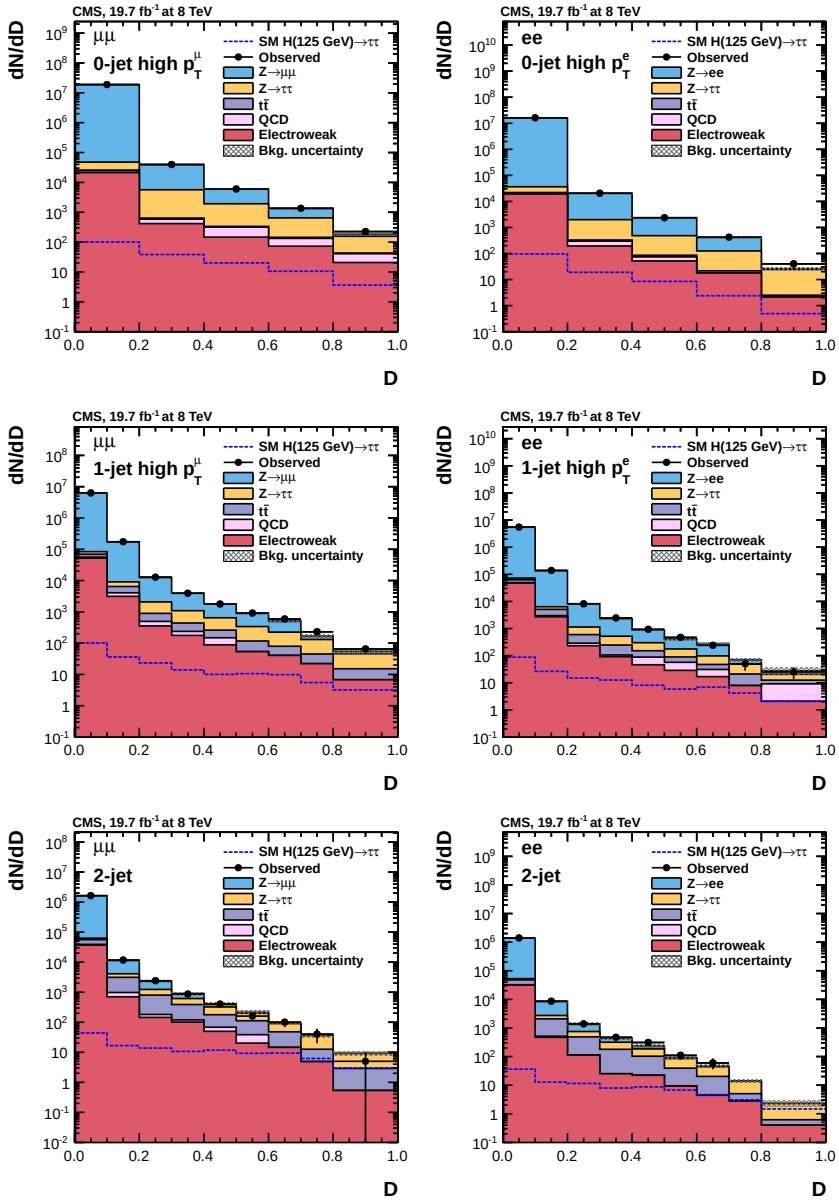

Figure 42: Observed and predicted distributions for the final discriminator D in the 8 TeV μμ (left) and ee (right) channels, and for the 0-jet high-p_T^ℓ (top), 1-jet high-p_T^ℓ (middle), and 2-jet (bottom) categories. The normalization of the predicted background distributions corresponds to the result of the global fit. The signal distribution, on the other hand, is normalized to the SM prediction. The open signal histogram is shown superimposed to the background histograms, which are stacked.

3.7.3 Systematic uncertainties

The values of a number of imprecisely known quantities can affect the rates and shapes of the $m_{\tau\tau}$ distributions for the signal and background processes. These systematic uncertainties can be grouped into theory related uncertainties, which are predominantly relevant for the expected signal yields, and into uncertainties from experimental sources, which can further be subdivided into uncertainties related to the reconstruction of physics objects and uncertainties in the background estimation. The uncertainties related to the reconstruction of physics objects apply to processes estimated with simulated samples, most importantly the signal processes. The distributions of the dominant background processes are estimated from data, and the corresponding systematic uncertainties are therefore mostly uncorrelated with the ones affecting the signal distributions.

The systematic uncertainties are represented by nuisance parameters that are varied in the fit according to their probability density function. A log-normal probability density function is assumed for the nuisance parameters affecting the event yields of the various background contributions. Systematic uncertainties that affect the template shapes, e.g. the τ_h energy scale uncertainty, are represented by nuisance parameters whose variation results in a continuous perturbation of the spectrum [75] and which are assumed to have a Gaussian probability density function.

3.7.3.1 *Systematic uncertainties evaluation*

The main experimental uncertainties in the decay channels involving a τ_h are related to the reconstruction of this object. The τ_h energy scale is obtained from a template fit to the τ_h mass distribution, such as the one shown in Fig. 26. In this fit, the shape of the mass distribution is morphed as a function of the τ_h energy scale parameter. The uncertainty of $\pm 3\%$ in the energy scale of each τ_h affects both the shape and the rate of the relevant signal and background distributions in each category. The τ_h identification and trigger efficiencies for genuine τ leptons sum up to an overall rate uncertainty of 6 to 10% per τ_h, depending on the decay channel, due to the different trigger and ℓ rejection criteria and additional uncertainties for higher $p_T^{\tau_h}$. For $Z \to \ell\ell$ events where jets, muons, or electrons are misidentified as τ_h, the estimation of the τ_h identification efficiency leads to rate uncertainties of 20 to 80%, including the statistical uncertainty due to the limited number of simulated events.

In the decay channels with muons or electrons, the uncertainties in the muon and electron identification, isolation, and trigger efficiencies lead to rate uncertainties of 2 to 4% for muons and 2 to 6% for electrons. The uncertainties related to the muon and electron energy scales are found to be negligible, except for the electron energy scale

uncertainty in the $e\mu$ and ee channels, which affects the normalization and shape of the $Z \to \tau\tau$ and signal $m_{\tau\tau}$distributions. The relative $\not{E}_T$ scale uncertainty of 5% affects the event yields for all channels making use of the $\not{E}_T$ in the event selection, in particular for the $\ell\tau_h$ channels due to the m_T selection [52]. This translates into yield uncertainties of 1 to 12%, depending on the channel and the event category. The uncertainties are largest for event categories with a minimum $\not{E}_T$ requirement and for background contributions with no physical source of $\not{E}_T$, e.g. the $Z \to ee$ contribution in the high-$p_T^{\tau_h}$ boosted category in the $e\tau_h$ channel. The uncertainty in the jet energy scale varies with jet p_T and jet η [32] and leads to rate uncertainties for the signal contributions of up to 20% in the VBF-tagged categories. For the most important background samples, the effect on the rate is, however, well below 5%. Because of the veto of events with b-tagged jets 3.3.6, uncertainties in the tagging efficiency for b-quark jets and in the mistagging efficiency for c-quark, light-flavour, and gluon jets result in rate uncertainties of up to 8% for the different signal and background components. The uncertainty in the integrated luminosity amounts to 2.2% for the 7 TeV analysis [53] and 2.6% for the 8 TeV analysis [54], yielding corresponding rate uncertainties for the affected signal and background samples.

The uncertainties related to the estimation of the different background processes are discussed in detail in the previous section, and only a summary is given here. For the different Drell–Yan decay modes, the uncertainty in the inclusive $Z \to \tau\tau$ yield is 3%, with additional extrapolation uncertainties in the different categories in the range of 2 to 14%. The uncertainties in the $W + \text{jets}$ event yields estimated from data are in the range of 10–100%. The values are dominated by the statistical uncertainties involved in the extrapolation from high to low m_T and due to the limited number of data events in the high-m_T control region. As a consequence, they are treated as uncorrelated with any other uncertainty. The QCD multijet background estimation results in 6 to 35% rate uncertainties for the LL' channels, except for the very pure dimuon final state and the VBF-tagged categories where uncertainties of up to 100% are estimated. Additional shape uncertainties are included in the $e\tau_h$, $\mu\tau_h$, and $e\mu$ channels to account for the uncertainty in the shape estimation from the control regions.

The rate and acceptance uncertainties for the signal processes related to the theoretical calculations are due to uncertainties in the parton distribution functions (PDF), variations of the renormalization and factorization scales, and uncertainties in the modelling of the underlying event and parton showers. The magnitude of the rate uncertainty depends on the production process and on the event category. In the VBF-tagged categories, the theoretical uncertainties concerning the $qq' \to H$ process are 4% from the PDFs and 3% from scale vari-

ations. The rate and acceptance uncertainties in the $gg \to H$ process in the VBF-tag categories are estimated by comparing the four different MC generators POWHEG, MADGRAPH, POWHEG interfaced with MINLO [95], and aMC@NLO [89]. They amount to 30% and thus become of similar absolute size as the uncertainties in the $qq' \to H$ process.

For the $gg \to H$ process, additional uncertainties are incorporated to account for missing higher-order corrections ranging from 10 to 41% depending on the category and on the decay channel. The combined systematic uncertainty in the background yield arising from diboson and single-top-quark production processes is estimated to be 15% for the LL′ channels based on recent CMS measurements [42, 36]. In the $\ell + L\tau_h$ and $\ell\ell + LL'$ channels, the uncertainties in the event yields of WZ production and ZZ production arise from scale variations and uncertainties in the PDFs, including the PDF uncertainties in the $gg \to ZZ$ event yields which are 44%. The resulting overall uncertainties range from 4 to 8%. The uncertainties in the small background from $t\bar{t} + Z$ production in the $\ell\ell + LL'$ channels amount to 50% [43].

In addition, uncertainties due to the limited number of simulated events or due to the limited number of events in data control regions are taken into account. These uncertainties are uncorrelated across bins in the individual templates. A summary of the considered systematic uncertainties is given in table 12.

Uncertainty	Affected processes	Change in acceptance
Tau energy scale	signal & sim. backgrounds	1–29%
Tau ID (& trigger)	signal & sim. backgrounds	6–19%
e misidentified as τ_h	$Z \to ee$	20–74%
μ misidentified as τ_h	$Z \to \mu\mu$	30%
Jet misidentified as τ_h	$Z + \text{jets}$	20–80%
Electron ID & trigger	signal & sim. backgrounds	2–6%
Muon ID & trigger	signal & sim. backgrounds	2–4%
Electron energy scale	signal & sim. backgrounds	up to 13%
Jet energy scale	signal & sim. backgrounds	up to 20%
$\not{E}_T$ scale	signal & sim. backgrounds	1–12%
$\varepsilon_{\text{b-tag}}$ b jets	signal & sim. backgrounds	up to 8%
$\varepsilon_{\text{b-tag}}$ light-flavoured jets	signal & sim. backgrounds	1–3%
Norm. Z production	Z	3%
$Z \to \tau\tau$ category	$Z \to \tau\tau$	2–14%
Norm. $W + \text{jets}$	$W + \text{jets}$	10–100%
Norm. $t\bar{t}$	$t\bar{t}$	8–35%
Norm. diboson	diboson	6–45%
Norm. QCD multijet	QCD multijet	6–70%
Shape QCD multijet	QCD multijet	shape only
Norm. reducible background	Reducible bkg.	15–30%
Shape reducible background	Reducible bkg.	shape only
Luminosity 7TeV(8TeV)	signal & sim. backgrounds	2.2% (2.6%)
PDF (qq)	signal & sim. backgrounds	4–5%
PDF (gg)	signal & sim. backgrounds	10%
Norm. ZZ/WZ	ZZ/WZ	4–8%
Norm. $t\bar{t} + Z$	$t\bar{t} + Z$	50%
Scale variation	signal	3–41%
Underlying event & parton shower	signal	2–10%
Limited number of events	all	shape only

Table 12: Systematic uncertainties, affected samples, and change in acceptance resulting from a variation of the nuisance parameter equivalent to one standard deviation. Several systematic uncertainties are treated as (partially) correlated for different decay channels and/or categories.

3.7.4 $\tau_h\tau_h$ channel results

The fully hadronic channel alone is sensitive to a Higgs signal produced with the rate predicted in the SM. In Fig. 43 the expected 95% CL upper limits, obtained using the modified frequentist construction CL_s [110, 124], are shown for the all the channels included in the analysis, for Higgs mass hypotheses between 90 and 145 GeV. At 125 GeV, the $\tau_h\tau_h$ channel is expected to exclude a signal strength equal 1.2 at the 95% CL. This is the second most sensitive channel, on par with $e\tau_h$ and after $\mu\tau_h$.

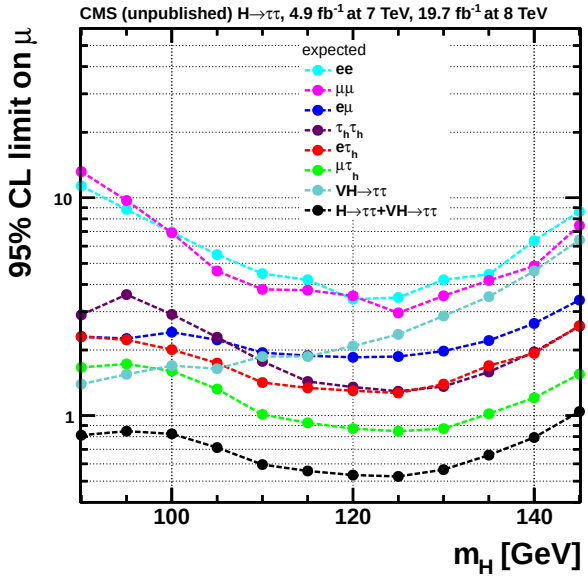

Figure 43: Expected 95% CL upper limit on the signal strength parameter $\mu = \sigma/\sigma_{SM}$ in the background only hypothesis, shown separately for the seven channels. The $\tau_h\tau_h$ channel is the second most sensitive channels after $\mu\tau_h$ for m_H =125 GeV, despite using only the 8 TeV data. For low m_H the limited signal acceptance, due to the high tau p_T threshold at the trigger level, reduces the sensitivity.

An excess of events in the region around $m_{\tau\tau}$125 GeV is visible in the $\tau_h\tau_h$ mass distributions in Fig. 41, left column. This excess is evident also in the observed 95% CL upper limit shown in Fig. 44 together with the expected limit obtained for the background-only hypothesis.

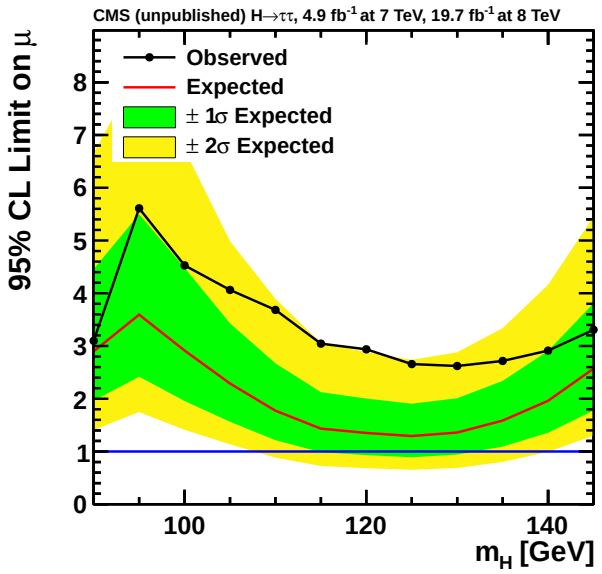

Figure 44: Combined observed 95% CL upper limit on the signal strength parameter $\mu = \sigma/\sigma_{SM}$, together with the expected limit obtained in the background-only hypothesis for the $\tau_h\tau_h$ channel. The bands show the expected one- and two-standard-deviation probability intervals around the expected limit.

3.7.5 Combined results

The excess of events observed in the most sensitive categories of figures 40 and 41 is highlighted in figure 45, which shows the observed and expected $m_{\tau\tau}$ distributions for the $\ell\tau_h$, $e\mu$, and $\tau_h\tau_h$ channels combined. The distributions are weighted in each category of each channel by the $S/(S+B)$ ratio where S is the expected signal yield for a SM Higgs boson with $m_H = 125\,\text{GeV}$ ($\mu = 1$) and B is the predicted background yield corresponding to the result of the global fit. The ratio is obtained in the central $m_{\tau\tau}$ interval containing 68% of the signal events. The figure also shows the difference between the observed data and expected background distributions, together with the expected distribution for a SM Higgs boson signal with $m_H = 125\,\text{GeV}$.

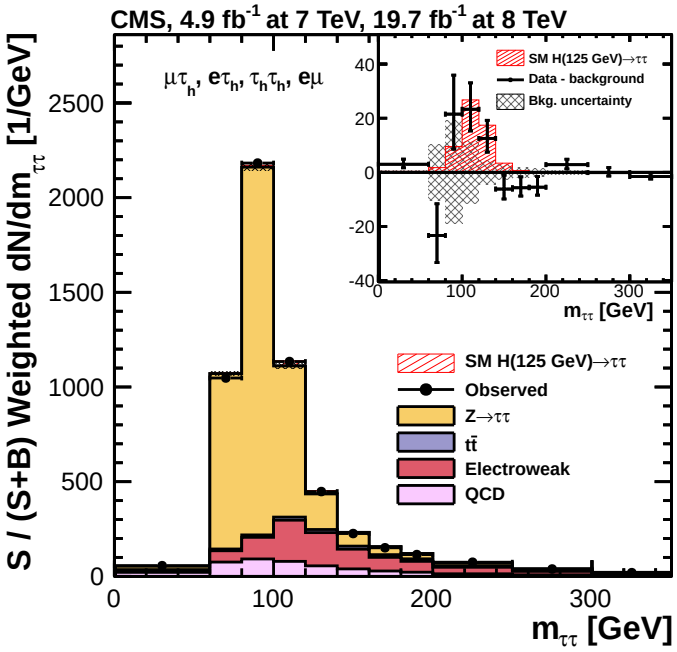

Figure 45: Combined observed and predicted $m_{\tau\tau}$ distributions for the $\mu\tau_h$, $e\tau_h$, $\tau_h\tau_h$, and $e\mu$ channels. The normalisation of the predicted background distributions corresponds to the result of the global fit. The signal distribution, on the other hand, is normalized to the SM prediction ($\mu = 1$). The distributions obtained in each category of each channel are weighted by the ratio between the expected signal and signal-plus-background yields in the category, obtained in the central $m_{\tau\tau}$ interval containing 68% of the signal events. The inset shows the corresponding difference between the observed data and expected background distributions, together with the signal distribution for a SM Higgs boson at $m_H = 125\,\text{GeV}$. The distribution from SM Higgs boson events in the WW decay channel does not significantly contribute to this plot.

The visible excess in the weighted $m_{\tau\tau}$ distribution is quantified by calculating the corresponding local p-values for the LL′ channels using a profile-likelihood ratio test statistics [21, 37]. Fig. 46 shows the distribution of local p-values and significances as a function of the Higgs boson mass hypothesis. The expected significance for a SM Higgs boson with $m_H = 125\,\text{GeV}$ is 3.6 standard deviations. For m_H between 110 and 130 GeV , the observed significance is larger than three standard deviations, and equals 3.4 standard deviations for $m_H = 125\,\text{GeV}$. The corresponding best-fit value for μ is $\hat{\mu} = 0.86 \pm 0.29$ at $m_H = 125\,\text{GeV}$.

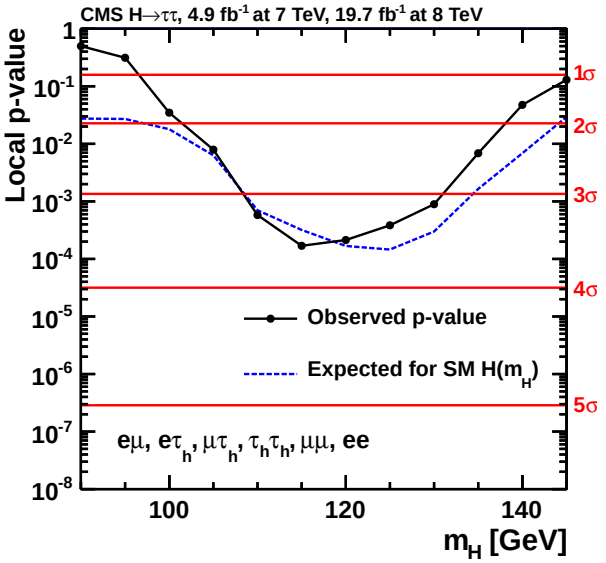

Figure 46: Local p-value and significance in number of standard deviations as a function of the SM Higgs boson mass hypothesis for the LL′ channels. The observation (solid line) is compared to the expectation (dashed line) for a SM Higgs boson with mass m_H. The background-only hypothesis includes the $pp \to H(125\,\text{GeV}) \to WW$ process for every value of m_H.

The m_{vis} or $m_{\tau\tau}$ distributions obtained for the 8 TeV dataset in the $\ell + L\tau_h$ and $\ell\ell + LL'$ channels are shown in figure 47. Because of the small number of expected events in each event category, different event categories are combined. The event yields for the individual event categories are given in table 21 in appendix **??**.

The following results include all decay channels considered. Fig. 48 left shows the observed 95% CL upper limit obtained using the modified frequentist construction CL_s [110, 124] together with the expected limit obtained for the background-only hypothesis for Higgs boson mass hypotheses ranging from 90 to 145GeV The background-only hypothesis includes the expected contribution from $H \to WW$ decays for $m_H = 125\,\text{GeV}$. The difference between evaluating this con-

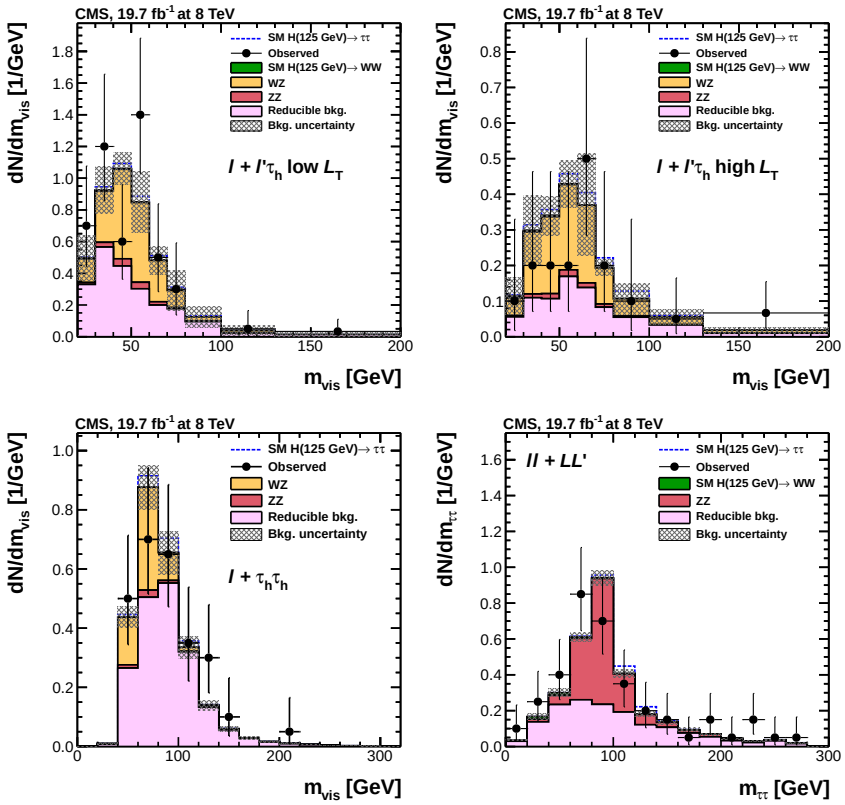

Figure 47: Observed and predicted m_{vis} distributions in the $\ell + \ell'\tau_h$ channel in the low-L_T (top left) and high-L_T (top right) categories, each for the 8 TeV dataset, and in the $\ell + \tau_h\tau_h$ channel (bottom left); observed and predicted $m_{\tau\tau}$ distributions in the $\ell\ell + LL'$ channel (bottom right). L_T is defined as the scalar sum of the p_T of the three leptons in the WH channels. It is used to define two categories in the 8 TeV WH analysis: low- and high-L_T,selection events with $L_T < 80$ and $L_T > 80$ GeV respectively. The normalization of the predicted background distributions corresponds to the result of the global fit. The signal distribution, on the other hand, is normalized to the SM prediction ($\mu = 1$). The signal and background histograms are stacked.

tribution at $m_H = 125\,\text{GeV}$ or at the corresponding m_H value for $m_H \neq 125\,\text{GeV}$ is less than 5%. An excess is visible in the observed limit with respect to the limit expected for the background-only hypothesis. The observed limit is compatible with the expected limit obtained in the signal-plus-background hypothesis for a SM Higgs boson with $m_H = 125\,\text{GeV}$ (figure 48 right). The excess is quantified in figure 49 which shows the local p-value as a function of m_H. For $m_H = 125\,\text{GeV}$, the expected p-value is smallest, corresponding to a significance of 3.7 standard deviations. The expected p-value is slightly smaller when including the $\ell + L\tau_h$ and $\ell\ell + LL'$ channels. The observed p-value is minimal for $m_H = 120\,\text{GeV}$ with a significance of 3.3 standard deviations. The observed significance is larger than three standard deviations for m_H between 115 and 130 GeV, and is equal to 3.2 standard deviations for $m_H = 125\,\text{GeV}$.

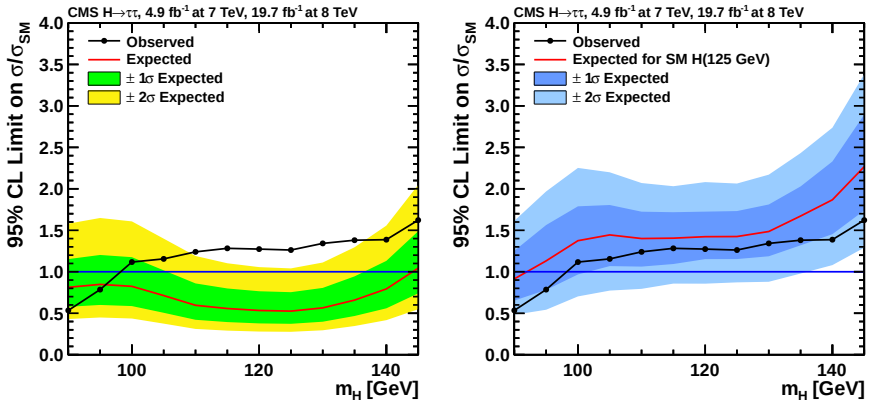

Figure 48: Combined observed 95% CL upper limit on the signal strength parameter $\mu = \sigma/\sigma_{SM}$, together with the expected limit obtained in the background-only hypothesis (left), and the signal-plus-background hypothesis for a SM Higgs boson with $m_H = 125\,\text{GeV}$ (right). The background-only hypothesis includes the $pp \to H(125\,\text{GeV}) \to WW$ process for every value of m_H. The bands show the expected one- and two-standard-deviation probability intervals around the expected limit.

The best-fit value for μ, combining all channels, is $\hat{\mu} = 0.78 \pm 0.27$ at $m_H = 125\,\text{GeV}$. Fig. 50 shows the results of the fits performed in each decay channel for all categories, and in each category for all decay channels. The uncertainties of the individual μ values in the 1-jet and 2-jet (VBF-tag) categories are of similar size, showing that both contribute about equally to the sensitivity of the analysis. The fraction of signal events from VBF production in the 1-jet categories and of signal events produced via gluon-gluon fusion in the 2-jet (VBF-tag) categories are each of the order of 20 to 30%; hence, it is not possible to fully disentangle the two production modes.

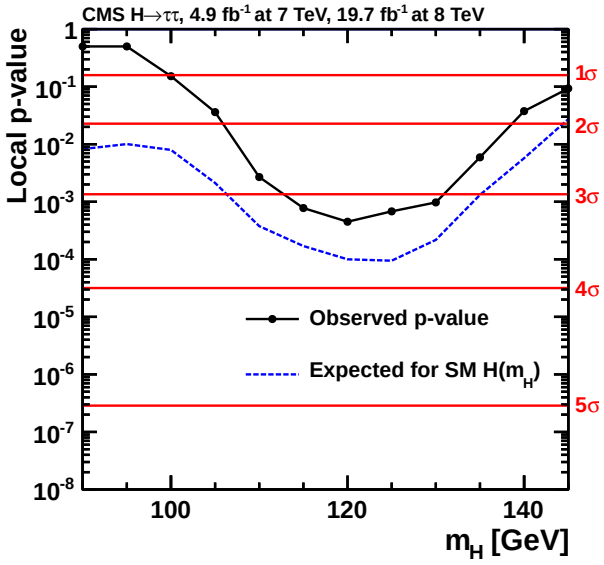

Figure 49: Local p-value and significance in number of standard deviations as a function of the SM Higgs boson mass hypothesis for the combination of all decay channels. The observation (solid line) is compared to the expectation (dashed line) for a SM Higgs boson with mass m_H. The background-only hypothesis includes the $pp \to H(125\,\text{GeV}) \to WW$ process for every value of m_H.

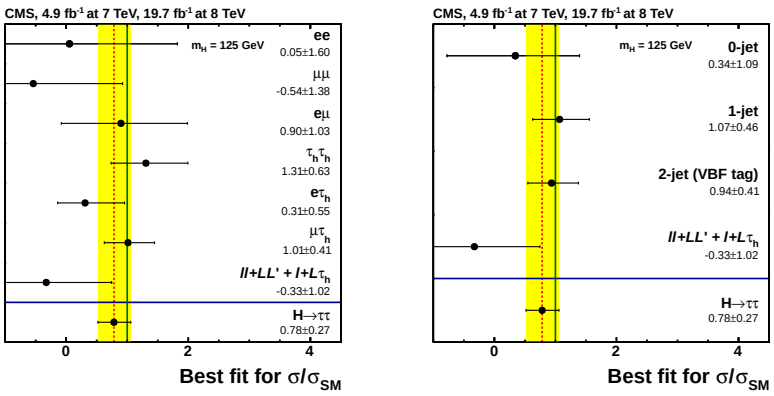

Figure 50: Best-fit signal strength values, for independent channels (left) and categories (right), for $m_H = 125\,\text{GeV}$. The combined value for the $H \to \tau\tau$ analysis in both plots corresponds to $\hat{\mu} = 0.78 \pm 0.27$, obtained in the global fit combining all categories of all channels. The dashed line corresponds to the best-fit μ value. The contribution from the $pp \to H(125\,\text{GeV}) \to WW$ process is treated as background normalized to the SM expectation.

The combined distribution of the decimal logarithm $\log(S/(S+B))$ obtained in each bin of the final discriminating variables for all event categories and channels is shown in figure 51. Here, S denotes the expected signal yield for a SM Higgs boson with $m_H = 125\,\text{GeV}$ ($\mu = 1$) and B denotes the expected background yield in a given bin. The plot illustrates the contribution from the different event categories that are sensitive to the different Higgs boson production mechanisms. In addition, it provides a visualisation of the observed excess of data events over the background expectation in the region of high $S/(S+B)$.

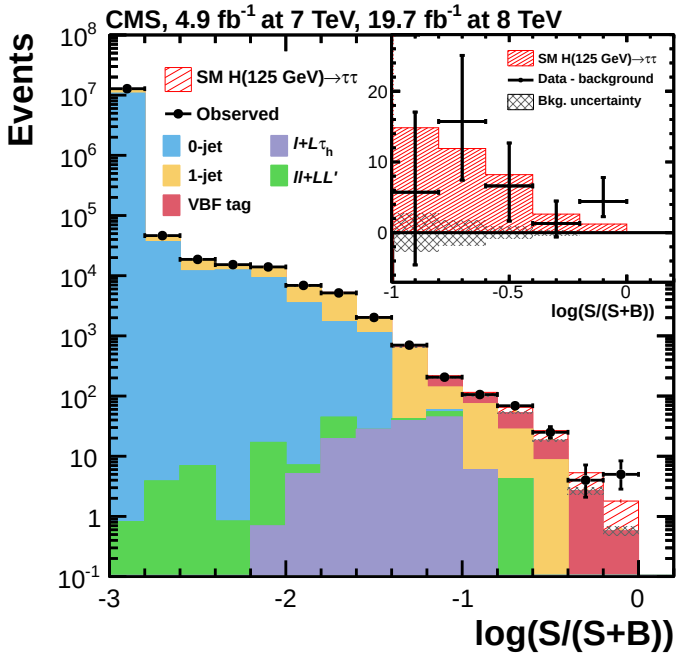

Figure 51: Combined observed and predicted distributions of the decimal logarithm $\log(S/(S+B))$ in each bin of the final $m_{\tau\tau}$, m_{vis}, or discriminator distributions obtained in all event categories and decay channels, with $S/(S+B)$ denoting the ratio of the predicted signal and signal-plus-background event yields in each bin. The normalisation of the predicted background distributions corresponds to the result of the global fit. The signal distribution, on the other hand, is normalized to the SM prediction ($\mu = 1$). The inset shows the corresponding difference between the observed data and expected background distributions, together with the signal distribution for a SM Higgs boson at $m_H = 125\,\text{GeV}$. The distribution from SM Higgs boson events in the WW decay channel does not significantly contribute to this plot.

3.7.5.1 *Higgs mass measurement*

Fig. 52 presents a scan of the negative log-likelihood difference, $-2\Delta \ln \mathcal{L}$, as a function of m_H. For each point in the parameter space, all nui-

sance parameters and the μ parameter are profiled. The background-only hypothesis includes the contribution from the $pp \to H(125\,\text{GeV}) \to WW$ process for every value of m_H. The difference between evaluating this additional background at $m_H = 125\,\text{GeV}$ or at the corresponding m_H value for $m_H \neq 125\,\text{GeV}$ is small. At the mass value corresponding to the minimum of the mass scan, the combined statistical and systematic uncertainties from the likelihood scan amount to 6 GeV. Additional contributions to the overall uncertainty of the mass measurement arise due to uncertainties in the absolute energy scale and its variation with p_T of 1 to 2% for τ_h candidates, electrons, muons, and the $\vec{p}_T$, summing up to an uncertainty of 4 GeV. Given the coarse m_H granularity, a parabolic fit is performed to $-2\Delta \ln \mathcal{L}$ values below 4. The combined measured mass of the Higgs boson is $m_H = 122 \pm 7\,\text{GeV}$.

3.7.5.2 *Higgs mass measurement*

Fig. 53 shows a likelihood scan in the two-dimensional (κ_V, κ_f) (left) and $(\mu_{ggH,ttH}, \mu_{qqH,VH})$ (right) parameter spaces for $m_H = 125\,\text{GeV}$. The κ_V and κ_f parameters quantify the ratio between the measured and the SM value for the coupling of the Higgs boson to vector bosons and fermions, respectively [113], whereas the $\mu_{ggH,ttH}$ and $\mu_{qqH,VH}$ parameters quantify the ratio between the measured and the SM value of the ggH plus ttH and VBF plus VH production rates respectively. To consistently measure deviations of the fermionic and the bosonic couplings of the Higgs boson, the $H \to WW$ contribution is considered as a signal process in this likelihood scan. For the VBF production of a Higgs boson that decays to a WW pair, the bosonic coupling enters both in the production and in the decay, thus providing sensitivity to the bosonic coupling despite the small expected event rates. All nuisance parameters are profiled for each point in the parameter space. The observed likelihood contours are consistent with the SM expectation of $\kappa_V = \kappa_f = 1$ and $\mu_{ggH,ttH} = \mu_{qqH,VH} = 1$.

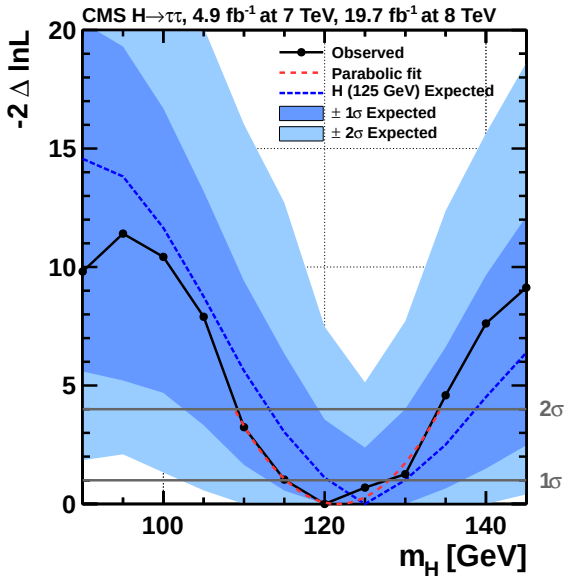

Figure 52: Scan of the negative log-likelihood difference, $-2\Delta \ln \mathcal{L}$, as a function of m_H . For each point, all nuisance parameters are profiled. For the likelihood scan as a function of m_H, the background-only hypothesis includes the $pp \to H(125\,\text{GeV}) \to WW$ process for every value of m_H. The observation (solid line) is compared to the expectation (dashed line) for a SM Higgs boson with mass $m_H = 125\,\text{GeV}$.

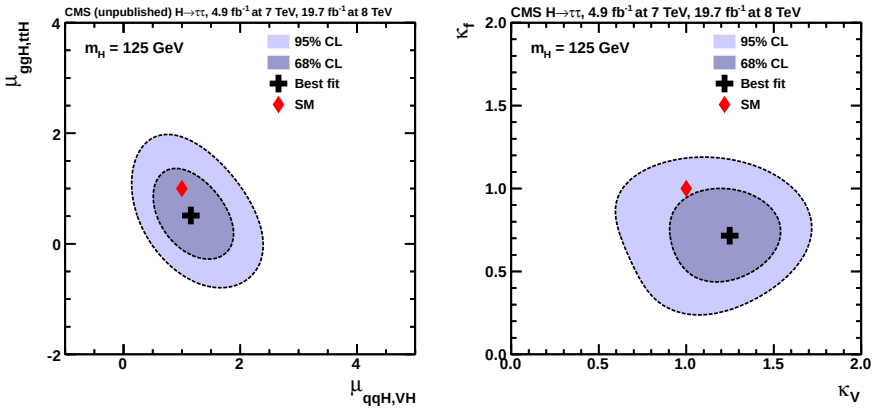

Figure 53: Scan of the negative log-likelihood difference, $-2\Delta \ln \mathcal{L}$, as a function of $\mu_{ggH,ttH}$ and $\mu_{qqH,VH}$ (left) and as a function of κ_V and κ_f (right). For each point, all nuisance parameters are profiled. The $H \to WW$ contribution is treated as a signal process.

4 SEARCH FOR A MSSM HIGGS BOSON DECAYING INTO A PAIR OF τ LEPTONS

4.1 INTRODUCTION AND MOTIVATIONS

A broad variety of precision measurements have shown the overwhelming success of the standard model (SM) [92, 135, 127] of fundamental interactions, which includes an explanation for the origin of the mass of the weak force carriers, as well as for the quark and lepton masses.

In the SM, this is achieved via the Brout–Englert–Higgs mechanism [85, 106, 107, 94, 108, 112], which predicts the existence of a scalar boson, the Higgs boson. However, the Higgs boson mass in the SM is not protected against quadratically divergent quantum-loop corrections at high energy, known as the hierarchy problem. In the model of supersymmetry (SUSY) [93, 136], which postulates a symmetry between the fundamental bosons and fermions, a cancellation of these divergences occurs naturally. The Higgs sector of the minimal supersymmetric extension of the standard model (MSSM) [86, 87] contains two scalar doublets that result in five physical Higgs bosons: a light and a heavy CP-even Higgs boson h and H, a CP-odd Higgs boson A, and two charged Higgs bosons $H^{\pm}$. At tree level the Higgs sector can be expressed in terms of two parameters which are usually chosen as the mass of the CP-odd Higgs boson m_A and $\tan\beta$, the ratio of the two vacuum expectation values of the two Higgs doublets.

The dominant neutral MSSM Higgs boson production mechanism is the gluon fusion process for small and moderate values of $\tan\beta$. At moderate-to-large values of $\tan\beta$ b-quark associated production is the dominant contribution, due to the enhanced Higgs boson Yukawa coupling to b quarks. Fig. 54 shows the leading-order diagrams for the gluon fusion and b-quark associated Higgs boson production. In the region of large $\tan\beta$ the branching fraction to tau leptons is also enhanced, making the search for neutral MSSM Higgs bosons in the $\tau\tau$ final state particularly interesting.

This thesis reports a search for neutral MSSM Higgs bosons in pp collisions at $\sqrt{s} = 7\,\text{TeV}$ and $8\,\text{TeV}$in the $\tau\tau$ decay channel. This work is published in Ref. [111]. Five different $\tau\tau$ signatures are studied, $e\tau_h, \mu\tau_h, e\mu$, $\mu\mu$, and $\tau_h\tau_h$. This work in centered on the $\tau_h\tau_h$ final state, which is detailed in Sec. 4.3.

The results are interpreted in the context of the MSSM with different benchmark scenarios described in Sec. 4.2 and also in a model

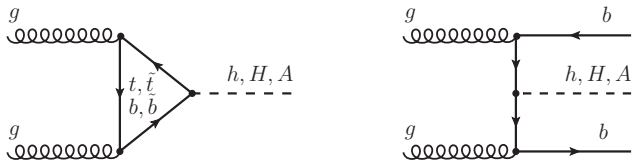

Figure 54: Leading-order diagrams of the gluon fusion (left) and b-quark associated Higgs boson production.

independent way, in terms of upper limits on the cross section times branching fraction $\sigma \cdot \mathcal{B}(\phi \to \tau\tau)$ for gluon fusion ($gg\phi$) and b-quark associated ($bb\phi$) neutral Higgs boson production, where ϕ denotes a single resonance with a narrow width compared to the experimental resolution, generally referring to any of the three neutral MSSM Higgs bosons h, A and H.

4.2 MSSM HIGGS BOSON BENCHMARK SCENARIOS

Traditionally, searches for MSSM Higgs bosons are expressed in terms of benchmark scenarios where the parameters $\tan\beta$ and m_A are varied, while the other parameters that enter through radiative corrections are fixed to certain benchmark values. At tree level the masses of the neutral MSSM scalar Higgs bosons h and H can be expressed in terms of $\tan\beta$ and m_A as follows

$$m^2_{H,h} = \frac{1}{2}\left[m^2_A + m^2_Z \pm \sqrt{(m^2_A + m^2_Z)^2 - 4m^2_Z m^2_A (\cos^2 2\beta)}\right], \quad (40)$$

which gives an upper bound on the light scalar Higgs boson mass, mh, in terms of the Z-boson mass of $m_h \leqslant m_Z \cos 2\beta$, which is below the excluded value of the LEP experiments [13]. After radiative corrections, values of the mass larger than the LEP limits are obtained with a maximum value of $m_h \sim 135\,\text{GeV}$ [78].

Taking into account higher-order corrections, the following extended set of parameters defines the MSSM Higgs sector: M_{SUSY} denotes the common soft-SUSY-breaking third-generation squark masses; μ is the higgsino mass parameter; M_1 (M_2) is the U(1) (SU(2)) gaugino mass parameter; X_t is the stop mixing parameter; A_t, A_b and A_τ are the trilinear Higgs–stop, Higgs–sbottom and Higgs–stau-lepton couplings, respectively; $m_{\tilde{g}}$ ($m_{\tilde{t}_1}$) is the gluino (stau) mass. A_t is obtained by the relation $A_t = X_t + \mu/\tan\beta$ and the value of the U(1)-gaugino mass parameter M_1 is generally fixed via the unification relation $M_1 = (5/3)M_2 \tan^2\theta_w$, where $\cos\theta_w = m_W/m_Z$.

Previous MSSM Higgs searches [33, 44, 2, 4, 8, 9, 5, 13] were interpreted in the m_h^{max} benchmark scenario [30, 31], which allows the

mass of the light scalar Higgs boson h to reach its maximum value of ~135 GeV. The ATLAS and CMS experiments have reported the observation of a new boson with mass around 125 GeV [3, 38, 41]. Evidence that this new boson also decays into tau lepton pairs has recently been reported by CMS [45]. If the new boson is interpreted as the light scalar MSSM Higgs boson h, a large part of the $\tan\beta$ and m_A parameter space in the m_h^{max} scenario is excluded. However, changes in some of the parameters open up a large region of the allowed parameter space again [105]. New benchmark scenarios [29] have thus recently been proposed where the mass of one of the scalar Higgs bosons, h or H, is compatible with the mass of the recently discovered Higgs boson of 125 GeVwithin a range of ± 3 GeV. This uncertainty is a conservative estimate of the theoretical uncertainty of the MSSM Higgs boson mass calculations [78]. Tab. 13 summarizes the main parameters of the benchmark scenarios considered in this study.

The traditional m_h^{max} scenario has been slightly modified to the m_h^{mod+} and m_h^{mod-} scenarios, where the different values of the stop mixing parameter yield a smaller light scalar Higgs boson mass than the maximal value of ~135 GeV. Other scenarios which have recently been proposed due to their interesting Higgs sector phenomenology compared to the SM are the light-stop scenario, which allows for a modified gluon fusion rate; the light-stau, which gives a modified $H \to \gamma\gamma$ rate; and the τ-phobic scenario, which gives a reduced Higgs decay rate to down-type fermions of up to 30% at large values of $\tan\beta$ and m_A. The value of m_A is generally varied between 90 and 1000 GeV. In the light-stop scenario the scan is only performed up to 600 GeV, because the calculation of the SUSY next-to-leading order (NLO) QCD corrections loses validity at larger masses. The range of $\tan\beta$ values studied for each scenario is chosen such that the calculation of the light scalar Higgs boson mass is well defined. In contrast to the other scenarios, that interpret the light scalar Higgs h as the recently discovered Higgs boson, the low-m_H scenario assumes the heavy scalar MSSM Higgs H as the new discovered state. In this scenario, the parameters have been chosen such that the mass of the light scalar Higgs h is not excluded by the LEP results [13]. The mass of the pseudoscalar Higgs boson is set to $m_A = 110$ GeV and the higgsino mass parameter μ and $\tan\beta$ are varied as shown in Tab. 13.

The neutral MSSM Higgs boson production cross sections and the corresponding uncertainties are provided by the LHC Higgs Cross Section Group [114]. The cross sections for the gluon fusion process in the m_h^{max} scenario have been obtained with the NLO QCD program HIGLU [131, 132], for the contribution of the top loop, the bottom loop, and the interference. The top loop contribution has been further corrected using the next-to-next-to-leading order (NNLO) program GGH@NNLO [99, 18, 123, 98, 19]. In the case of the other bench-

Table 13: MSSM benchmark scenarios.

Parameter	m_h^{max}	m_h^{mod+}	m_h^{mod-}
m_A	90–1000 GeV	90–1000 GeV	90–1000 GeV
$\tan\beta$	0.5–60	0.5–60	0.5–60
M_{SUSY}	1000 GeV	1000 GeV	1000 GeV
μ	200 GeV	200 GeV	200 GeV
M_1	$(5/3)\, M_2 \tan^2\theta_W$	$(5/3)\, M_2 \tan^2\theta_W$	$(5/3)\, M_2 \tan^2\theta_W$
M_2	200 GeV	200 GeV	200 GeV
X_t	2 M_{SUSY}	1.5 M_{SUSY}	-1.9 M_{SUSY}
A_b, A_t, A_τ	$A_b = A_t = A_\tau$	$A_b = A_t = A_\tau$	$A_b = A_t = A_\tau$
$m_{\tilde{g}}$	1500 GeV	1500 GeV	1500 GeV
$m_{\tilde{l}_3}$	1000 GeV	1000 GeV	1000 GeV

Parameter	light-stop	light-stau	τ-phobic	low-m_H
m_A	90–600 GeV	90–1000 GeV	90–1000 GeV	110 GeV
$\tan\beta$	0.7–60	0.5–60	0.9–50	1.5–9.5
M_{SUSY}	500 GeV	1000 GeV	1500 GeV	1500 GeV
μ	400 GeV	500 GeV	2000 GeV	300-3100 GeV
M_1	340 GeV	$(5/3)\, M_2 \tan^2\theta_W$	$(5/3)\, M_2 \tan^2\theta_W$	$(5/3)\, M_2 \tan^2\theta_W$
M_2	400 GeV	200 GeV	200 GeV	200 GeV
X_t	2 M_{SUSY}	1.6 M_{SUSY}	2.45 M_{SUSY}	2.45 M_{SUSY}
A_b, A_t, A_τ	$A_b = A_t = A_\tau$	$A_b = A_t, A_\tau = 0$	$A_b = A_t = A_\tau$	$A_b = A_t = A_\tau$
$m_{\tilde{g}}$	1500 GeV	1500 GeV	1500 GeV	1500 GeV
$m_{\tilde{l}_3}$	1000 GeV	245 GeV	500 GeV	1000 GeV

mark scenarios, the program SusHi [102] has been used as it includes the SUSY NLO QCD corrections [101, 97, 77, 79, 80] that are of importance in these alternative scenarios. In the SusHi calculations, the electroweak corrections due to light-fermion loop effects [11, 26] have also been included. For the $bb\phi$ process, the four-flavor NLO QCD calculation [81, 76] and the five-flavor NNLO QCD calculation, as implemented in bbh@nnlo [100] have been combined using the Santander matching scheme [96]. In all cross section programs used, the Higgs boson Yukawa couplings have been calculated with FeynHiggs [104, 103, 78, 88]. The Higgs boson branching fraction to tau leptons in the different benchmark scenarios has been obtained with FeynHiggs and hdecay [133, 82, 83], as described in Ref. [113].

4.3 ANALYSIS

4.3.1 Analysis strategy

This analysis is a natural extension of the SM Higgs to tau tau search presented in Ch. 3. The definition of the physics objects is the same as in Sec. 3.3, the events are preselected as described in Sec. 3.4.2 and the techniques used to estimate the background contamination correspond to what is detailed in Sec. 3.6.

The differences between the SM and the MSSM analysis are limited to:

- the b–tagged jets in the event are used to single out the $bb\phi$ process (Fig. 54, right), instead of being used as a veto (cfr. Sec. 3.4.5);
- any requirement that would imply the presence of and extra jet (excluding the b–jets produced in the $bb\phi$ process), thus forcing the Higgs to be boosted (such as the p_T^H cut applied in the SM 3.4.4), is dropped. In fact, the request of an additional jet would have introduced an undesired model-dependency. The production rate of an MSSM Higgs boson in association with jets depends on the particular benchmark scenario taken into consideration. Moreover, the kinematics of the Higgs boson, especially its transverse momentum, depend on $\tan\beta$. The request of an extra jet is equivalent to requiring the Higgs system to be boosted, therefore, if such requirement is applied, ideally the p_T of the Higgs should be reweighed and the signal acceptance re-evaluated for each different $\tan\beta$ point. These shortcomings would have narrowed the possibility to interpret the results in a wide number of MSSM scenarios. For this reason, the Higgs p_T cut is removed and similarly the di-tau plus jet trigger is not used and the signal acceptance reduction is estimated to be smaller than 5%, thus negligible.

4.3.2 Datasets and samples

For the MSSM analysis in the fully hadronic channel, only the data selected by the `HLT_DoubleMediumIsoPFTau35_Trk{1,5}_eta2p1` trigger have been used. The dataset names and the corresponding integrated luminosities are shown in Tab. 14. The total integrated luminosity is 18.3 fb^{-1} for which good quality runs are selected by applying the JSON file `Cert_190456-208686_8TeV_22Jan2013ReReco_Collisions12_JSON.txt`. As opposed to the SM analysis 3.2, the `HLT_DoubleMediumIsoPFTau{25,30}_Trk{1,5}_eta2p1_Jet30` trigger has not been used, to preserve model independency.

Data Sample for Event Selection 2012	Integrated Luminosity [pb^{-1}]
/TauParked/Run2012B-22Jan2013-v1/AOD	3870.0
/TauParked/Run2012C-22Jan2013-v1/AOD	7054.8
/TauParked/Run2012D-22Jan2013-v1/AOD	7369.0

Table 14: List of the samples used for the analysis of the data collected in 2012. The table lists all samples used for the main event selection. In the MSSM analysis, period 2012A is dropped and period 2012B is considered for a corresponding luminosity of 3870 pb^{-1}.

The MC samples used to model the backgrounds correspond exactly to what is used for the SM analysis, and are reported in Tab. 6. In addition, the MSSM MC signal samples for the $gg \to \phi$ and $gg \to bb\phi$ processes, modeled with the event generator *PYTHIA* 6.4 [130], are listed in Tab. 15.

MSSM Higgs Signal Processes		
Process	Dataset Name	$\sigma\times$ BR [pb]
$gg \to A$	/SUSYGluGluToHToTauTau_M-*_8TeV-pythia6-tauola	0.21 * 0.039
$qq \to bbA$	/SUSYBBHToTauTau_M-*_8TeV-pythia6-tauola	0.45 * 0.039
SM Higgs Signal Processes		
Process	Dataset Name	$\sigma\times$ BR [pb]
$gg \to H$	/GluGluToHToTauTau_M-*_8TeV-powheg-pythia6	19.27 * 0.0637
$qq \to qqH$	/VBF_HToTauTau_M-*_8TeV-powheg-pythia6	1.58 * 0.0637
$gg \to t\bar{t}/VH$	/WH_ZH_TTH_HToTauTau_M-*_8TeV-pythia6-tauola	1.12 * 0.0637

Table 15: Samples of simulated events used for the analysis of the data collected in 2012. The name of the file sets is to be extended by *Summer12-DR53X-PU_S10_START53_V*/AODSIM* for each sample in 2012. The production cross sections for the MSSM Higgs boson are given for the heavy neutral CP-odd Higgs boson A, with $m_\phi = 300\,\text{GeV}$, $\tan\beta = 8$ and in m_h^{max} scenario (cfr. Tab 13), whereas the production cross sections for the SM Higgs boson are given for $m_H = 125$ GeV.

4.3.3 Event classification

To further enhance the sensitivity of the MSSM search, the sample of selected events is split into two mutually exclusive event categories:

4.3.3.1 *no-btag*

This event category is mainly sensitive to the gluon-fusion Higgs production mechanism, Fig. 54 left. Events are required to have no b-tagged jets with $p_T > 20$ GeV.

4.3.3.2 *b-tag*

This event category is intended to exploit the production of Higgs bosons in association with b–quarks which is enhanced in the MSSM, Fig. 54 right. In this category at least one b–tagged jet with $p_T > 20$ GeV is required and not more than one jet with $p_T > 30$ GeV to suppress $t\bar{t}$ background

4.4 STATISTICAL ANALYSIS

To search for the presence of a MSSM Higgs boson signal in the selected events, a binned maximum likelihood fit is performed. The invariant mass of the tau-lepton pairs $m_{\tau\tau}$, reconstructed using the SVFit Sec. 3.3.8, is used as the input to the fit in the $e\tau_h$, $\mu\tau_h$, $e\mu$, and $\tau_h\tau_h$ final states.

The sensitivity of the $\mu\mu$ channel is enhanced by fitting the two-dimensional distribution of $m_{\tau\tau}$ versus the mass of the visible decay products, m_{vis}, utilizing the fact that most of the large $Z \to \mu\mu$ background contributing to this channel is concentrated in the m_{vis} distribution within a narrow peak around the Z-boson mass. The final mass and discriminant plots are shown in Fig. 55 and 56 for the no b–tag and b–tag categories respectively. The fit is performed simultaneously for the five final states and the two event categories, b–tag and no b–tag.

4.4.1 Systematic uncertainties

Various imperfectly known effects can alter the shape and the normalization of the invariant-mass spectrum. These can be sorted into two different classes, experimental and theoretical uncertainties. The experimental uncertainties, pertain either the reconstruction of the objects or the background estimation technique, are evaluated as described in Sec. 3.7.3.1. The theoretical uncertainties on the MSSM Higgs signal cross sections depend on $\tan\beta$, m_A, and the scenario considered, and can amount up to ~25%. In the cross section calculations the MSTW2008 [117] parton distribution functions are used, and the recommended prescription [117, 116] to compute the uncertainties is followed. The renormalization and factorization scales used in the theoretical calculations and the variation considered are summarized in Ref. [114]. Tab. 16 provides a summary of all the systematic uncertainties taken into account

The systematic uncertainties described above are incorporated in the fit via nuisance parameters and are treated according to the frequentist paradigm, as described in Ref. [21]. The uncertainties that affect the shape of the mass spectrum, mainly those corresponding to

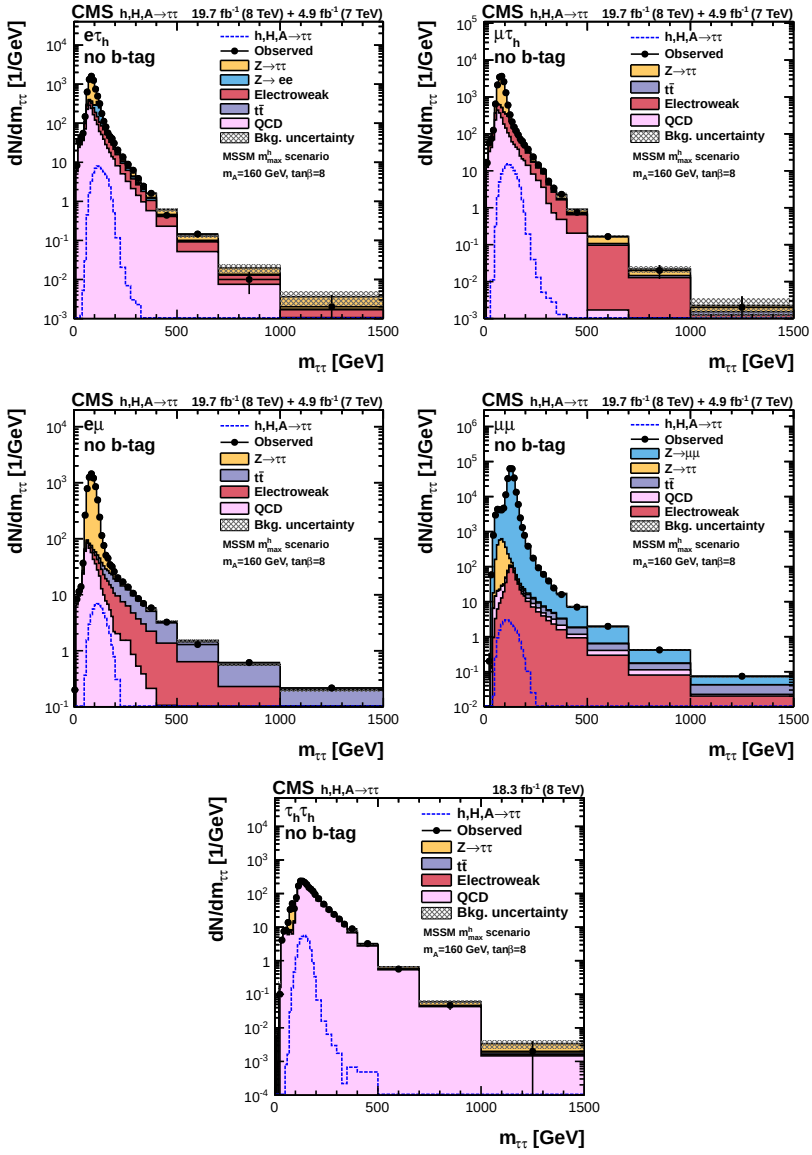

Figure 55: Reconstructed $\tau\tau$ invariant-mass in the no b-tag category for the $e\tau_h$, $\mu\tau_h$, $e\mu$, $\mu\mu$ and $\tau_h\tau_h$ channels. The electroweak background includes the contributions from $Z \to ee$, $Z \to \mu\mu$, W, di-bosons, and single top. In the $\mu\mu$ channel, the $Z \to \mu\mu$ contribution is shown separately. The expected signal yield of the MSSM Higgs bosons h, H, and A for $m_A = 160\text{GeV}$and $\tan\beta = 8$ in the m_h^{max} scenario is also shown.

the energy scales, are represented by the nuisance parameters whose variation results in a continuous perturbation of the spectrum. Shape uncertainties due to limited statistics are incorporated via nuisance parameters that allow for uncorrelated single-bin fluctuations of the background expectation, following the method described in Ref. [24]. In the tail of the $m_{\tau\tau}$ distribution ($m_{\tau\tau} > 150\,\text{GeV}$), where the sta-

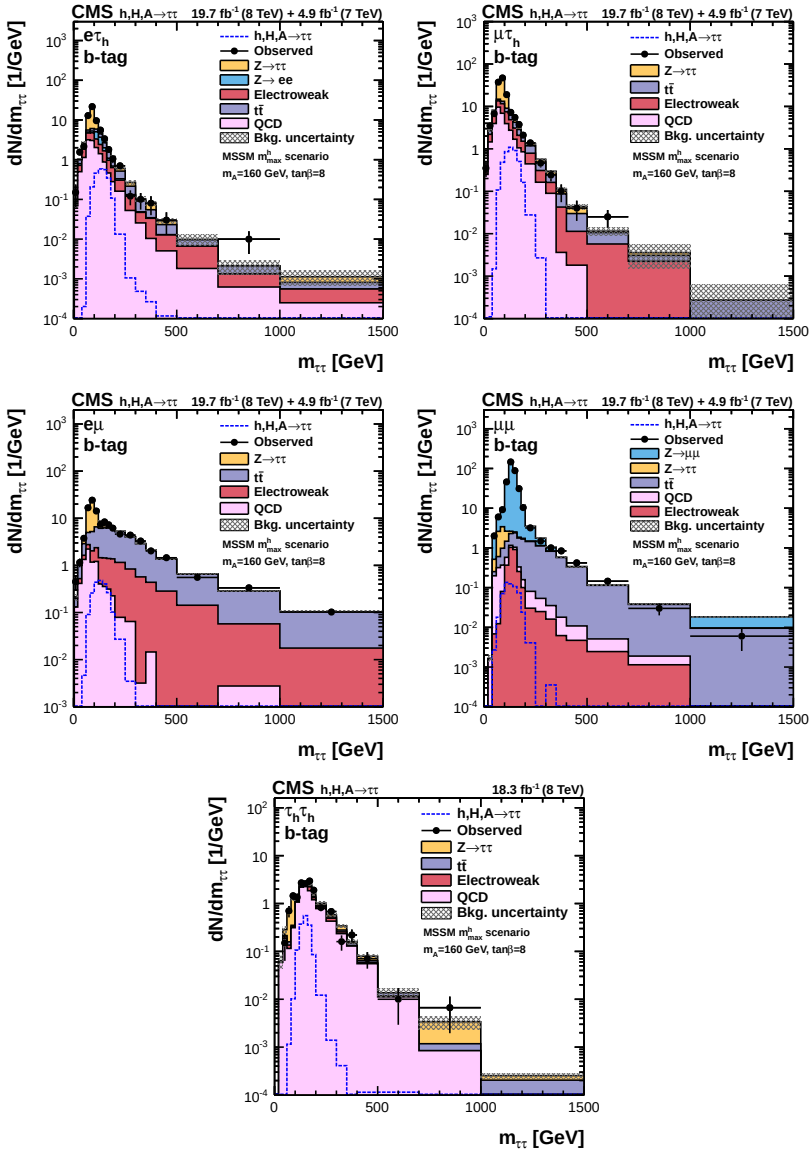

Figure 56: Reconstructed $\tau\tau$ mass in the b-tag category for the $e\tau_h$, $\mu\tau_h$, $e\mu$, $\mu\mu$ and $\tau_h\tau_h$ channels. Other details are as in Fig. 55.

tistical uncertainties are large, a different method is used. A fit of the form $f = \exp[-m_{\tau\tau}/(c_0 + c_1 \cdot m_{\tau\tau})]$ is performed for each of the major backgrounds, the result of which replaces the nominal distribution. The uncertainties in the fit parameters c_0 and c_1 are treated as nuisance parameters in the likelihood fit.

4.4.2 Limit extraction

The invariant-mass spectra show no clear evidence for the presence of a MSSM Higgs boson signal so exclusion limits are obtained. For

Table 16: Systematic uncertainties that affect the estimated number of signal or background events. Several uncertainties are treated as correlated for the different decay channels and event categories. Some uncertainties vary with p_T, η, and final state, so ranges are given.

		Propagation of uncertainty into event categories	
Experimental uncertainties	Uncertainty	no b-tag	b-tag
Integrated luminosity 7 (8)TeV	2.2 (2.6)%	2.2 (2.6)%	2.2 (2.6)%
Jet energy scale	1–10%	1–5%	1–8%
$\not\!\!E_T$	1–5%	1–2%	1–2%
Electron identification and trigger	2%	2%	2%
Muon identification and trigger	2–3%	2–6%	2–6%
Tau-lepton identification and trigger	8%	8–19%	8–19%
b-tagging efficiency	2–7%	2–4%	2–9%
b-mistag rate	10–20%	2%	2–5%
Normalization, Z production	3.3%	3.3%	3.3%
$Z \to$ fifi: category selection	3%	—	1–3%
Normalization, $t\bar{t}$	10%	10%	10–17%
Normalization, di-boson	15–30%	15–30%	15–30%
Normalization, QCD Multijet	10–35%	10–35%	20–35%
Normalization, W+jets	10–30%	10–30%	30%
Normalization, $Z \to ee$: e misidentified as τ_h	20%	20%	20%
Normalization, $Z \to \mu\mu$: μ misidentified as τ_h	30%	30%	30%
Normalization, Z+jets : jet misidentified as τ_h	20%	20%	20%
Electron energy scale	1%	1%	1%
Muon energy scale	1%	1%	1%
Tau-lepton energy scale	3%	3%	3%

the calculation of exclusion limits a modified frequentist criterion CL_s [110, 125] is used. The chosen test statistic q, used to determine how signal- or background-like the data are, is based on a profile likelihood ratio.

In this study, two searches are performed:

- a model independent search for a single narrow resonance ϕ for different mass hypotheses in the gluon fusion and b-quark associated Higgs boson production modes;
- a search for the MSSM neutral Higgs bosons, h, A, and H in the $\tau\tau$ mass spectrum.

In the case of the model independent search for a single resonance ϕ, the profile likelihood ratio is defined as

$$q_\mu = -2 \ln \frac{L\left(N_{obs}|\mu \cdot s + b, \hat{\theta}_\mu\right)}{L\left(N_{obs}|\hat{\mu} \cdot s + b, \hat{\theta}\right)}, \quad \text{with } 0 \leqslant \hat{\mu} \leqslant \mu, \tag{41}$$

where N_{obs} is the number of observed events, b and s are the number of expected background and signal events, μ is the signal strength

modifier, and $\hat{\theta}$ is the nuisance parameter vector describing the systematic uncertainties. The value $\hat{\hat{\theta}}_\mu$ maximizes the likelihood in the numerator for a given μ, while $\hat{\mu}$ and $\hat{\theta}$ define the point at which the likelihood reaches its global maximum. The ratio of probabilities to observe a value of the test statistic at least as large as the one observed in data, q_μ^{obs}, under the signal-plus-background ($\mu \cdot s + b$) and background-only hypotheses,

$$CL_s(\mu) = \frac{P(q_\mu \geqslant q_\mu^{obs} | \mu \cdot s + b)}{P(q_\mu \geqslant q_\mu^{obs} | b)} \leqslant \alpha, \tag{42}$$

is used as the criterion for excluding the presence of a signal at the $1 - \alpha$ confidence level (CL).

Upper limits on $\sigma \cdot \mathcal{B}(\phi \to \tau\tau)$ at 95% CL for gluon fusion and b-quark associated neutral Higgs boson production for a single narrow resonance are obtained using Eqs. 41 and 42. The expected limit is obtained by replacing the observed data by a representative dataset which not only contains the contribution from background processes but also a SM Higgs boson with a mass of 125 GeV. To extract the limit on the gluon fusion (b-quark associated) Higgs boson production, the rate of the b-quark associated (gluon fusion) Higgs boson production is treated as a nuisance parameter in the fit.

A search for MSSM Higgs bosons in the $\tau\tau$ final state is also performed, where the three neutral MSSM Higgs bosons are present in the signal. In light of the recent Higgs boson discovery at 125 GeV, a search for a MSSM signal versus a background-only hypothesis is no more the only hypothesis worth considering. A modified CL_s approach has been also adopted in this case, which tests the compatibility of the data to a signal of the three neutral Higgs bosons h, H, and A compared to a SM Higgs boson hypothesis, with inclusion of the backgrounds in both cases. To achieve this, a physics model is built according to

$$M(\mu) = [\mu \cdot s(\text{MSSM}) + (1 - \mu) \cdot s(\text{SM})] + b. \tag{43}$$

In the search, two well defined theories are tested so μ can only take the value of 0 or 1. The test statistic used in the CL_s method is given by the ratio of likelihoods

$$q_{\text{MSSM/SM}} = -2 \ln \frac{L\left(N_{obs} | M(1), \hat{\theta}_1\right)}{L\left(N_{obs} | M(0), \hat{\theta}_0\right)}, \tag{44}$$

where the numerator and denominator are maximized by finding the corresponding nuisance parameters $\hat{\theta}_1$ for μ=1 and $\hat{\theta}_0$ for μ=0.

The MSSM Higgs boson signal expectation for each benchmark scenario studied is determined in each point of the parameter space as follows:

- At each point of m_A and $\tan\beta$: the mass, the gluon fusion and associated-b production cross sections, and the branching fraction to $\tau\tau$ are determined for h, H and A.

- The contributions of all three neutral Higgs boson are added using the corresponding cross sections times branching fractions.

Limits on $\tan\beta$ versus m_A at 95% CL are obtained for different benchmark MSSM scenarios following the test statistic given in Eq. 44.

4.5 RESULTS

The invariant-mass spectra show no clear evidence for the presence of a MSSM Higgs boson signal. Therefore 95% CL upper bounds on $\tan\beta$ as a function of the pseudoscalar Higgs boson mass m_A are set for the traditional MSSM benchmark scenario m_h^{max}, and the recently proposed benchmark scenarios, m_h^{mod+}, m_h^{mod-}, light-stop, light-stau, and τ-phobic. In the case of the low-m_H scenario, limits on $\tan\beta$ as a function of the higgsino mass parameter μ are performed, where m_A is set to a value of 110 GeV.

A test of the compatibility of the data to a signal of the three neutral Higgs bosons h, H, and A compared to a SM Higgs boson hypothesis is performed as described in Section 4.4, using the test statistics given by Eq. 44. The simulation of the SM Higgs boson signal at 125 GeV used in the statistical analysis, is the same as in the dedicated SM Higgs boson search in the $\tau\tau$ decay mode [45], which includes the contributions from gluon fusion, vector boson fusion, and Z or W boson and top-quark associated Higgs boson production. The contribution from SM b-quark associated Higgs boson production is expected to be small and is not included in this analysis.

Fig. 57 shows the expected and observed exclusion limits at the 95% CL in the m_h^{max} scenario and the modified scenarios m_h^{mod+} and m_h^{mod-}. The allowed regions where the mass of the MSSM scalar Higgs boson h or H is compatible with the mass of the recently discovered boson of 125 GeV within a range of ± 3 GeV are delimited by the hatched areas. Most of the MSSM parameter space is excluded by the Higgs boson mass requirement in the m_h^{max} scenario, while in the modified scenarios the exclusion is mainly concentrated at low $\tan\beta$ values.

Fig. 58 shows the exclusion limits at the 95% CL in the light-stop, light-stau, τ-phobic and low-m_H scenarios. In the light-stop scenario, most of the parameter space probed is excluded either by the direct exclusion of this search or by the Higgs boson mass compatibility requirement with the recent Higgs boson discovery at 125 GeV.

It should be noted that due to the interference effects of the bottom and top loops in the MSSM ggh cross section calculation, the direct search is also able to exclude some regions at low $\tan\beta$.

To allow to compare these results to other extensions of the SM in addition to the MSSM, which have been proposed to solve the hierarchy problem, a search for a single resonance ϕ with a narrow width compared to the experimental resolution is also performed. In this case, model independent limits on the product of the production cross section times branching fraction to $\tau\tau$, $\sigma \cdot \mathcal{B}(\phi \to \tau\tau)$, for gluon fusion and b-quark associated Higgs boson production, as a function of the Higgs boson mass m_ϕ have been determined. To model the

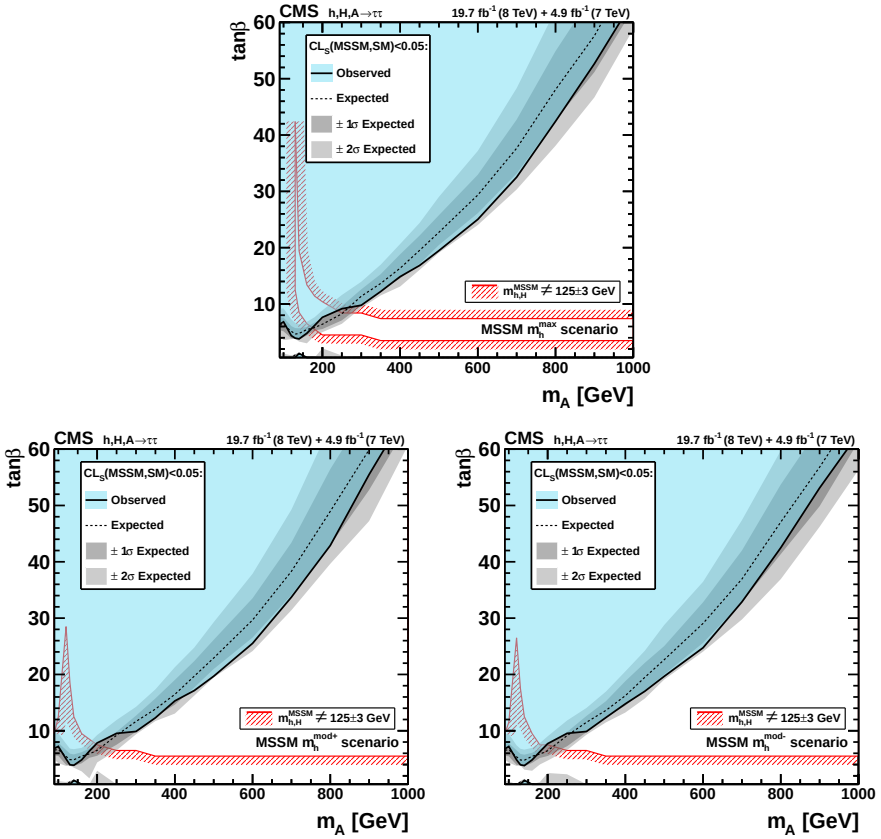

Figure 57: Expected and observed exclusion limits at 95% CL in the m_A-$\tan\beta$ parameter space for the MSSM m_h^{max}, m_h^{mod+} and m_h^{mod-} benchmark scenarios, are shown as shaded areas. The allowed regions where the mass of the MSSM scalar Higgs boson h or H is compatible with the mass of the recently discovered boson of 125 GeV within a range of ± 3 GeV are delimited by the hatched areas. A test of the compatibility of the data to a signal of the three neutral Higgs bosons h, H and A compared to a SM Higgs boson hypothesis is performed.

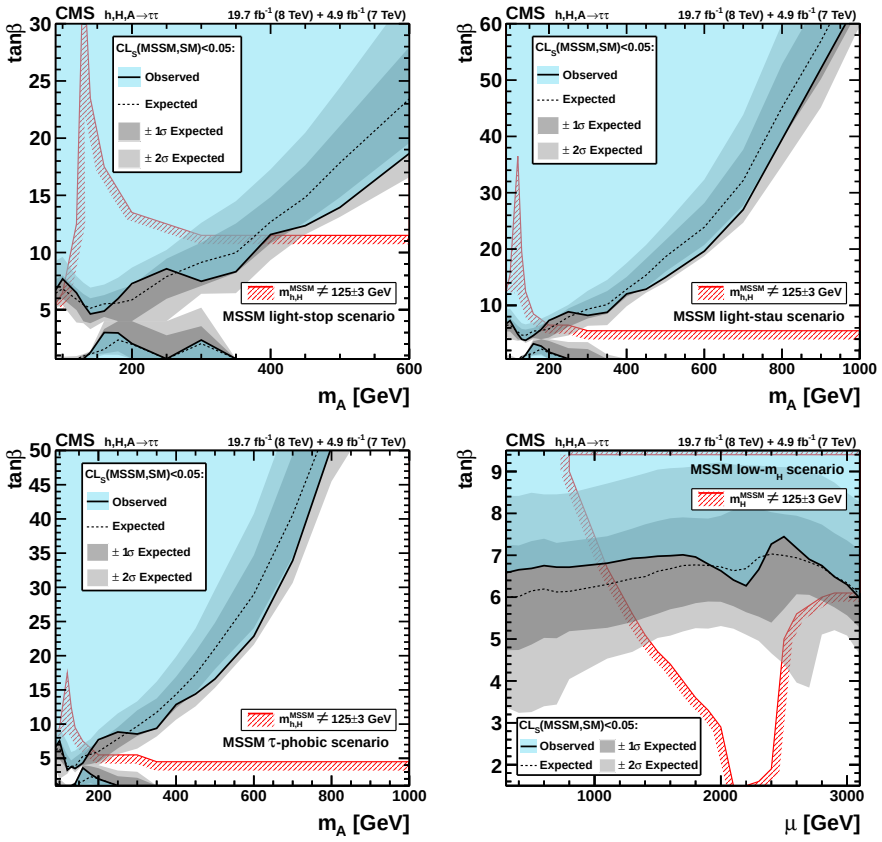

Figure 58: Expected and observed exclusion limits at 95% CL in the m_A-$\tan\beta$ parameter space for the MSSM light-stop, light-stau, and τ-phobic benchmark scenarios. In the MSSM low-m_H benchmark scenario the limits in the μ-$\tan\beta$ parameter space are shown. Other details are as in Fig. 57.

hypothetical signal ϕ, the same simulation samples as the neutral MSSM Higgs boson search have been used. These results have been obtained using the data with 8TeVcenter-of-mass energy only and are shown in Fig. 59. The expected and observed limits are computed using the test statistics given by Eq. 41. To extract the limit on the gluon fusion (b-quark associated) Higgs boson production, the rate of the b-quark associated (gluon fusion) Higgs boson production is treated as a nuisance parameter in the fit. For the expected limits, the observed data have been replaced by a representative dataset which not only contains the contribution from background processes but also a SM Higgs boson with a mass of 125 GeV. The observed limits are in agreement with the expectation.

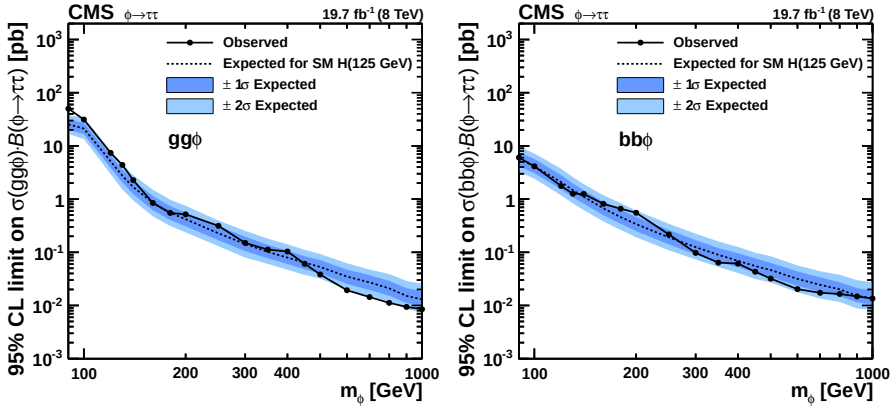

Figure 59: Upper limit at 95% CL on $\sigma(gg\phi)\cdot\mathcal{B}(\phi\to\tau\tau)$ (left) and $\sigma(bb\phi)\cdot\mathcal{B}(\phi\to\tau\tau)$ (right) at 8TeVcenter-of-mass energy as a function of m_ϕ, where ϕ denotes a generic Higgs-like state. The expected and observed limits are computed using the test statistics given by Eq. 41. For the expected limits, the observed data have been replaced by a representative dataset which not only contains the contribution from background processes but also a SM Higgs boson with a mass of 125 GeV.

Finally, a 2-dimensional 68% and 95% CL likelihood scan of the cross section times branching fraction to $\tau\tau$ for gluon fusion and b-quark associated Higgs boson production, $\sigma(bb\phi)\cdot\mathcal{B}(\phi\to\tau\tau)$ versus $\sigma(gg\phi)\cdot\mathcal{B}(\phi\to\tau\tau)$, has also been performed. The results for different values of the Higgs boson mass m_ϕ are shown in Fig. 60. The best fit value and the expectation from a SM Higgs boson with a mass of 125 GeV is also shown. The result from the likelihood scan for $m_\phi = 125$ GeV is compatible with the expectation from a SM Higgs boson.

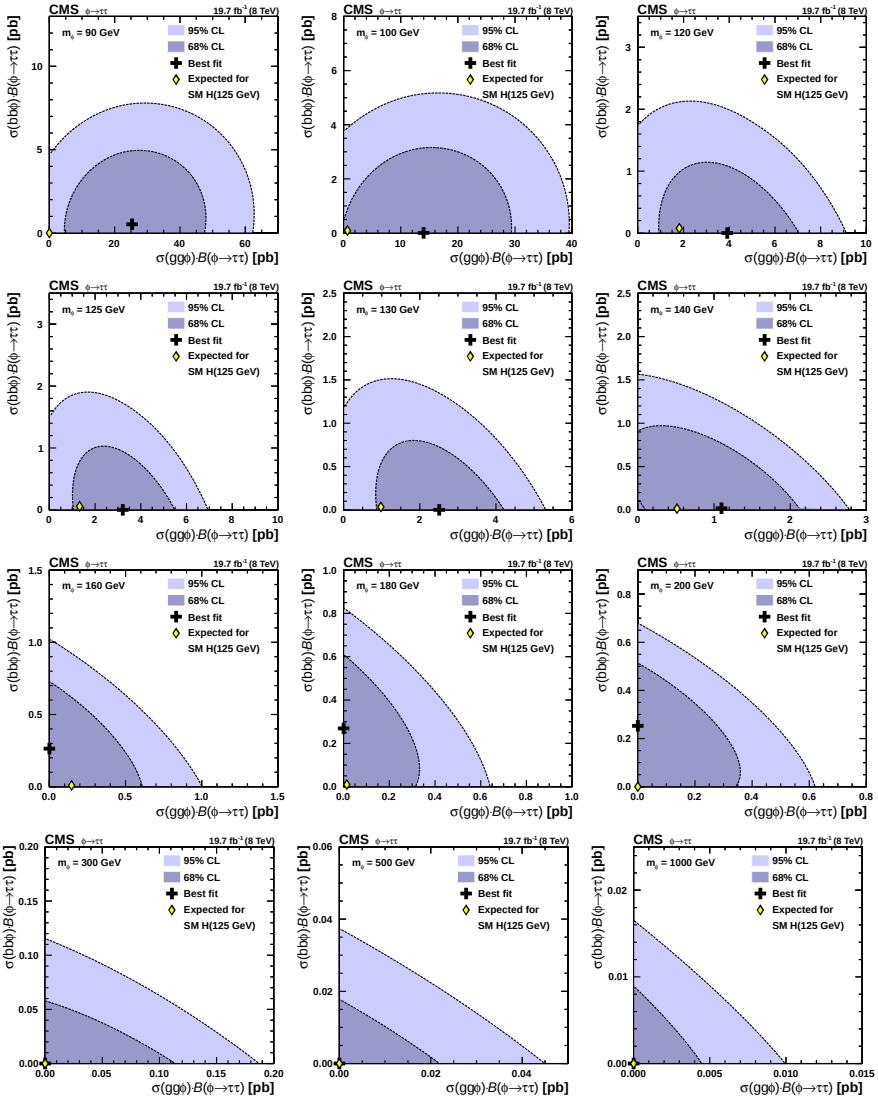

Figure 60: Likelihood contours of $\sigma(bb\phi)\cdot\mathcal{B}(\phi\to\tau\tau)$ versus $\sigma(gg\phi)\cdot\mathcal{B}(\phi\to\tau\tau)$ at 8TeVcenter-of-mass energy for different values of the Higgs boson mass m_ϕ. The best fit value (cross) and the expectation from a SM Higgs boson with a mass of 125 GeV (diamond) is also shown. In the case of m_ϕ = 300, 500 and 1000GeV, the best fit value and the expectation from a SM Higgs boson at 125 GeV are both at (0,0).

5 CONCLUSIONS

The first search for $H \to \tau\tau$ in the fully hadronic final state, using $19.7 fb^{-1}$ of data collected by CMS at $\sqrt{s} = 8\,TeV$, has been performed and presented in this thesis. This work has been an essential part of the general search for a Higgs boson decaying into a pair of tau leptons carried out in the CMS Collaboration.

The search for the Higgs boson has been conducted both in the standard model and in the minimal supersymmetric standard model contexts. In the SM analysis, the gluon–gluon fusion and vector-boson fusion production of a Higgs boson are probed in the one-jet and two-jet final states, respectively, whereas the production of a Higgs boson in association with a W or Z boson decaying leptonically is identified by requiring additional electrons or muons in the final state. The results obtained in the fully hadronic channel have been combined with the ones in the other five di-tau channels, $\mu\tau_h$, $e\tau_h$, $\tau_h\tau_h$, $e\mu$, $\mu\mu$, and ee.

The $\tau_h\tau_h$ channel alone is the second most sensitive after $\mu\tau_h$ at $m_H = 125\,GeV$, excluding at the 95% CL, in the background-only hypothesis, a signal cross section equal to $1.2 * (\sigma_H \times BR(H \to \tau\tau))_{SM}$. A 2 standard deviation excess is observed over the background-only prediction for $m_H = 125\,GeV$.

Combining the six di-tau channels together, an excess of events over the background-only hypothesis is observed with a local significance equal to 3.2 standard deviations at $m_H = 125GeV$, to be compared to an expected significance of 3.7 standard deviations. The best fit of the observed $H \to \tau\tau$ signal cross section times branching fraction for $m_H = 125\,GeV$ is 0.78 ± 0.27 times the standard model expectation. Assuming that this excess corresponds to a Higgs boson decaying to $\tau\tau$, its mass is measured to be $m_H = 122 \pm 7GeV$. These results constitute evidence for the coupling between the τ lepton and the 125 GeV Higgs boson discovered in 2012 by the ATLAS and CMS Collaborations.

In the MSSM analysis, the characteristic b-quark associated Higgs production mode is probed in the events with at least one b–tagged jet whereas the gluon–gluon fusion mode is tested in events with no such jets. As opposed to the SM analysis, the selections have been carefully designed to avoid any model-dependency. No excess is observed in the tau-lepton-pair invariant mass spectrum. Therefore, exclusion limits have been set in the MSSM $\tan\beta$ vs. m_A parameter space for different MSSM benchmark scenarios, m_h^{max}, m_h^{mod+}, m_h^{mod-}, light-stop, light-stau, τ-phobic and low-m_H cross section Model indepen-

dent upper limits on the Higgs boson production cross section times branching fraction for gluon fusion and b–quark associated production have been also extracted.

A | DI-τ_h TRIGGER EFFICIENCY MEASUREMENT

A.1 INTRODUCTION

The measurement of the trigger efficiency is the first critical step in building an analysis. Five out of the six channels encompassed in the Higgs to di-tau search, $\mu\tau_h$, $e\tau_h$, $e\mu$, ee, $\mu\mu$, include at least an electron or a muon in the final state and therefore make use of triggers that rely on the clear signature of a light lepton paired up with an hadronic tau. For these triggers, the Level-1 is based on a single muon or a single electron and the request of an hadronic tau is done at the later HLT stage, where both the calorimeter and tracker contribute to the reconstruction, greatly improving the tau momentum resolution.

In the fully hadronic $\tau_h\tau_h$ channel, the selected events are required to pass the `HLT_DoubleMediumIsoPFTau35_Trk{1,5}_eta2p1` trigger, which is based on the presence, at all levels, starting from the Level-1, of two isolated hadronic tau.

A.2 THE DI-τ_h TRIGGER

The `HLT_DoubleMediumIsoPFTau35_Trk{1,5}_eta2p1` trigger had been deployed for most of 2012 CMS data-taking, covering the B, C and D periods, for and integrated luminosity corresponding to 18.3fb^{-1} out of 19.7fb^{-1} collected in 2012. During period A and at the beginning of period B, the only suitable trigger available online was the `HLT_DoubleMediumIsoPFTau{25,30}_Trk{1,5}_eta2p1_Jet30` trigger [1] This trigger collected an integrated luminosity corresponding to 1.4fb^{-1}.

At Level-1 two jet objects with $p_T > 44$ GeV and $|\eta| < 2.17$ are required. In order to perform a first rough tau identification and rejection of QCD jets, these Level-1 candidate jets are classified as Level-1 tau jets if they satisfy an additional specific requirements on the energy deposit spread and narrowness of the jet cone.

However, for high τ energies, the above requirements introduce an inefficiency for genuine tau leptons. This is recovered by allowing events with two Level-1 jets (central or tau) with $p_T > 64$ GeV and $|\eta| < 3.0$ to be selected. The Level-2 takes the Level-1 jets as a seed and unpacks the full calorimetric information. The transverse momenta of Level-2 objects must exceed 35 GeV. This p_T threshold is lower

1 The latter differs from the former by the requirement of an additional jet with $p_T > 30$ GeV after the Level-1, and by slightly lower p_T thresholds on the taus. The considerations made in this appendix apply to both.

than the one at Level-1; however, the energy calibration applied to Level-1 jets and hence tau-jets is tuned for QCD jets and effectively overestimates the actual tau energy by about 20 GeV.

Then, at Level-2.5, the pixel track isolation is applied on the Level-2 objects to further decrease the event rate. Finally, at Level-3, two PFTaus, reconstructed with a light version of the PF algorithm, with $p_T > 35$ GeV, are required and additional quality cuts on their constituent tracks are applied.

Because of the specific design of this trigger, and because of the lack of a single-tau utility trigger, the standard technique used for the efficiency measurement is not applicable in this case. In fact, a requirement for two hadronic taus or jets is already implemented at Level-1 and, subsequently, at all the trigger levels, which makes it impossible to analyze per-leg efficiency independently using online HLT information of the signal events. Furthermore,there is no an obvious orthogonal dataset with enhanced signal events that can be used to extract the trigger efficiency from data.

A.3 THE TECHNIQUE IMPLEMENTED

The trigger efficiency has been measured in both data and MC samples. The data samples are listed in Sec. 3.2 and, as far as the simulation is concerned, all the SM gluon-gluon fusion Higgs samples at different m_H have been considered together. This reduced the statistical uncertainty on the MC to a negligible level.

The method consists of selecting an unbiassed sample of taus that pass the final selection as described in Sec. **??** and computing the trigger efficiency as the ratio of the number of events in the control sample above that would pass the trigger divided by the size of the control sample itself.

In order to select an unbiassed sample of taus in data, which acts in fact as the denominator, the selection applied is meant to isolate $Z \to \tau_\mu \tau_h$ events without using any tau-related trigger requirement:

- the single muon trigger `HLT_IsoMu24_eta2p1` must be fired;
- a well identified and isolated muon, with $p_T > 24$ GeV and $|\eta| < 2.1$ and matched with the trigger object, is required;
- a tau lepton is required. It must satisfy the following conditions, which are identical to the offline selection: $p_T > 20$ GeV and $|\eta| < 2.1$, medium working point of the delta beta corrected, 3 hits isolation and loose working point of the anti muon discriminator.

Furthermore, additional cuts are applied in order to reduce the contamination from processes other than $Z \to \tau_\mu \tau_h$ and to increase the purity of the sample:

- the invariant, visible mu-tau mass must be lower than 60 GeV to reduce the contamination from $Z \to \mu\mu$ events;
- the transverse mass between the muon and the missing transverse energy must be smaller than 20 GeV to reduce the W + jets background.

A cross check performed using the simulated Z and W samples show that a purity larger than 85% is obtained.

The deployment of the `HLT_DoubleMediumIsoPFTau35_Trk{1,5}_eta2p1` trigger has been accompanied by the introduction of a sibling utility trigger `HLT_IsoMu18_eta2p1_MediumIsoPFTau25_Trk1_eta2p1`. In this trigger, the tau is selected exactly in the same manner as in the di-tau trigger, the only differences being the lower p_T threshold for the Level-2 tau and the absence of the Level-1 tau requirement, whereas the muon is selected as in `HLT_IsoMu24_eta2p1` trigger, apart for a lower p_T cut.

The numerator of the ratio described above is obtained by selecting the events in the control sample that fire the `HLT_IsoMu18_eta2p1_MediumIsoPFTau25_Trk1_eta2p1` trigger. Since the muon leg of this trigger is identical to `HLT_IsoMu24_eta2p1` apart for the p_T cut lowered down to 18 GeV all the muons that fire the `HLT_IsoMu24_eta2p1` trigger can fire the `HLT_IsoMu18_eta2p1_MediumIsoPFTau25_Trk1_eta2p1` trigger as well, thus the efficiency on the muon part is equal one and can be factorised out.

Two more effects need to be taken into account in order to complete the efficiency measurement: the different p_T threshold at Level-2, 25 instead of 35 GeV, and the efficiency of the Level-1 trigger.

To rectify these differences, the p_T threshold on the Level-2 τ objects is increased manually at 35 GeV and the selected events must have, in addition, either a matching Level-1 tau with $p_T > 44$ GeV and $|\eta| < 2.1$ or a matching Level-1 jet with $p_T > 64$ GeV and $|\eta| < 3.0$

Exactly the same procedure is applied for both data and MC. The efficiency curves as a function of the tau p_T are obtained analytically by fitting the ratio distribution here derived. The derivation of these functions is described in the following Sec. A.4.

A.4 THE CHOICE OF THE FIT FUNCTION

Ideally, the curve describing the trigger effect in dependence of p_T is the Heaviside step function centered at the p_T cut value, p_T^{cut}:

$$\Theta(p_T) = \begin{cases} 0 & \text{if } p_T < p_T^{cut} \\ \alpha & \text{if } p_T > p_T^{cut} \end{cases}$$

However, experimentally, the transverse momentum resolution is finite and described by an approximately gaussian probability distribution function. In particular, at the trigger level, the need to have a fast reconstruction, has a non negligible impact on the precision of the momentum measurement. As a result, the application of a threshold at a certain p_T value is not equivalent to a sharp cut: events with a p_T lower than the threshold have however a non-null probability to pass the trigger selection, as well as events with a p_T greater than the threshold could not fire the trigger bit. The probability is higher near the value of the p_T cut and then goes to zero, so the effect of the measurement uncertainty at transverse momentum away from the threshold is negligible. The net effect is the smearing of the step function by the function that describe the resolution of the trigger. It is achieved by the convolution of the two curves and results in a function with an inflection point in correspondence of the p_T threshold of the trigger. This function is referred to as Error Function.

The trigger under study presents different p_T thresholds applied at different levels. Each one brings a specific resolution function centered at a different p_T value and at the end of the Level-3 selection these effects are merged all together. It is difficult to find a unique parametrization which is able to describe in a good manner the trigger efficiency over the whole p_T range.

Then, the first step of this study consists of the analysis of the Level-2 and Level-3 resolutions. The L1 is not considered because, due to is shifted p_T value reconstruction, its turn on grows and reaches the plateau when the other two contribution start to increase. So, the Level-1 resolution does not affect the final trigger efficiency.

In Figures 61a and 61b are reported the event per event resolutions for L2 and L3 respectively, computed as pulls:

$$\frac{p_T^{\tau off} - p_T^{\tau HLT}}{p_T^{\tau off}} \tag{45}$$

where $p_T^{\tau off}$ stays for the τ p_T measured offline and $p_T^{\tau HLT}$ is the value of the τ p_T calculated by the HLT. According to this definition the resolutions are expected to be distributed as a Gaussian centered in zero. At a first glance, the shapes of the two distributions are similar to a Gaussian function, but differ from it because are distorted on their sides and asymmetric. This means that in the HLT the p_T measurement is underestimated with respect to the offline evaluation. In fact, in the HLT some tracks can be lost leading to a τ with lower p_T, while the offline PF algorithm can recover their information with

sophisticated algorithms. The same reason underlies the shift of the distribution center towards negative values: the effect is negligible in the L3 resolution because at this level intervenes the superior reconstruction of a PF-type techniques.

In fact, the function that better fit the Level-2 resolution is a right-sided Crystal Ball: it consists of a Gaussian core portion and a power-law low-end tail on the right side, below a certain threshold. It is given by:

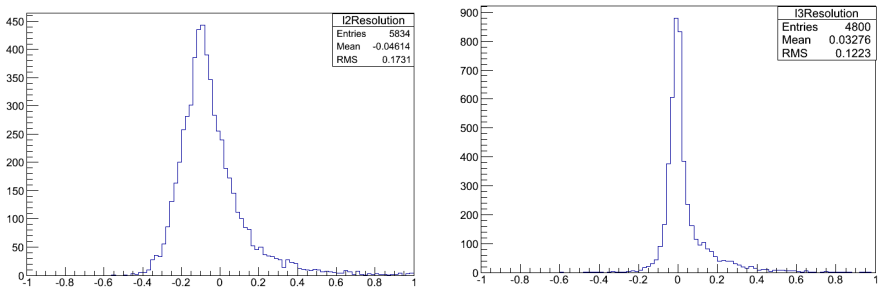

(a) Level-2 resolution. **(b)** Level-3 Resolution.

Figure 61: The trigger p_T resolutions at (a) L2 and (b) L3 for the full dataset.

$$\mathrm{CrystalBall}(x; x_0, \sigma, \alpha, n) = N \cdot \begin{cases} e^{-t^2/2} & \text{if } t < \alpha \\ a \cdot (b + t)^{-n} & \text{if } t \geqslant \alpha \end{cases}$$

where N is the common normalization parameter and t, a and b are defined in the following way:

$$t = \frac{x - x_0}{\sigma} \qquad a = \left(\frac{n}{|\alpha|}\right)^n e^{-|\alpha|^2/2} \qquad b = \frac{n}{|\alpha|} - |\alpha| \tag{46}$$

x_0 and σ are the mean and the variance parameter of the Gaussian core, α indicates the number of standard deviation from the mean at which starts the tail and n is the power of the tail.

As for the Level-3 p_T resolution, the distribution is too peaked and the simple one-sided Crystal Ball cannot describe well its shape. The solution consists of an asymmetric function, that can be optimized indipendently for each sides: the choice of the fit function falls on the Double Sided Crystal Ball. The curve has a Gaussian core and a power-law tail on both sides:

$$\mathrm{DoubleCrystalBall}(x; x_0, \sigma, \alpha, \beta, n_\alpha, n_\beta) = N \cdot \begin{cases} a_\beta \cdot (b_\beta - t)^{-n_\beta} & \text{if } t \leqslant -\beta \\ e^{-t^2/2} & \text{if } -\beta < t < \alpha \\ a_\alpha \cdot (b_\alpha + t)^{-n_\alpha} & \text{if } t \geqslant \alpha \end{cases}$$

where t is defined as above, a_α and b_α are the same as a and b in the Crystal Ball, a_β and b_β are also equal to them, except for the replacement of α and n_α with β and n_β. These parameters have the same role as above: α, n_α, β and n_β represent the number of standard deviation from which the tail starts and the power of the tail for the right and the left side, respectively.

The distributions with the fit functions are shown in Figures 62a and 62b, while the parameters obtained from the fit procedure are reported in Tab. 17.

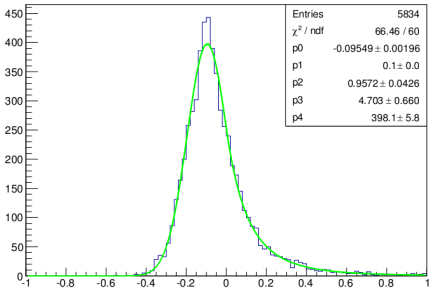

(a) The fit of the Level-2 p_T resolution.

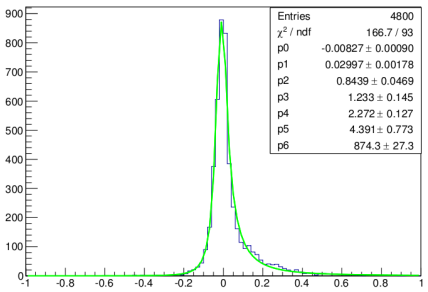

(b) The fit of the Level-3 p_T resolution.

Figure 62: The trigger p_T resolutions at (a) L2 and (b) L3 fitted with a Right Sided Crystal Ball and a Double Sided Crystal Ball, respectively.

Level	Fit parameters						
	N	x_0	σ	α	n_α	β	n_β
L2	398±6	-0.095±0.002	0.102±0.002	0.96±0.04	4.7±0.7		
L3	874±27	-0.008±0.001	0.029±0.002	0.84±0.05	2.3±0.1	1.2±0.1	4.4±0.8

Table 17: The parameters obtained from the fit of the L2 and L3 p_T resolutions.

From the resulting fit parameters it can be inferred that the Level-2 p_T resolution is worse than the Level-3 p_T resolution. This feature implies that the L2 p_T resolution dominates in the total trigger p_T resolution: the trigger efficiency culd be fitted with a convolution of a right-sided Crystal Ball and a Heaviside step function. The fact that the Crystal Ball has a tail on the right side makes the convoluted curve increase with the p_T, until the right-side tail is extinguished. However, this is an effect which is not observed experimentally: the trigger efficiency after a certain p_T value reaches a plateau and remains quite stable. In fact, there are other elements, such as the cuts applied on the track quality, which attenuate the tendency of the p_T resolution to grow indefinitely: the net effect is the lowering of the trigger efficiency at high p_T and the achievement of a stable plateau. The attempt to fit the trigger efficiency with the convolution of the step function and the Crystal Ball ends up to an unstable fit. In fact, when the fit converges, the value of the parameters describing the

tail of the Crystal Ball, α and n, are very high and affected by a large error. This implies that the tail starts very far from the mean of the curve and its slope is tiny: the fit returns a negligible non-gaussian tail for the Crystal Ball, which tends to become a Gaussian function. In Fig. 63 is reported the comparison between the fit of the efficiency with the Crystal Ball (in green) and the Gaussian (in red) parametrization for the p_T resolution: from the plot it can be inferred that the difference of the two curves is tiny. Moreover, the large α and n uncertainties mean that it is very hard to constrict these parameters. In conclusion, it can be stated that the fit prefers a simple Gaussian as resolution function.

As a result, in order to have a more stable and robust fit, the trigger efficiency is described by the convolution of the Heaviside step function and the Gaussian curve. The function obtained is the cumulative distribution function:

$$\Phi(x) = \frac{\varepsilon}{2}\left[1 + \mathrm{erf}\left(\frac{x - x_0}{\sqrt{2}\sigma}\right)\right] \tag{47}$$

where erf, the error function, is defined as:

$$\mathrm{erf}(x) = \frac{2}{\sqrt{\pi}}\int_0^x e^{-t^2}dt \tag{48}$$

ε is the normalization, x_0 and σ are the Gaussian mean and width parameters. They are the three fit parameters and represent the plateau efficiency, the p_T value correspondent to the inflection point and the spread of the resolution function.

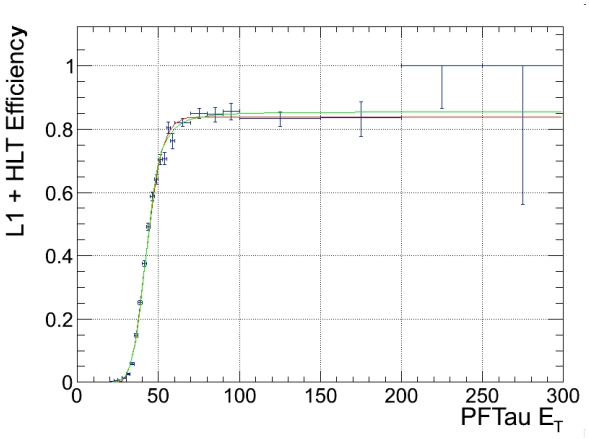

Figure 63: The comparison of the fit curves given by the convolution of the step function with the Crystal Ball (in green) and the Gaussian (in red) is reported. The efficiency is measured for the dataset considered.

A.5 THE FIT PROCEDURE

Once the fit function has been identified, other issues need to be addressed to optimize the fit result. The unbinned maximum likelihood method has been chosen to perform the fits in the followings. A set of N measured quantities $\vec{x} = (x_1,...,x_N)$ is considered. They are statistically independent and each one follows the probability density function $f(x_i;\vec{\theta})$, where $\vec{\theta} = (\theta_1,...,\theta_N)$ is the set of N parameters whose values are unknown. The likelihood function is given by the joint p.d.f. $f(\vec{x};\vec{\theta})$, which is obtained by the factorization of the single p.d.f., evaluated with the data $\vec{x}$ and viewed as a function of the parameters $\vec{\theta}$:

$$\mathcal{L}(\vec{\theta}) = \prod_{i=1}^{N} f(x_i;\vec{\theta}) \tag{49}$$

The method of maximum likelihood takes the estimators $\hat{\theta}$ to be those values of $\vec{\theta}$ that maximize $\mathcal{L}(\vec{\theta})$. It is usual to work with $\ln\mathcal{L}$: the logarithm is an increasing function and $\ln\mathcal{L}$ is maximized by the same parameter values that maximize the $\mathcal{L}$ function. Moreover, it is easier and useful in terms of CPU usage: the joint p.d.f. becomes the sum of the singular p.d.f. and the best parameter values can be found by solving the likelihood equations:

$$\frac{\partial \ln\mathcal{L}}{\partial\theta_i} = 0 \tag{50}$$

In the case considered, the p.d.f's are the cumulative distribution functions $\Phi(x)$ and the parameters θ_i are ϵ, x_0 and σ.

The choice to keep the data unbinned is due to many reasons. The binning could result in a loss of information, specially for the delicate region at low p_T and for the inflection point, and hence larger statistical errors for the parameters estimates. In addition,the probability for each point to fall in the bin is taken into account. Moreover, the analysis would become very complex due to the critical search for the best binning choice to apply. The unbinned maximum likelihood method prevents such problems to occur.

However, using these settings to perform the fit, an important feature has emerged: the parameters returned by the fit depend on the choice of the starting point of the fit. The points considered are 20, 25, 30 e 35 GeV: the lower threshold is imposed by the tau p_T cut at 20 GeV, while the higher one is given by the necessity to describe well the trigger efficiency also near 45 GeV, which is the offline cut on the τ p_T in the analysis. The different fit functions are displayed with various colours in Fig. 64 for the data and Monte Carlo sample and for different $|\eta|$ regions.

Analyzing the fit results reported in Tab. 18 some considerations can be made: the dependence consists of the increase of the efficiency

plateau and of the p_T resolution spread but in the decrease of the inflection point value with the use of lower starting point values. This can be assigned to the fact that considering more points the fit realizes well the enlargment of the curve due to the resolution and, consequently, estimates better the turning point of the efficiency measurement. This leads to a higer value for the x_0 parameter; the fit function become flat from high p_T values and the plateau is evaluated in a not fully corrected manner. Otherwise, reducing the number of points considered in the fit, the first part of the resulting curve does not describe satisfactory the efficiency, but then the fit recovers relibility and returns an acceptable value for the efficiency plateau.

As can be inferred from the plot and the table the effect of the dependence of the parameters on the starting point is more evident in data, while in Monte carlo sample is negligible. In addition, the effect occurs mainly at high $|\eta|$ values: the greater deviation in the fit curves can be noticed for the region of $|\eta| > 1.6$. The explanation lies in the poor statistic of the sample: only the 25% of data are contained in this $|\eta|$ region. Then, each point is affected by a larger uncertainty that makes the fit paramaters to vary consistently in function of the number of points considered. Due to the splitting of data in the $|\eta|$ regions as described before, it can be understand that the trend in the sample with the η merged and considered indistinctly is dominated by the behaviour of data in $|\eta| < 1.4$.

For the Monte Carlo sample, because all the parameter values of different curves are in agreement within their errors, the function used as a measurement of the trigger efficiency is the one which has the best χ^2. The curve with the starting point at 30 GeV is a good compromise in all the $|\eta|$ regions considered and describes better the efficiency points.

Instead, for the data sample, the parameters correspondent at different fit functions are not compatible with each other. Then, there is the need to establish a method to find a satisfactory description of the trigger efficiency. The choice of the curve associated at the best χ^2, which is the one with the starting point at 35 GeV, is not appropriate: this would mean neglecting the functions distant and not consistent with it and loosing the information carried by the curve at low p_T, with starting point at 20 GeV. The right approach is to use the various fit functions to evaluate the systematic uncertainty on the trigger efficiency measurement.

First of all, it might be defined the uncertainty corresponding to each function. In fact, is not correct to compare two curves by regarding at the one σ displacement of its parmeter values: the fit procedure makes the paratameters to be correlated between them and the error which returns is the total variance associated at that value. The uncertainty on the fit function is not gathered from this total error but it is evaluated exploiting the full covariant matrix, which is also pro-

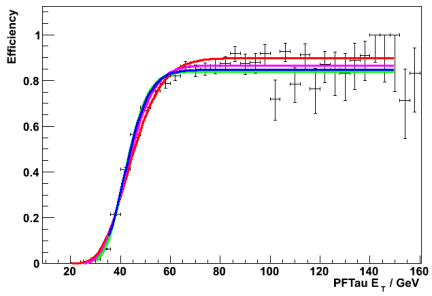

(a) The fit functions of the trigger efficiency for data in the region $|\eta| < 1.4$.

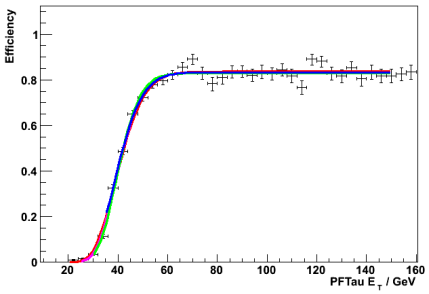

(b) The fit functions of the trigger efficiency for MC in the region $|\eta| < 1.4$.

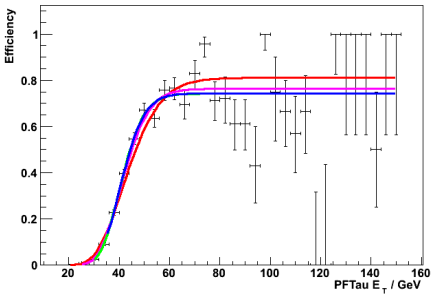

(c) The fit functions of the trigger efficiency for data in the region $|\eta| > 1.6$.

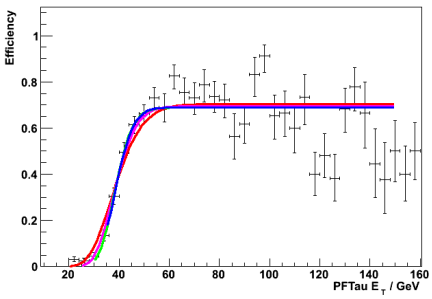

(d) The fit functions of the trigger efficiency for MC in the region $|\eta| > 1.6$.

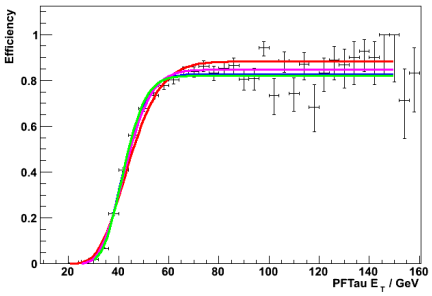

(e) The fit functions of the trigger efficiency for data for all the $|\eta|$ values.

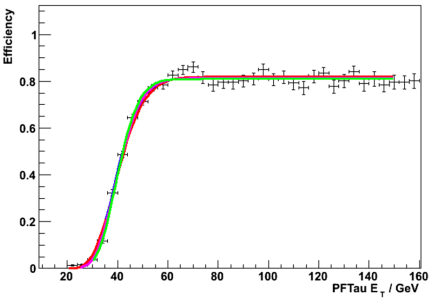

(f) The fit functions of the trigger efficiency for MC for all the $|\eta|$ values.

Figure 64: The functions returned by the fit for different starting points: 20 GeV in red, 25 GeV in pink, 30 GeV in green and 35 GeV in blue. The efficiency is measured for data in (a), (c) and (e), and for Monte Carlo in (b), (d) and (f). The η region considered are: $|\eta| < 1.4$ in (a) and (b), $|\eta| > 1.6$ in (c) and (d), and all the possible η value considered indistinctly in (e) and (f).

vided by the fit procedure. The covariant matrix has on the diagonal elements the variance of the parameters and in the off-diagonal positions the covariance between them. The matrix is symmetric: it could be diagonalized and its eigenvalues and eigenvectors can be find. The linear combinations of the eigenvectors with the coefficients given by the eigenvalues represent a set of three new states. The variation of these states allows for the estimation of the fit function uncertainty. It is achieved by modifying the entire set of the three fit parameters by

η	Sample	Starting	Fit parameters			
		point	χ^2	ε	x_0	σ
< 1.4	data	20 GeV	0.28	0.898±0.007	44.3±0.2	1.02±0.01
		25 GeV	0.48	0.866±0.008	43.1±0.2	0.86±0.01
		30 GeV	0.76	0.839±0.008	42.3±0.2	0.73±0.01
		35 GeV	1.09	0.846±0.009	42.4±0.2	0.78±0.02
	MC	20 GeV	0.82	0.837±0.005	40.5±0.2	0.88±0.02
		25 GeV	0.90	0.832±0.005	40.4±0.2	0.80±0.02
		30 GeV	0.99	0.829±0.006	40.4±0.2	0.74±0.03
		35 GeV	1.07	0.833±0.006	40.1±0.2	0.86±0.04
> 1.6	data	20 GeV	0.28	0.81±0.02	43.6±0.4	1.09±0.03
		25 GeV	0.50	0.76±0.02	41.8±0.4	0.86±0.03
		30 GeV	0.83	0.74±0.02	41.2±0.4	0.75±0.03
		35 GeV	1.16	0.74±0.02	41.2±0.4	0.79±0.06
	MC	20 GeV	0.94	0.70±0.02	38.7±0.6	0.95±0.06
		25 GeV	1.01	0.69±0.02	38.6±0.5	0.74±0.05
		30 GeV	1.14	0.69±0.02	38.7±0.5	0.61±0.06
		35 GeV	1.26	0.69±0.02	38.8±0.5	0.61±0.09
all	data	20 GeV	0.28	0.883±0.007	44.2±0.2	1.04±0.01
		25 GeV	1.48	0.847±0.007	43.5±0.2	0.86±0.01
		30 GeV	0.78	0.820±0.008	42.1±0.2	0.74±0.01
		35 GeV	1.11	0.827±0.009	42.2±0.2	0.78±0.02
	MC	20 GeV	0.84	0.819±0.005	40.3±0.2	0.90±0.02
		25 GeV	0.92	0.814±0.005	40.2±0.2	0.79±0.02
		30 GeV	1.02	0.810±0.005	40.2±0.2	0.72±0.02
		35 GeV	1.10	0.814±0.005	29.9±0.2	0.82±0.04

Table 18: The parameters returned from the fit for all the different starting points, both in data and in MC samples and for the region $|\eta| < 1.4$, $|\eta| > 1.6$ and all the possible η values considered indistinclty.

adding or subtracting the values of the new state vector elements. In this manner the fit parameter errors are computed according to their correlations. The variation up and down of the parameter values for each of the three new states leads to obtain six fit functions. The envelope of these curves gives the errors associated to the fit functions. It is calculated by defining, point by point, the maximum and the minimum between the values assumed by the six fit curves.

This method is applied to the fit functions with 20 and 35 GeV as starting points. The decision has been taken in order to exploit all the possible information from the low p_T region and to remain consistent in the measurement of the trigger efficiency. In fact, the two curves are the more distant and different ones and in this manner the

understimation of the systematic uncertainty on the trigger efficiency is prevented. The result is illustrated in Figures 65a, 65c and 65e for the different η regions. The red and blue lines are the six fit function correspondent to 20 and 35 GeV as starting point, respectively. The black lines represent the envelope of the curves for each starting point. Once the error associated at each fit function is estimated in the correct way, it can be stated that the two curves returned by the fit procedure are not compatibile.

Then, the final step is the identification of the trigger efficiency and of its uncertainty. For this purpose, it can be created a total envelope starting from the two previous envelopes: it is obtained by taken for each point the maximum and minimum value between the four curves. The resulting total envelope constitutes the uncertainty of the trigger efficiency measurement. It is connected to the method implemented to find it, which takes into account the dependence of the fit functions on the fit starting points. The measurement of the trigger efficiency in function of the tau p_T is achieved by taking the central value of this total envelope. The result is a function which is defined point by point. It is represented by the solid lines for the three $|\eta|$ regions in the plots in Figures 65b, 65d and 65f.

The values assumed by the trigger efficiency at the plateau, at high p_T, are $(87\pm3)\%$ in the region $|\eta| < 1.4$, $(77\pm5)\%$ in the region $|\eta| > 1.6$ and $(85\pm3)\%$ when all the η values are considered indistinctly. As expected, the error on the measurement for the high η values is greater due to the low statistics, while the values obtained in the region $|\eta| < 1.4$ and mearging all the η values are very similar. In addition, all the results are in agreement. The measurement performed represent the best estimate for the trigger efficiency, considering all the effects which compare in the study and the strategies adopted to take them into account in the achiving of the final result.

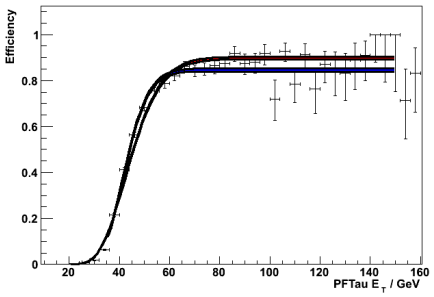

(a) The method of the envelope for data in the region $|\eta| < 1.4$.

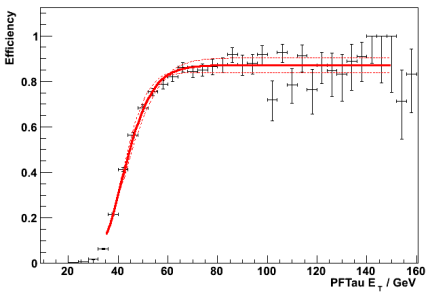

(b) The final fit function of the trigger efficiency for data in the region $|\eta| < 1.4$.

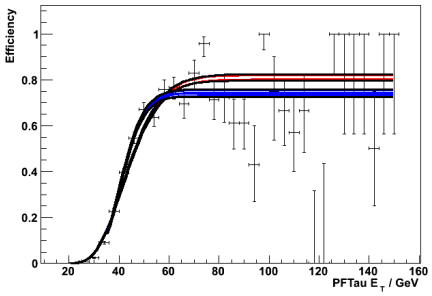

(c) The method of the envelope for data in the region $|\eta| > 1.6$.

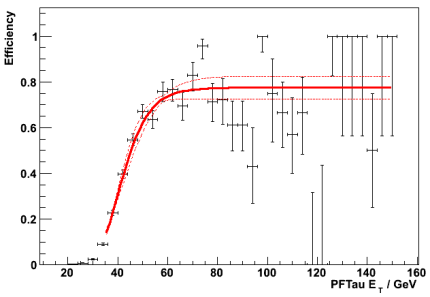

(d) The final fit function of the trigger efficiency for data in the region $|\eta| > 1.6$.

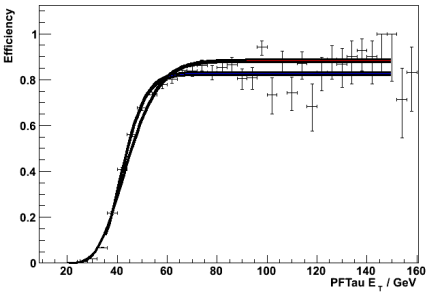

(e) The method of the envelope for data for all the $|\eta|$ values.

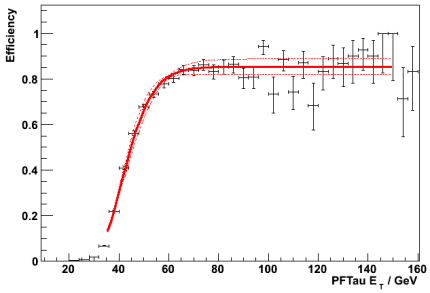

(f) The final fit function of the trigger efficiency for data for all the $|\eta|$ values.

Figure 65: In (a), (c) and (e) for starting point 20 GeV (in red) and 35 GeV (in blue) six functions are obtained by varying the parameters according to their correlations. The black lines are the envelope of the six curves for each starting point. In (b), (d) and (f) the dashed red lines are the total envelope and the solid line is the central value of the envelope. The efficiency is measured for data in all the plots. The η region considered are: $|\eta| < 1.4$ in (a) and (b), $|\eta| > 1.6$ in (c) and (d), and all the possible η value considered indistinctly in (e) and (f).

B FINAL EVENT YIELDS IN THE SM ANALYSIS

Event category	SM Higgs ($m_H = 125\,GeV$) ggH	VBF	VH	Σ signal	Background	Data	$\frac{S}{S+B}$	σ_{eff} (GeV)
$\mu\tau_h$								
0-jet low-$p_T^{\tau_h}$ 7 TeV	23.1	0.2	0.1	23.5 ± 3.4	11950 ± 590	11959	0.002	17.4
0-jet low-$p_T^{\tau_h}$ 8 TeV	83.0	0.8	0.4	85.0 ± 11.0	40800 ± 1900	40353	0.003	16.3
0-jet high-$p_T^{\tau_h}$ 7 TeV	17.5	0.2	0.2	17.9 ± 2.6	1595 ± 83	1594	0.022	15.1
0-jet high-$p_T^{\tau_h}$ 8 TeV	66.2	0.7	0.6	67.5 ± 9.3	5990 ± 250	5789	0.020	15.2
1-jet low-$p_T^{\tau_h}$ 7 TeV	9.1	1.6	0.8	11.5 ± 1.7	2020 ± 120	2047	0.012	18.8
1-jet low-$p_T^{\tau_h}$ 8 TeV	36.0	6.0	3.0	45.0 ± 6.0	9030 ± 360	9010	0.010	18.6
1-jet high-$p_T^{\tau_h}$ 7 TeV	7.7	1.1	0.6	9.4 ± 1.3	796 ± 39	817	0.033	19.1
1-jet high-$p_T^{\tau_h}$ 8 TeV	29.6	4.3	2.4	36.3 ± 4.6	3180 ± 130	3160	0.029	19.7
1-jet high-$p_T^{\tau_h}$ boosted 7 TeV	2.6	0.8	0.5	3.9 ± 0.6	282 ± 16	269	0.054	17.7
1-jet high-$p_T^{\tau_h}$ boosted 8 TeV	11.5	2.9	2.0	16.5 ± 2.6	1265 ± 62	1253	0.072	17.2
VBF tag 7 TeV	0.2	1.3	–	1.6 ± 0.1	22 ± 2	23	0.14	19.6
Loose VBF tag 8 TeV	1.1	3.4	–	4.5 ± 0.4	81 ± 7	76	0.17	17.0
Tight VBF tag 8 TeV	0.3	2.0	–	2.4 ± 0.2	15 ± 2	20	0.49	18.1
$e\tau_h$								
0-jet low-$p_T^{\tau_h}$ 7 TeV	11.8	0.1	0.1	12.0 ± 1.8	6140 ± 320	6238	0.002	16.4
0-jet low-$p_T^{\tau_h}$ 8 TeV	33.4	0.3	0.2	34.0 ± 4.6	16750 ± 750	17109	0.002	15.8
0-jet high-$p_T^{\tau_h}$ 7 TeV	11.1	0.1	0.1	11.3 ± 1.7	1159 ± 62	1191	0.015	14.3
0-jet high-$p_T^{\tau_h}$ 8 TeV	31.4	0.3	0.3	32.1 ± 4.4	4380 ± 170	4536	0.010	15.4
1-jet low-$p_T^{\tau_h}$ 7 TeV	3.1	0.6	0.3	4.0 ± 0.6	366 ± 25	385	0.029	19.6
1-jet low-$p_T^{\tau_h}$ 8 TeV	9.1	1.8	1.0	11.9 ± 1.6	1200 ± 56	1214	0.025	16.5
1-jet high-$p_T^{\tau_h}$ boosted 7 TeV	1.2	0.3	0.2	1.8 ± 0.3	150 ± 9	167	0.089	15.5
1-jet high-$p_T^{\tau_h}$ boosted 8 TeV	5.1	1.4	0.9	7.5 ± 1.1	497 ± 27	476	0.11	15.5
VBF tag 7 TeV	0.2	0.7	–	0.9 ± 0.1	14 ± 2	13	0.24	15.9
Loose VBF tag 8 TeV	0.6	1.8	–	2.4 ± 0.2	45 ± 4	40	0.14	16.7
Tight VBF tag 8 TeV	0.3	1.3	–	1.6 ± 0.1	9 ± 2	7	0.51	16.2
$\tau_h\tau_h$								
1-jet boosted 8 TeV	7.2	2.1	1.0	10.3 ± 1.7	1133 ± 49	1120	0.054	15.2
1-jet highly-boosted 8 TeV	5.6	1.6	1.2	8.4 ± 1.2	380 ± 23	366	0.14	13.1
VBF tag 8 TeV	0.5	2.4	–	3.0 ± 0.3	29 ± 4	34	0.32	14.3
$e\mu$								
0-jet low-p_T^{μ} 7 TeV	20.8	0.2	0.2	21.1 ± 3.0	11320 ± 260	11283	0.002	24.4
0-jet low-p_T^{μ} 8 TeV	70.3	0.7	0.7	71.7 ± 9.6	40410 ± 830	40381	0.002	23.6
0-jet high-p_T^{μ} 7 TeV	7.5	0.1	0.1	7.8 ± 1.1	1636 ± 55	1676	0.007	22.7
0-jet high-p_T^{μ} 8 TeV	24.0	0.2	0.5	24.7 ± 3.3	6000 ± 150	6095	0.006	20.7
1-jet low-p_T^{μ} 7 TeV	9.0	1.6	1.0	11.7 ± 1.5	2475 ± 74	2482	0.009	23.7
1-jet low-p_T^{μ} 8 TeV	40.6	6.5	3.7	50.8 ± 6.1	10910 ± 250	10926	0.007	23.8
1-jet high-p_T^{μ} 7 TeV	4.7	1.0	0.6	6.2 ± 0.8	928 ± 37	901	0.015	23.3
1-jet high-p_T^{μ} 8 TeV	18.0	3.4	2.6	23.9 ± 2.9	4040 ± 110	4050	0.014	23.1
Loose VBF tag 7 TeV	0.2	1.0	–	1.2 ± 0.1	19 ± 1	12	0.13	23.0
Loose VBF tag 8 TeV	0.6	2.6	–	3.3 ± 0.3	99 ± 6	112	0.054	23.5
Tight VBF tag 8 TeV	0.2	1.5	–	1.6 ± 0.1	14 ± 1	17	0.31	17.8

Table 19: Observed and predicted event yields in all event categories of the $\mu\tau_h$, $e\tau_h$, $\tau_h\tau_h$, and $e\mu$ channels in the full $m_{\tau\tau}$mass range. The event yields of the predicted background distributions correspond to the result of the global fit. The signal yields, on the other hand, are normalized to the standard model prediction. The different signal processes are labelled as ggH (gluon-gluon fusion), VH (production in association with a W or Z boson), and VBF (vector-boson fusion). The $\frac{S}{S+B}$ variable denotes the ratio of the signal and the signal-plus-background yields in the central $m_{\tau\tau}$ range containing 68% of the signal events for $m_H = 125\,GeV$. The σ_{eff} variable denotes the standard deviation of the $m_{\tau\tau}$ distribution for corresponding signal events.

Event category	SM Higgs ($m_H = 125\,GeV$) ggH	VBF	VH	Σ signal	Background	Data
μμ						
0-jet low-p_T^μ 7 TeV	8.0	0.1	0.1	8.2 ± 1.2	266200 ± 1400	266365
0-jet low-p_T^μ 8 TeV	25.4	0.3	0.6	26.4 ± 3.8	873200 ± 2600	873709
0-jet high-p_T^μ 7 TeV	5.5	0.1	0.3	5.9 ± 0.8	982900 ± 2100	982442
0-jet high-p_T^μ 8 TeV	30.6	0.4	3.5	34.6 ± 4.6	3775700 ± 3100	3776365
1-jet low-p_T^μ 7 TeV	2.5	0.4	0.3	3.2 ± 0.4	18680 ± 180	18757
1-jet low-p_T^μ 8 TeV	7.0	1.0	0.6	8.6 ± 1.1	40900 ± 360	40606
1-jet high-p_T^μ 7 TeV	3.7	1.4	1.9	7.0 ± 0.6	233600 ± 1200	234390
1-jet high-p_T^μ 8 TeV	15.1	2.2	4.4	21.7 ± 2.3	646000 ± 2500	646549
2-jet 7 TeV	1.4	0.2	0.7	2.4 ± 0.3	33260 ± 350	33186
2-jet 8 TeV	6.3	3.9	2.6	12.8 ± 1.4	164100 ± 1400	164469
ee						
0-jet low-p_Te 7 TeV	3.6	–	0.1	3.7 ± 0.5	190900 ± 1000	190890
0-jet low-p_Te 8 TeV	14.3	0.2	0.3	14.7 ± 2.2	519440 ± 700	519376
0-jet high-p_Te 7 TeV	4.0	–	0.5	4.5 ± 0.6	819900 ± 1700	820035
0-jet high-p_Te 8 TeV	22.3	0.3	2.5	25.1 ± 3.4	3225000 ± 2000	3225144
1-jet low-p_Te 7 TeV	1.5	0.2	0.1	1.8 ± 0.2	10268 ± 97	10300
1-jet low-p_Te 8 TeV	4.6	0.6	0.3	5.5 ± 0.7	26570 ± 180	26604
1-jet high-p_Te 7 TeV	2.4	0.4	0.6	3.4 ± 0.4	144900 ± 740	144945
1-jet high-p_Te 8 TeV	11.7	1.9	3.2	16.9 ± 1.8	560000 ± 1900	560104
2-jet 7 TeV	1.6	0.6	0.4	2.6 ± 0.4	35800 ± 280	35796
2-jet 8 TeV	5.0	2.8	1.6	9.4 ± 1.1	140000 ± 1200	140070

Table 20: Observed and predicted event yields in all event categories of the ee and μμ channels for the full discriminator value D region. The event yields of the predicted background distributions correspond to the result of the global fit. The signal yields, on the other hand, are normalized to the standard model prediction. The different signal processes are labelled as ggH (gluon-gluon fusion), VH (production in association with a W or Z boson), and VBF (vector-boson fusion).

Event category	Signal	Background	Data	$\frac{S}{S+B}$
$\ell\ell + LL'$				
$\mu\mu + \mu\tau_h$ 7 TeV	0.111 ± 0.005	2.4 ± 0.3	2	0.103
$\mu\mu + \mu\tau_h$ 8 TeV	0.427 ± 0.021	10.5 ± 0.6	12	0.092
$ee + \mu\tau_h$ 7 TeV	0.087 ± 0.004	1.5 ± 0.1	2	0.135
$ee + \mu\tau_h$ 8 TeV	0.385 ± 0.018	7.6 ± 0.4	11	0.149
$\mu\mu + e\tau_h$ 7 TeV	0.078 ± 0.004	2.2 ± 0.1	1	0.092
$\mu\mu + e\tau_h$ 8 TeV	0.293 ± 0.014	12.2 ± 0.6	8	0.081
$ee + e\tau_h$ 7 TeV	0.075 ± 0.004	2.2 ± 0.1	4	0.077
$ee + e\tau_h$ 8 TeV	0.279 ± 0.013	10.2 ± 0.5	13	0.063
$\mu\mu + \tau_h\tau_h$ 7 TeV	0.073 ± 0.006	0.8 ± 0.1	0	0.195
$\mu\mu + \tau_h\tau_h$ 8 TeV	0.285 ± 0.022	5.8 ± 0.4	4	0.150
$ee + \tau_h\tau_h$ 7 TeV	0.061 ± 0.004	1.1 ± 0.1	1	0.127
$ee + \tau_h\tau_h$ 8 TeV	0.260 ± 0.020	4.8 ± 0.4	9	0.148
$\mu\mu + e\mu$ 7 TeV	0.051 ± 0.002	1.0 ± 0.1	3	0.100
$\mu\mu + e\mu$ 8 TeV	0.202 ± 0.008	5.1 ± 0.3	9	0.105
$ee + e\mu$ 7 TeV	0.045 ± 0.002	1.0 ± 0.0	1	0.077
$ee + e\mu$ 8 TeV	0.185 ± 0.007	4.0 ± 0.2	4	0.082
$\ell + \tau_h\tau_h$				
$\mu + \tau_h\tau_h$ 7 TeV	0.35 ± 0.03	4.1 ± 0.4	2	0.098
$\mu + \tau_h\tau_h$ 8 TeV	1.57 ± 0.12	35.2 ± 2.1	38	0.054
$e + \tau_h\tau_h$ 7 TeV	0.23 ± 0.02	2.7 ± 0.2	0	0.101
$e + \tau_h\tau_h$ 8 TeV	0.87 ± 0.08	16.5 ± 1.1	15	0.062
$\ell + \ell'\tau_h$				
$\mu + \mu\tau_h$ 7 TeV	0.33 ± 0.02	3.2 ± 0.4	2	0.090
$\mu + \mu\tau_h$ low L_T 8 TeV	0.72 ± 0.03	20.7 ± 2.2	19	0.046
$\mu + \mu\tau_h$ high L_T 8 TeV	0.72 ± 0.02	8.4 ± 1.3	7	0.102
$e + \mu\tau_h / \mu + e\tau_h$ 7 TeV	0.47 ± 0.03	6.2 ± 1.0	6	0.074
$e + \mu\tau_h / \mu + e\tau_h$ low L_T 8 TeV	0.92 ± 0.03	24.6 ± 3.2	30	0.041
$e + \mu\tau_h / \mu + e\tau_h$ high L_T 8 TeV	1.15 ± 0.04	13.9 ± 2.0	11	0.109

Table 21: Observed and predicted event yields in all event categories of the $\ell\ell + LL'$and $\ell + L\tau_h$ channels for the full $m_{\tau\tau}$ and m_{vis} regions, respectively. The event yields of the predicted background distributions correspond to the result of the global fit. The signal yields, on the other hand, are normalized to the standard model prediction. Only SM Higgs boson production ($m_H = 125\,GeV$) in association with a W or Z boson is considered as a signal process. The $\frac{S}{S+B}$ variable denotes the ratio of the signal and the signal-plus-background yields in the central $m_{\tau\tau}$ range containing 68% of the signal events for $m_H = 125\,GeV$.

C FINAL EVENT YIELDS IN THE MSSM ANALYSIS

Table 22: Observed and expected number of events in the two event categories in the $\tau_h\tau_h$ channel. Other details are as in Tab. 23.

$\tau_h\tau_h$ channel		
	$\sqrt{s} = 8$TeV	
Process	no b-tag	b-tag
$Z \to \tau\tau$	2511 ± 97	60 ± 3
QCD	20192 ± 236	273 ± 21
W+jets	630 ± 165	17 ± 5
Z+jets (e, μ or jet faking τ)	115 ± 19	2 ± 0.4
$t\bar{t}$	38 ± 4	16 ± 2
Di-bosons + single top	63 ± 13	5 ± 1
Total background	23548 ± 174	374 ± 19
$h, H, A \to \tau\tau$	325 ± 34	30 ± 5
Observed data	23606	381
Efficiency $\times$ acceptance		
gluon fusion Higgs	9.11×10^{-3}	1.32×10^{-4}
b-quark associated Higgs	7.26×10^{-3}	1.37×10^{-3}

Table 23: Observed and expected number of events in the two event categories in the $e\tau_h$ channel, where the combined statistical and systematic uncertainty is shown. The expected signal yields for $h, H, A \to \tau\tau$ in the m_h^{max} scenario for m_A = 160GeVand $\tan\beta = 8$ and the signal efficiency times acceptance for a MSSM Higgs boson of 160GeVmass are also given.

$e\tau_h$ channel				
	$\sqrt{s} = 7$TeV		$\sqrt{s} = 8$TeV	
Process	no b-tag	b-tag	no b-tag	b-tag
$Z \to \tau\tau$	11819 ± 197	135 ± 4	30190 ± 345	453 ± 14
QCD	4163 ± 212	78 ± 11	11894 ± 544	194 ± 27
W+jets	1344 ± 112	29 ± 7	5646 ± 385	113 ± 25
Z+jets (e, μ or jet faking τ)	1334 ± 130	9 ± 1	6221 ± 360	83 ± 7
$t\bar{t}$	43 ± 3	19 ± 3	290 ± 22	102 ± 12
Di-bosons + single top	46 ± 5	7 ± 0.9	224 ± 23	30 ± 4
Total background	18750 ± 144	278 ± 11	54464 ± 259	975 ± 29
$h, H, A \to \tau\tau$	128 ± 13	10 ± 1	466 ± 43	37 ± 5
Observed data	18785	274	54547	975
Efficiency $\times$ acceptance				
gluon fusion Higgs	1.39×10^{-2}	1.24×10^{-4}	9.48×10^{-3}	1.11×10^{-4}
b-quark associated Higgs	1.12×10^{-2}	2.10×10^{-3}	7.78×10^{-3}	1.49×10^{-3}

Table 24: Observed and expected number of events in the two event categories in the $\mu\tau_h$ channel. Other details are as in Tab. 23.

$\mu\tau_h$ channel				
	$\sqrt{s} = 7$TeV		$\sqrt{s} = 8$TeV	
Process	no b-tag	b-tag	no b-tag	b-tag
$Z \to \tau\tau$	26838 ± 244	284 ± 8	87399 ± 497	1118 ± 31
QCD	5495 ± 258	131 ± 18	18056 ± 811	552 ± 62
W+jets	2779 ± 201	55 ± 14	12845 ± 793	237 ± 52
Z+jets (e, μ or jet faking τ)	716 ± 109	11 ± 2	3704 ± 454	54 ± 9
$t\bar{t}$	82 ± 6	36 ± 5	564 ± 41	194 ± 22
Di-bosons + single top	94 ± 11	12 ± 2	506 ± 51	60 ± 7
Total background	36004 ± 205	530 ± 18	123075 ± 407	2214 ± 44
$h, H, A \to \tau\tau$	226 ± 23	17 ± 2	929 ± 85	67 ± 9
Observed data	36055	542	123239	2219
Efficiency $\times$ acceptance				
gluon fusion Higgs	2.34×10^{-2}	2.49×10^{-4}	1.78×10^{-2}	2.32×10^{-4}
b-quark associated Higgs	1.96×10^{-2}	3.54×10^{-3}	1.53×10^{-2}	2.66×10^{-3}

Table 25: Observed and expected number of events in the two event categories in the eμ channel. Other details are as in Tab. 23.

eμ channel				
	$\sqrt{s} = 7$TeV		$\sqrt{s} = 8$TeV	
Process	no b-tag	b-tag	no b-tag	b-tag
$Z \to \tau\tau$	13783 ± 134	165 ± 5	48218 ± 300	679 ± 8
QCD	804 ± 114	14 ± 3	4302 ± 356	148 ± 17
$t\bar{t}$	467 ± 29	309 ± 18	2215 ± 158	1183 ± 48
Di-bosons + single top	501 ± 55	63 ± 8	2367 ± 248	308 ± 38
Total background	15556 ± 128	551 ± 21	57102 ± 257	2318 ± 37
$h, H, A \to \tau\tau$	114 ± 11	9 ± 1	455 ± 43	34 ± 4
Observed data	15436	558	57285	2353
Efficiency × acceptance				
gluon fusion Higgs	1.14×10^{-2}	1.11×10^{-4}	8.83×10^{-3}	8.85×10^{-5}
b-quark associated Higgs	9.70×10^{-3}	1.80×10^{-3}	7.59×10^{-3}	1.33×10^{-3}

Table 26: Observed and expected number of events in the two event categories in the μμ channel. Other details are as in Tab. 23.

μμ channel				
	$\sqrt{s} = 7$TeV		$\sqrt{s} = 8$TeV	
Process	no b-tag	b-tag	no b-tag	b-tag
$Z \to \tau\tau$	6838 ± 118	34 ± 1	20931 ± 376	101 ± 5
$Z \to \mu\mu$	562008 ± 764	1435 ± 34	1894509 ± 1566	5125 ± 69
QCD	380 ± 51	4 ± 2	1131 ± 108	31 ± 7
$t\bar{t}$	183 ± 15	83 ± 7	809 ± 62	324 ± 15
Di-bosons + single top	1114 ± 221	10 ± 2	5543 ± 625	48 ± 8
Total background	570523 ± 763	1566 ± 35	1922923 ± 1439	5629 ± 72
$h, H, A \to \tau\tau$	57 ± 5	3 ± 0.4	195 ± 17	8 ± 1
Observed data	570616	1559	1922924	5608
Efficiency × acceptance				
gluon fusion Higgs	5.66×10^{-3}	2.55×10^{-5}	3.73×10^{-3}	2.29×10^{-5}
b-quark associated Higgs	5.33×10^{-3}	6.65×10^{-4}	3.58×10^{-3}	3.42×10^{-4}

BIBLIOGRAPHY

[1] https://twiki.cern.ch/twiki/bin/viewauth/CMS/PileupMCReweightingUtilities.

[2] Georges Aad et al. Search for neutral MSSM Higgs bosons decaying to $\tau^+\tau^-$ pairs in proton-proton collisions at $\sqrt{s} = 7$ Tev with the ATLAS detector. *Phys. Lett. B*, 705:174, 2011. doi: 10.1016/j.physletb.2011.10.001.

[3] Georges Aad et al. Observation of a new particle in the search for the Standard Model Higgs boson with the ATLAS detector at the LHC. *Phys. Lett. B*, 716:1, 2012. doi: 10.1016/j.physletb.2012.08.020.

[4] T. Aaltonen et al. Search for Higgs bosons predicted in two-Higgs-doublet models via decays to tau lepton pairs in 1.96-TeV p anti-p collisions. *Phys. Rev. Lett.*, 103:201801, 2009. doi: 10.1103/PhysRevLett.103.201801.

[5] T. Aaltonen et al. Search for Higgs bosons produced in association with b quarks. *Phys. Rev. D*, 85:032005, 2012. doi: 10.1103/PhysRevD.85.032005.

[6] T. Aaltonen et al. Evidence for a particle produced in association with weak bosons and decaying to a bottom-antibottom quark pair in Higgs boson searches at the Tevatron. *Phys.Rev.Lett.*, 109:071804, 2012. doi: 10.1103/PhysRevLett.109.071804.

[7] S. Abachi et al. Observation of the top quark. *Phys.Rev.Lett.*, 74:2632–2637, 1995. doi: 10.1103/PhysRevLett.74.2632.

[8] Victor Mukhamedovich Abazov et al. Search for neutral Higgs bosons in the multi-b-jet topology in 5.2 fb^{-1} of $p\bar{p}$ collisions at $\sqrt{s} = 1.96$ TeV. *Phys. Lett. B*, 698:97, 2011. doi: 10.1016/j.physletb.2011.02.062.

[9] Victor Mukhamedovich Abazov et al. Search for Higgs bosons decaying to $\tau\tau$ pairs in $p\bar{p}$ collisions at $\sqrt{s} = 1.96$ TeV. *Phys. Lett. B*, 707:323, 2012. doi: 10.1016/j.physletb.2011.12.050.

[10] F. Abe et al. Observation of top quark production in $\bar{p}p$ collisions. *Phys.Rev.Lett.*, 74:2626–2631, 1995. doi: 10.1103/PhysRevLett.74.2626.

[11] U. Aglietti, R. Bonciani, G. Degrassi, and A. Vicini. Two loop light fermion contribution to Higgs production and decays. *Phys. Lett. B*, 595:432, 2004. doi: 10.1016/j.physletb.2004.06.063.

[12] S. Agostinelli, J. Allison, K. Amako, J. Apostolakis, H. Araujo, P. Arce, M. Asai, D. Axen, S. Banerjee, G. Barrand, F. Behner, L. Bellagamba, J. Boudreau, L. Broglia, A. Brunengo, H. Burkhardt, S. Chauvie, J. Chuma, R. Chytracek, G. Cooperman, G. Cosmo, P. Degtyarenko, A. Dell'Acqua, G. Depaola, D. Dietrich, R. Enami, A. Feliciello, C. Ferguson, H. Fesefeldt, G. Folger, F. Foppiano, A. Forti, S. Garelli, S. Giani, R. Giannitrapani, D. Gibin, J.J. GÛmez Cadenas, I. GonzÂ·lez, G. Gracia Abril, G. Greeniaus, W. Greiner, V. Grichine, A. Grossheim, S. Guatelli, P. Gumplinger, R. Hamatsu, K. Hashimoto, H. Hasui, A. Heikkinen, A. Howard, V. Ivanchenko, A. Johnson, F.W. Jones, J. Kallenbach, N. Kanaya, M. Kawabata, Y. Kawabata, M. Kawaguti, S. Kelner, P. Kent, A. Kimura, T. Kodama, R. Kokoulin, M. Kossov, H. Kurashige, E. Lamanna, T. LampÈn, V. Lara, V. Lefebure, F. Lei, M. Liendl, W. Lockman, F. Longo, S. Magni, M. Maire, E. Medernach, K. Minamimoto, P. Mora de Freitas, Y. Morita, K. Murakami, M. Nagamatu, R. Nartallo, P. Nieminen, T. Nishimura, K. Ohtsubo, M. Okamura, S. O'Neale, Y. Oohata, K. Paech, J. Perl, A. Pfeiffer, M.G. Pia, F. Ranjard, A. Rybin, S. Sadilov, E. Di Salvo, G. Santin, T. Sasaki, N. Savvas, Y. Sawada, S. Scherer, S. Sei, V. Sirotenko, D. Smith, N. Starkov, H. Stoecker, J. Sulkimo, M. Takahata, S. Tanaka, E. Tcherniaev, E. Safai Tehrani, M. Tropeano, P. Truscott, H. Uno, L. Urban, P. Urban, M. Verderi, A. Walkden, W. Wander, H. Weber, J.P. Wellisch, T. Wenaus, D.C. Williams, D. Wright, T. Yamada, H. Yoshida, and D. Zschiesche. Geant4 a simulation toolkit. *Nuclear Instruments and Methods in Physics Research Section A: Accelerators, Spectrometers, Detectors and Associated Equipment*, 506(3):250 – 303, 2003. ISSN 0168-9002. doi: 10.1016/S0168-9002(03)01368-8. URL http://www.sciencedirect.com/science/article/pii/S0168900203013688.

[13] ALEPH, DELPHI, L3, OPAL Collaborations, and the LEP Working Group for Higgs Boson Searches, S. Schael, et al. Search for neutral MSSM Higgs bosons at LEP. *Eur. Phys. J. C*, 47:547, 2006. doi: 10.1140/epjc/s2006-02569-7.

[14] Simone Alioli, Paolo Nason, Carlo Oleari, and Emanuele Re. NLO Higgs boson production via gluon fusion matched with shower in POWHEG. *JHEP*, 04:002, 2009. doi: 10.1088/1126-6708/2009/04/002.

[15] Simone Alioli, Paolo Nason, Carlo Oleari, and Emanuele Re. A general framework for implementing NLO calculations in shower Monte Carlo programs: the POWHEG BOX. *JHEP*, 06:043, 2010. doi: 10.1007/JHEP06(2010)043.

[16] J. Allison, K. Amako, J. Apostolakis, H. Araujo, P.A. Dubois, M. Asai, G. Barrand, R. Capra, S. Chauvie, R. Chytracek, G.A.P. Cirrone, G. Cooperman, G. Cosmo, G. Cuttone, G.G. Daquino, M. Donszelmann, M. Dressel, G. Folger, F. Foppiano, J. Generowicz, V. Grichine, S. Guatelli, P. Gumplinger, A. Heikkinen, I. Hrivnacova, A. Howard, S. Incerti, V. Ivanchenko, T. Johnson, F. Jones, T. Koi, R. Kokoulin, M. Kossov, H. Kurashige, V. Lara, S. Larsson, F. Lei, O. Link, F. Longo, M. Maire, A. Mantero, B. Mascialino, I. McLaren, P.M. Lorenzo, K. Minamimoto, K. Murakami, P. Nieminen, L. Pandola, S. Parlati, L. Peralta, J. Perl, A. Pfeiffer, M.G. Pia, A. Ribon, P. Rodrigues, G. Russo, S. Sadilov, G. Santin, T. Sasaki, D. Smith, N. Starkov, S. Tanaka, E. Tcherniaev, B. Tome, A. Trindade, P. Truscott, L. Urban, M. Verderi, A. Walkden, J.P. Wellisch, D.C. Williams, D. Wright, and H. Yoshida. Geant4 developments and applications. *Nuclear Science, IEEE Transactions on*, 53(1):270 –278, feb. 2006. ISSN 0018-9499. doi: 10.1109/TNS.2006.869826.

[17] Johan Alwall, Michel Herquet, Fabio Maltoni, Olivier Mattelaer, and Tim Stelzer. MadGraph 5: going beyond. *JHEP*, 06:128, 2011. doi: 10.1007/JHEP06(2011)128.

[18] Charalampos Anastasiou and Kirill Melnikov. Higgs boson production at hadron colliders in NNLO QCD. *Nucl. Phys. B*, 646: 220, 2002. doi: 10.1016/S0550-3213(02)00837-4.

[19] Charalampos Anastasiou and Kirill Melnikov. Pseudoscalar Higgs boson production at hadron colliders in NNLO QCD. *Phys. Rev. D*, 67:037501, 2003. doi: 10.1103/PhysRevD.67.037501.

[20] G. Arnison et al. Experimental Observation of Isolated Large Transverse Energy Electrons with Associated Missing Energy at s**(1/2) = 540-GeV. *Phys.Lett.*, B122:103–116, 1983. doi: 10.1016/0370-2693(83)91177-2.

[21] ATLAS and CMS Collaborations, LHC Higgs Combination Group. Procedure for the LHC Higgs boson search combination in Summer 2011. Technical Report ATL-PHYS-PUB 2011-11, CMS NOTE 2011/005, CERN, 2011. URL http://cdsweb.cern.ch/record/1379837.

[22] M. Banner et al. Observation of Single Isolated Electrons of High Transverse Momentum in Events with Missing Transverse Energy at the CERN anti-p p Collider. *Phys.Lett.*, B122:476–485, 1983. doi: 10.1016/0370-2693(83)91605-2.

[23] R. Barate et al. Search for the standard model Higgs boson at LEP. *Phys.Lett.*, B565:61–75, 2003. doi: 10.1016/S0370-2693(03)00614-2.

[24] Roger J. Barlow and Christine Beeston. Fitting using finite Monte Carlo samples. *Comput. Phys. Commun.*, 77:219, 1993. doi: 10.1016/0010-4655(93)90005-W.

[25] J. Beringer et al. Review of particle physics. *Phys. Rev. D*, 86: 010001, 2012. doi: 10.1103/PhysRevD.86.010001.

[26] R. Bonciani, G. Degrassi, and A. Vicini. On the generalized harmonic polylogarithms of one complex variable. *Comput. Phys. Commun.*, 182:1253, 2011. doi: 10.1016/j.cpc.2011.02.011.

[27] B.K. Bullock, Kaoru Hagiwara, and Alan D. Martin. Tau polarization and its correlations as a probe of new physics. *Nucl. Phys. B*, 395:499, 1993. doi: 10.1016/0550-3213(93)90045-Q.

[28] Matteo Cacciari, Gavin P. Salam, and Gregory Soyez. The anti-k_t jet clustering algorithm. *JHEP*, 04:063, 2008. doi: 10.1088/1126-6708/2008/04/063.

[29] M. S. Carena, S. Heinemeyer, O. Stal, C. E. M. Wagner, and G. Weiglein. MSSM Higgs boson searches at the LHC: benchmark scenarios after the discovery of a Higgs-like particle. *Eur. Phys. J. C*, 73:2552, 2013. doi: 10.1140/epjc/s10052-013-2552-1.

[30] Marcela S. Carena, S. Heinemeyer, C. E. M. Wagner, and G. Weiglein. Suggestions for benchmark scenarios for MSSM Higgs boson searches at hadron colliders. *Eur. Phys. J. C*, 26:601, 2003. doi: 10.1140/epjc/s2002-01084-3.

[31] Marcela S. Carena, S. Heinemeyer, C. E. M. Wagner, and G. Weiglein. MSSM Higgs boson searches at the Tevatron and the LHC: Impact of different benchmark scenarios. *Eur. Phys. J. C*, 45:797, 2006. doi: 10.1140/epjc/s2005-02470-y.

[32] Serguei Chatrchyan et al. Determination of jet energy calibration and transverse momentum resolution in CMS. *JINST*, 6: 11002, 2011. doi: 10.1088/1748-0221/6/11/P11002.

[33] Serguei Chatrchyan et al. Search for Neutral MSSM Higgs Bosons Decaying to Tau Pairs in pp Collisions at $\sqrt{s} = 7$ TeV. *Phys. Rev. Lett.*, 106:231801, 2011. doi: 10.1103/PhysRevLett.106.231801.

[34] Serguei Chatrchyan et al. Missing transverse energy performance of the CMS detector. *JINST*, 6:P09001, 2011. doi: 10.1088/1748-0221/6/09/P09001.

[35] Serguei Chatrchyan et al. Performance of τ-lepton reconstruction and identification in CMS. *JINST*, 7:P01001, 2012. doi: 10.1088/1748-0221/7/01/P01001.

[36] Serguei Chatrchyan et al. Measurement of the single-top-quark t-channel cross section in pp collisions at $\sqrt{s} = 7$ TeV. *JHEP*, 12: 035, 2012. doi: 10.1007/JHEP12(2012)035.

[37] Serguei Chatrchyan et al. Combined results of searches for the standard model Higgs boson in pp collisions at $\sqrt{s} = 7$ TeV. *Phys. Lett. B*, 710:26, 2012. doi: 10.1016/j.physletb.2012.02.064.

[38] Serguei Chatrchyan et al. Observation of a new boson at a mass of 125 GeV with the CMS experiment at the LHC. *Phys. Lett. B*, 716:30, 2012. doi: 10.1016/j.physletb.2012.08.021.

[39] Serguei Chatrchyan et al. Performance of CMS muon reconstruction in pp collision events at $\sqrt{s} = 7$ TeV. *JINST*, 7:P10002, 2012. doi: 10.1088/1748-0221/7/10/P10002.

[40] Serguei Chatrchyan et al. Identification of b-quark jets with the CMS experiment. *JINST*, 8:P04013, 2013. doi: 10.1088/1748-0221/8/04/P04013.

[41] Serguei Chatrchyan et al. Observation of a new boson with mass near 125 GeV in pp collisions at $\sqrt{s}$ = 7 and 8 TeV. *JHEP*, 06:081, 2013. doi: 10.1007/JHEP06(2013)081.

[42] Serguei Chatrchyan et al. Measurement of the W^+W^- and ZZ production cross sections in pp collisions at $\sqrt{s}$ = 8 TeV. *Phys. Lett. B*, 721:190, 2013. doi: 10.1016/j.physletb.2013.03.027.

[43] Serguei Chatrchyan et al. Measurement of associated production of vector bosons and top quark-antiquark pairs in pp collisions at $\sqrt{s}$ = 7 TeV. *Phys. Rev. Lett.*, 110:172002, 2013. doi: 10.1103/PhysRevLett.110.172002.

[44] Serguei Chatrchyan et al. Search for a Higgs boson decaying into a b-quark pair and produced in association with b quarks in proton-proton collisions at 7 TeV. *Phys. Lett. B*, 722:207, 2013. doi: 10.1016/j.physletb.2013.04.017.

[45] Serguei Chatrchyan et al. Evidence for the 125 GeV Higgs boson decaying to a pair of τ leptons. *JHEP*, 05:104, 2014. doi: 10.1007/JHEP05(2014)104.

[46] CMS Collaboration. Particle–flow event reconstruction in CMS and performance for jets, taus, and $\not{E}_T$. CMS Physics Analysis Summary CMS-PAS-PFT-09-001, CERN, 2009. URL http://cdsweb.cern.ch/record/1194487.

[47] CMS Collaboration. Electron reconstruction and identification at $\sqrt{s} = 7$ TeV. CMS Physics Analysis Summary CMS-PAS-EGM-10-004, 2010. URL http://cdsweb.cern.ch/record/1299116.

[48] CMS Collaboration. Jet performance in pp collisions at $\sqrt{s}$=7 TeV. CMS Physics Analysis Summary CMS-PAS-JME-10-003, CERN, 2010. URL http://cdsweb.cern.ch/record/1279362.

[49] CMS Collaboration. Commissioning of the Particle-flow Event Reconstruction with the first LHC collisions recorded in the CMS detector. CMS Physics Analysis Summary CMS-PAS-PFT-10-001, 2010. URL http://cdsweb.cern.ch/record/1247373.

[50] CMS Collaboration. Commissioning of the particle-flow reconstruction in minimum-bias and jet events from p p collisions at 7 TeV. CMS Physics Analysis Summary CMS-PAS-PFT-10-002, 2010. URL http://cdsweb.cern.ch/record/1279341.

[51] CMS Collaboration. Commissioning of the particle-flow event reconstruction with leptons from J/ψ and W decays at 7 TeV. CMS Physics Analysis Summary CMS-PAS-PFT-10-003, 2010. URL http://cdsweb.cern.ch/record/1279347.

[52] CMS Collaboration. Performance of missing transverse momentum reconstruction algorithms in proton-proton collisions at $\sqrt{s} = 8$ TeV with the CMS detector. CMS Physics Analysis Summary CMS-PAS-JME-12-002, CERN, 2012. URL http://cdsweb.cern.ch/record/1543527.

[53] CMS Collaboration. Absolute calibration of the luminosity measurement at CMS: Winter 2012 update. CMS Physics Analysis Summary CMS-PAS-SMP-12-008, CERN, 2012. URL http://cdsweb.cern.ch/record/1434360.

[54] CMS Collaboration. Cms luminosity based on pixel cluster counting - summer 2013 update. CMS Physics Analysis Summary CMS-PAS-LUM-13-001, CERN, 2013. URL http://cdsweb.cern.ch/record/1598864.

[55] CMS Collaboration. The Electromagnetic Calorimeter Technical Design Report. Technical Report CERN/LHCC 97-033, CERN, 1997.

[56] CMS Collaboration. The Magnet Project Technical Design Report. Technical Report CERN/LHCC 97-010, CERN, 1997.

[57] CMS Collaboration. The Muon Project Technical Design Report. Technical Report CERN/LHCC 97-32, CERN, 1997.

[58] CMS Collaboration. CMS. the TriDAS project. Technical design report, vol. 1: The trigger systems. Technical Report CERN-LHCC-2000-038, CERN, 2000.

[59] CMS Collaboration. CMS: The TriDAS project. Technical design report, vol. 2: Data acquisition and high-level trigger. Technical report, CERN, 2002.

[60] CMS Collaboration. CMS Physics Technical Design Report Volume I : Detector Performance and Software. Technical Report CERN-LHCC-2006-001, CERN, 2006.

[61] CMS Collaboration. CMS Physics Technical Design Report: Volume II (PTDR2), Physics Performance. Technical Report CERN-LHCC-2006-021, CERN, 2006.

[62] CMS Collaboration. Plans for jet energy corrections at cms, 2007. CMS AN-2007/055.

[63] CMS Collaboration. Plans for jet energy corrections at cms, 2007. CMS-PAS-JME-07-002.

[64] CMS Collaboration. Mc truth l2 & l3 factorized jet corrections at cms, 2008. CMS AN-2008/003.

[65] CMS Collaboration. Determination of the relative jet energy scale at cms from dijet balance, 2008. CMS AN-2008/031.

[66] CMS Collaboration. Calorimeter jet quality criteria for the first cms collision data, and preparations for calibrating their efficiencies, 2009. CMS AN-2009/087.

[67] CMS Collaboration. Performance of muon identification in pp collisions at $\sqrt{s}$ = 7 TeV. *CMS Physics Analysis Summary*, CMS-PAS-MUO-10-002, 2010. URL http://cdsweb.cern.ch/record/1279140.

[68] CMS Collaboration. b-jet identification in the cms experiment, 2011. CMS-PAS-BTV-11-004.

[69] CMS Collaboration. Measurement of the ww, wz and zz cross sections at cms, 2011. CMS-PAS-EWK-11-010.

[70] CMS Collaboration. Measurement of top quark pair differential cross sections at $\sqrt{s} = 7$ tev, 2011. CMS-PAS-TOP-11-013.

[71] CMS Collaboration. Combination of top pair production cross section measurements, 2011. CMS-PAS-TOP-11-024.

[72] CMS Collaboration. Modelling backgrounds via embedding technique applied on rechit level, 2013. AN-13-073.

[73] CMS Collaboration. Physics objects in the higgs to tau tau analysis, 2013. AN-13-188.

[74] CMS Collaboration. Performance of b tagging at $\sqrt{s} = 8$ tev in multijet, ttbar and boosted topology events, 2013. CMS-PAS-BTV-13-001.

[75] J. S. Conway. Incorporating nuisance parameters in likelihoods for multisource spectra. In *Proceedings of PHYSTAT 2011 Workshop on Statistical Issues Related to Discovery Claims in Search Experiments and Unfolding*, page 115. CERN-2011-006, 2011. URL http://cdsweb.cern.ch/record/1306523.

[76] S. Dawson, C. B. Jackson, L. Reina, and D. Wackeroth. Exclusive Higgs boson production with bottom quarks at hadron colliders. *Phys. Rev. D*, 69:074027, 2004. doi: 10.1103/PhysRevD.69.074027.

[77] G. Degrassi and P. Slavich. NLO QCD bottom corrections to Higgs boson production in the MSSM. *JHEP*, 11:044, 2010. doi: 10.1007/JHEP11(2010)044.

[78] G. Degrassi, S. Heinemeyer, W. Hollik, P. Slavich, and G. Weiglein. Towards high precision predictions for the MSSM Higgs sector. *Eur. Phys. J. C*, 28:133, 2003. doi: 10.1140/epjc/s2003-01152-2.

[79] G. Degrassi, S. Di Vita, and P. Slavich. NLO QCD corrections to pseudoscalar Higgs production in the MSSM. *JHEP*, 08:128, 2011. doi: 10.1007/JHEP08(2011)128.

[80] G. Degrassi, S. Di Vita, and P. Slavich. On the NLO QCD corrections to the production of the heaviest neutral Higgs scalar in the MSSM. *Eur. Phys. J. C*, 72:2032, 2012. doi: 10.1140/epjc/s10052-012-2032-z.

[81] S. Dittmaier, M. Krämer, and M. Spira. Higgs radiation off bottom quarks at the Tevatron and the CERN LHC. *Phys. Rev. D*, 70:074010, 2004. doi: 10.1103/PhysRevD.70.074010.

[82] A. Djouadi, J. Kalinowski, and M. Spira. HDECAY: A Program for Higgs boson decays in the standard model and its supersymmetric extension. *Comput. Phys. Commun.*, 108:56, 1998. doi: 10.1016/S0010-4655(97)00123-9.

[83] A. Djouadi, M. M. Mühlleitner, and M. Spira. Decays of supersymmetric particles: The Program SUSY-HIT (SUspect-SdecaY-Hdecay-InTerface). *Acta Phys. Polon. B*, 38:635, 2007.

[84] R. K. Ellis, I. Hinchliffe, M. Soldate, and J. J. van der Bij. Higgs decay to $\tau^+\tau^-$: A possible signature of intermediate mass higgs bosons at high energy hadron colliders. *Nucl. Phys. B*, 297:221, 1988. doi: 10.1016/0550-3213(88)90019-3.

[85] F. Englert and R. Brout. Broken Symmetry and the Mass of Gauge Vector Mesons. *Phys. Rev. Lett.*, 13:321, 1964. doi: 10.1103/PhysRevLett.13.321.

[86] Pierre Fayet. Supergauge invariant extension of the Higgs mechanism and a model for the electron and its neutrino. *Nucl. Phys. B*, 90:104, 1975. doi: 10.1016/0550-3213(75)90636-7.

[87] Pierre Fayet. Spontaneously broken supersymmetric theories of weak, electromagnetic and strong interactions. *Phys. Lett. B*, 69: 489, 1977. doi: 10.1016/0370-2693(77)90852-8.

[88] Markus Frank, Thomas Hahn, Sven Heinemeyer, Wolfgang Hollik, Heidi Rzehak, and Georg Weiglein. The Higgs boson masses and mixings of the complex MSSM in the Feynman-diagrammatic approach. *JHEP*, 02:047, 2007. doi: 10.1088/1126-6708/2007/02/047.

[89] Stefano Frixione and Bryan R. Webber. Matching NLO QCD computations and parton shower simulations. *JHEP*, 06:029, 2002. doi: 10.1088/1126-6708/2002/06/029.

[90] Stefano Frixione, Paolo Nason, and Carlo Oleari. Matching NLO QCD computations with Parton Shower simulations: the POWHEG method. *JHEP*, 0711:070, 2007. doi: 10.1088/1126-6708/2007/11/070. * Temporary entry *.

[91] G. Bauer et al. Modeling of $w \to \ell\nu$ met with boson recoil. *CMS Analysis Note*, AN-10-332, 2010.

[92] S. L. Glashow. Partial Symmetries of Weak Interactions. *Nucl. Phys.*, 22:579, 1961. doi: 10.1016/0029-5582(61)90469-2.

[93] Yu. A. Golfand and E. P. Likhtman. Extension of the Algebra of Poincare Group Generators and Violation of p Invariance. *JETP Lett.*, 13:323, 1971.

[94] G. S. Guralnik, C. R. Hagen, and T. W. B. Kibble. Global Conservation Laws and Massless Particles. *Phys. Rev. Lett.*, 13:585, 1964. doi: 10.1103/PhysRevLett.13.585.

[95] Keith Hamilton, Paolo Nason, and Giulia Zanderighi. MINLO: multi-scale improved NLO. *JHEP*, 10:155, 2012. doi: 10.1007/JHEP10(2012)155.

[96] Robert Harlander, Michael Kramer, and Markus Schumacher. Bottom-quark associated Higgs-boson production: reconciling the four- and five-flavour scheme approach. 2011.

[97] Robert V. Harlander and Philipp Kant. Higgs production and decay: Analytic results at next-to-leading order QCD. *JHEP*, 12: 015, 2005. doi: 10.1088/1126-6708/2005/12/015.

[98] Robert V. Harlander and William B. Kilgore. Production of a pseudo-scalar Higgs boson at hadron colliders at next-to-next-to leading order. *JHEP*, 10:017, 2002.

[99] Robert V. Harlander and William B. Kilgore. Next-to-next-to-leading order Higgs production at hadron colliders. *Phys. Rev. Lett.*, 88:201801, 2002. doi: 10.1103/PhysRevLett.88.201801.

[100] Robert V. Harlander and William B. Kilgore. Higgs boson production in bottom quark fusion at next-to-next-to leading order. *Phys. Rev. D*, 68:013001, 2003. doi: 10.1103/PhysRevD.68.013001.

[101] Robert V. Harlander and Matthias Steinhauser. Supersymmetric Higgs production in gluon fusion at next-to-leading order. *JHEP*, 09:066, 2004. doi: 10.1088/1126-6708/2004/09/066.

[102] Robert V. Harlander, Stefan Liebler, and Hendrik Mantler. SusHi: A program for the calculation of Higgs production in gluon fusion and bottom-quark annihilation in the Standard Model and the MSSM. *Comput. Phys. Commun.*, 184:1605, 2013. doi: 10.1016/j.cpc.2013.02.006.

[103] S. Heinemeyer, W. Hollik, and G. Weiglein. The Masses of the neutral $\mathcal{CP}$-even Higgs bosons in the MSSM: Accurate analysis at the two-loop level. *Eur. Phys. J. C*, 9:343, 1999. doi: 10.1007/s100529900006.

[104] S. Heinemeyer, W. Hollik, and G. Weiglein. FeynHiggs: a program for the calculation of the masses of the neutral CP-even Higgs bosons in the MSSM. *Comput. Phys. Commun.*, 124:76–89, 2000. doi: 10.1016/S0010-4655(99)00364-1.

[105] S. Heinemeyer, O. Stål, and G. Weiglein. Interpreting the LHC Higgs search results in the MSSM. *Phys. Lett. B*, 710:201, 2012. doi: 10.1016/j.physletb.2012.02.084.

[106] Peter W. Higgs. Broken symmetries, massless particles and gauge fields. *Phys. Lett.*, 12:132, 1964. doi: 10.1016/0031-9163(64)91136-9.

[107] Peter W. Higgs. Broken Symmetries and the Masses of Gauge Bosons. *Phys. Rev. Lett.*, 13:508, 1964. doi: 10.1103/PhysRevLett.13.508.

[108] Peter W. Higgs. Spontaneous Symmetry Breakdown without Massless Bosons. *Phys. Rev.*, 145:1156, 1966. doi: 10.1103/PhysRev.145.1156.

[109] Stanisław Jadach, Johann H. Kühn, and Zbigniew Wąs. TAUOLA - a library of Monte Carlo programs to simulate decays of polarized tau leptons. *Comput. Phys. Commun.*, 64:275, 1991. doi: 10.1016/0010-4655(91)90038-M.

[110] Thomas Junk. Confidence level computation for combining searches with small statistics. *Nucl. Instrum. Meth. A*, 434:435, 1999. doi: 10.1016/S0168-9002(99)00498-2.

[111] Vardan Khachatryan et al. Search for neutral MSSM Higgs bosons decaying to a pair of tau leptons in pp collisions. *JHEP*, 1410:160, 2014. doi: 10.1007/JHEP10(2014)160.

[112] T. W. B. Kibble. Symmetry breaking in non-Abelian gauge theories. *Phys. Rev.*, 155:1554, 1967. doi: 10.1103/PhysRev.155.1554.

[113] LHC Higgs Cross Section Working Group. Handbook of LHC Higgs Cross Sections: 3. Higgs Properties. CERN Report CERN-2013-004, CERN, 2013.

[114] LHC Higgs Cross Section Working Group, S. Dittmaier, C. Mariotti, G. Passarino, and R. Tanaka (Eds.). Handbook of LHC Higgs Cross Sections: 1. Inclusive Observables. *CERN-2011-002*, CERN, Geneva, 2011.

[115] LHC Higgs Cross Section Working Group, S. Dittmaier, C. Mariotti, G. Passarino, and R. Tanaka (Eds.). Handbook of LHC Higgs Cross Sections: 1. Inclusive Observables. *CERN-2011-002*, CERN, Geneva, 2011.

[116] A. D. Martin, W. J. Stirling, R. S. Thorne, and G. Watt. Uncertainties on α_S in global PDF analyses and implications for predicted hadronic cross sections. *Eur. Phys. J. C*, 64:653, 2009. doi: 10.1140/epjc/s10052-009-1164-2.

[117] A. D. Martin, W. J. Stirling, R. S. Thorne, and G. Watt. Parton distributions for the LHC. *Eur. Phys. J. C*, 63:189, 2009. doi: 10.1140/epjc/s10052-009-1072-5.

[118] S. P. Martin. A Supersymmetry Primer. *arXiv:hep-ph/970935v5*, 2008.

[119] Kirill Melnikov and Frank Petriello. The W boson production cross section at the LHC through O(alpha**2(s). *Phys. Rev. Lett.*, 96:231803, 2006. doi: 10.1103/PhysRevLett.96.231803.

[120] Kirill Melnikov and Frank Petriello. Electroweak gauge boson production at hadron colliders through O(alpha(s)**2). *Phys. Rev.*, D74:114017, 2006. doi: 10.1103/PhysRevD.74.114017.

[121] Paolo Nason. A new method for combining NLO QCD with shower Monte Carlo algorithms. *JHEP*, 11:040, 2004. doi: 10.1088/1126-6708/2004/11/040.

[122] Paolo Nason and Carlo Oleari. NLO Higgs boson production via vector-boson fusion matched with shower in POWHEG. *JHEP*, 1002:037, 2010. doi: 10.1007/JHEP02(2010)037.

[123] V. Ravindran, J. Smith, and W. L. van Neerven. NNLO corrections to the total cross section for Higgs boson production in hadron-hadron collisions. *Nucl. Phys. B*, 665:325, 2003. doi: 10.1016/S0550-3213(03)00457-7.

[124] A. L. Read. Presentation of search results: the $\mathtt{cl}_s$ technique. *J. Phys. G*, 28:2693, 2002. doi: 10.1088/0954-3899/28/10/313.

[125] Alexander L. Read. Presentation of search results: The CL_s technique. *J. Phys. G*, 28:2693, 2002. doi: 10.1088/0954-3899/28/10/313.

[126] K. Rose. Deterministic annealing for clustering, compression, classification, regression, and related optimization problems. *Proceedings of the IEEE*, 86:2210, 1998. doi: 10.1109/5.726788.

[127] Abdus Salam. Weak and electromagnetic interactions. In Nils Svartholm, editor, *Elementary particle physics: relativistic groups and analyticity*, page 367, Stockholm, 1968. Almqvist & Wiksell. Proceedings of the eighth Nobel symposium.

[128] Gavin P. Salam. Towards Jetography. *Eur. Phys. J.*, C67:637–686, 2010. doi: 10.1140/epjc/s10052-010-1314-6.

[129] Torbjorn Sjostrand, Leif Lonnblad, Stephen Mrenna, and Peter Z. Skands. Pythia 6.3 physics and manual. 2003.

[130] Torbjörn Sjöstrand, Stephen Mrenna, and Peter Skands. PYTHIA 6.4 physics and manual. *JHEP*, 05:026, 2006. doi: 10.1088/1126-6708/2006/05/026.

[131] M. Spira, A. Djouadi, D. Graudenz, and P. M. Zerwas. Higgs boson production at the LHC. *Nucl. Phys. B*, 453:17, 1995. doi: 10.1016/0550-3213(95)00379-7.

[132] Michael Spira. HIGLU: A program for the calculation of the total Higgs production cross-section at hadron colliders via gluon fusion including QCD corrections. DESY Report DESY-T-95-05, 1995.

[133] Michael Spira. QCD effects in Higgs physics. *Fortsch. Phys.*, 46:203, 1998. doi: 10.1002/(SICI)1521-3978(199804)46:3<203::AID-PROP203>3.0.CO;2-4.

[134] Z. Was. TAUOLA the library for tau lepton decay, and KKMC/KORALB/KORALZ/... status report. *Nucl. Phys. Proc. Suppl.*, 98:96–102, 2001. doi: 10.1016/S0920-5632(01)01200-2.

[135] Steven Weinberg. A Model of Leptons. *Phys. Rev. Lett.*, 19:1264, 1967. doi: 10.1103/PhysRevLett.19.1264.

[136] J. Wess and B. Zumino. Supergauge transformations in four dimensions. *Nucl. Phys. B*, 70:39, 1974. doi: 10.1016/0550-3213(74)90355-1.

Riccardo A. Manzoni: *Search for a Higgs boson decaying into a di-τ pair in the double hadronic final state,* © December 2014